Conical Spring and Localised Region Methodologies for Modelling of Soft Tissue Deformation

A thesis submitted in fulfilment of the requirements for the degree of Doctor of Philosophy

Mohd Nadzeri Omar

Bachelor of Engineering (Mechanical), RMIT University

School of Engineering

College of Science Engineering and Health

RMIT University

October 2017

Declaration

I certify that except where due acknowledgement has been made, the work is that of the author alone; the work has not been submitted previously, in whole or in part, to qualify for any other academic award; the content of the thesis is the result of work which has been carried out since the official commencement date of the approved research program; any editorial work, paid or unpaid, carried out by a third party is acknowledged; and, ethics procedures and guidelines have been followed.

Mohd Nadzeri Omar

2 October 2017

Abstract

Considerable research efforts have been dedicated to the development of virtual reality simulators that facilitate medical students in learning anatomy and surgery in the virtual environment and to allow surgeons to rehearse the surgical procedures. The level of realism depends upon the simulation accuracy and the computational efficiency of underlying deformable models. Ideally, the deformable models should be able to simulate accurately mechanical behaviours of soft tissues with real-time visual and force feedback.

Modelling soft tissue deformation is not an easy task. Due to the complexity of soft tissue properties, many methods have been proposed to model soft tissue properties. One of the most well-known methods is the Finite Element Method (FEM). In this method, the soft tissue is represented by multiple elements that are derived based on complex mathematical formulations. It has been proven that the method is able to simulate soft tissue properties accurately, but it requires high computational cost to produce real-time interaction. In this regard, the Mass Spring Method (MSM) has been proposed as an alternative. The traditional MSM model simulates soft tissue deformation by discretising the soft tissue into several mass points that are connected to each other by linear springs. The major advantage of MSM is it has an excellent computational performance. However, the MSM application is limited to linear deformation, which does not represent the actual behaviour of the soft tissue deformation.

In this thesis, an improved MSM model has been proposed to simulate the complex behaviour of soft tissue deformations. The improved MSM model is called conical spring model which considers the general behaviour of soft tissue deformation that is a combination of linear and nonlinear responses. Piecewise approach is used to discretise each response individually, and the conical spring methodology is used to model the deformation behaviours during all the responses. The piecewise approach gives precision in modelling while the conical spring methodology that was founded on stiffness variation, has improved the accuracy of the simulation due to its ability to model any type of linear and nonlinear responses. Moreover, the generated conical spring model is based on the force propagation approach. The computational performance of the model relies on the number of nodes involved in the propagation of the force. Inherently, computational time can be improved by considering the nodes only in a deformation area, and ignoring the other nodes.

Soft tissue deformation commonly occurs only within a local region. As the effect of the deformation outside the local region is very little, it can be ignored in real practice. In this thesis, methods to define the local region were proposed. The methods are based on the linear elastic theory. As reported in Chapter 4 of this thesis, the localised region was generated based on displacement value induced when the simulation model was subjected to an external load. The Boussinesq method, which is widely used in the soil mechanics, was used to estimate the induced displacement value. However, the Boussinesq method is limited to the isotropic material. Therefore, as described in Chapter 5, the study has extended the isotropic localised region to anisotropic localised region by introducing an anisotropic factor which was derived based on cross-anisotropic properties. By using the anisotropic factor, the anisotropic localised region is determined from the corresponding isotropic case.

Alternatively, in Chapter 6, we have presented a localised region that was generated based on stress value induced during a loading process. It is shown for point load type of contact, in comparison to ABAQUS analysis, stress based localisation has a better accuracy than the displacement based localisation. However, the stress value that is also determined using the Boussinesq method, has no relation to the material properties. Hence, a combination of the Hertzian and the Boussinesq method was used to generate localised regions with respect to the material properties and loading conditions.

In the final chapter, contributions of the study were discussed, and some of the future works to expand the research were listed out.

Acknowledgement

First and foremost, I would like to thank Associate Professor Yongmin Zhong for his invaluable guidance throughout this research work. His knowledge, direction, and support helped me to progress in this thesis. Without him, this thesis would never have materialised.

Thanks also to RMIT University and the University of Malaysia, Pahang, for giving me the opportunity to pursue my academic objectives and for supporting me and my research work through their scholarships.

Finally, I would like to thank my parents, who deserve my highest appreciation, as well as my sisters and brothers for their love and support. I would also like to thank my wife for her love, encouragement, and patience during the lengthy journey taken. For sure, my lovely kids, who have made me gone deeply through the course of this work.

Table of Contents

List of Tables

List of Figures

1 INTRODUCTION

As the incidences of traumatic injuries, cancer and cardiovascular disease continue to increase, the impact of surgical treatment on the public health systems continues to grow. As a result, there is a high volume of surgery worldwide; an estimated 234 million major operations are performed around the world each year, corresponding to one operation for every twenty-five people alive. Surgery is often the only therapy that can alleviate disabilities and reduce the risk of death from common conditions. While surgical procedures are intended to save lives, an unsafe surgical procedure can cause substantial harm. At a minimum, seven million surgical patients could be harmed by surgical failures each year, including at least one million patients who could die during or immediately after a surgical procedure. Given the high death and complication rates of major surgical procedures, surgical safety is now a substantial global public health concern [1, 2].

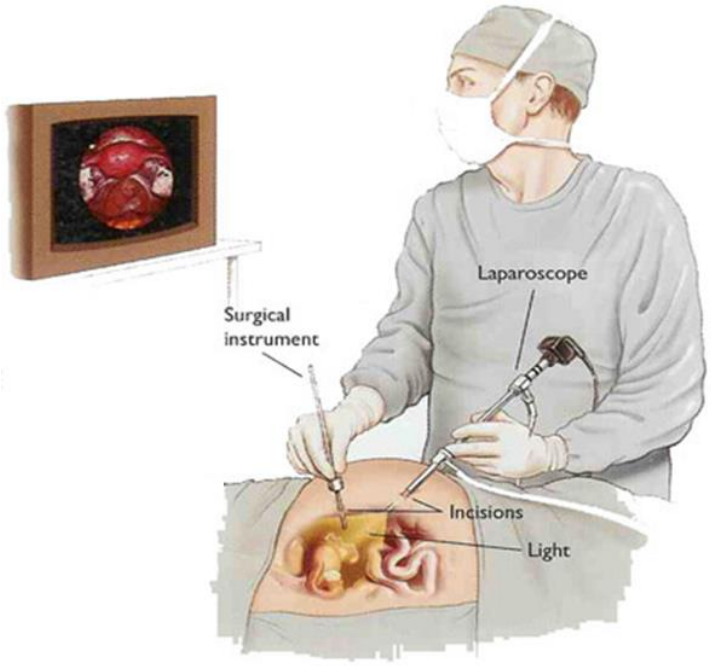

Figure 1.1. Minimally Invasive Surgery (MIS).

Minimally invasive surgery (MIS), which is a surgery performed with long thin instruments through small incisions, has been used for several decades (see Fig. 1.1). The main reasons behind the rapid developments in MIS include its benefits for the patient, such as less trauma, shorter hospital stay and reduced recovery time [3]. In some cases of minimally invasive procedure, surgeons would make several small incisions, just a few millimetres on the skin. A long, thin tube with a miniature camera attached to the end (called an endoscope) is passed through one of the incisions. The images from the endoscope will

be projected on the monitors in the operating room so that surgeons can get a clear and magnified view of the surgical area while special instruments are passed through the other openings. These instruments allow the surgeon to perform a surgery by exploring, removing or repairing anything inside the body. To ensure safer surgeries, the most recent MIS is equipped with robotic assistance in the form of a robotic arm (see Figure 1.2).

Successful MIS does not only require the surgeon to be familiar with technical aspects of the procedure and skilled in the manipulation of instruments based on the guidance from the video images, the process also needs a well thought-out surgical intervention plan. Consequently, poor expertise can endanger the patient's safety, for example, damages to the grasped tissue caused by the instruments, which in turn can lead to a higher number of errors and complications. Therefore, surgeons need to undergo comprehensive training to develop expertise in performing MIS.

Figure 1.2. Robot-Assisted Minimally Invasive Surgery [Photo © The da Vinci® Surgical System].

A surgeon's expertise depends on the number of surgeries that the surgeon has performed. Traditional training requires a surgeon to operate surgeries on a living human. The method of training requires surgeons to work under the supervision of a skilled surgeon, learning the procedure during an actual operation on a patient. While this method includes careful observation and instruction from the expert, yet, it limits the opportunities to perform different procedures and to rehearse the procedures before returning to clinical practice. Moreover, this kind of procedure will expose high risk to the patient, and often renders a feeling of the patient being experimented upon.

On the other hand, conventional MIS training is delivered through seminars with the guidance of an experienced individual. The seminars may take place in laboratories by using anesthetised animals or

cadavers, however, the use of cadavers and animals does not only involve ethical issues, but also leads to unreliable data since the properties of the specimens might be different from a living human [4].

These drawbacks can be manipulated by establishing a form of virtual training for MIS procedure. The use of virtual surgical simulation allows the trainee to practice all or certain components of a procedure without posing any risk to the patient. The simulation will allow the surgeon to rehearse an operation and develop the necessary techniques without limiting the number of repetitions necessary to master the procedure. The ability to perform repetitions will lead to the process of optimising the surgical intervention plan, and consequently, more accurate and safer operation can be conducted [5-7].

1.1 BACKGROUND

Surgical simulation is not a new invention as it has been used for several decades. A simulator like Minimally Invasive Surgical Trainer–Virtual Reality (MIST-VR) by Mentice Corporation has been used in the field since the 1990s [8, 9]. Despite its rapid development, surgical simulation is still considered as a challenging field, and it will take some time before surgical simulation becomes available on the common ground.

The cause of this delay is due to the complexity in modelling soft tissue responses. For high-end applications, such as surgical training, the modelling outcome must provide an accurate visual response, and it must also be able to provide haptic feedback (see Fig. 1.3). On top of that, the feedbacks need to be delivered in a real-time interaction. Therefore, surgical simulations are strongly rely on the soft tissue modelling, and until now, there is no an ideal modelling approach available since it involves a large trade-off between variables, especially accuracy and real-time interaction [4, 5, 10, 11].

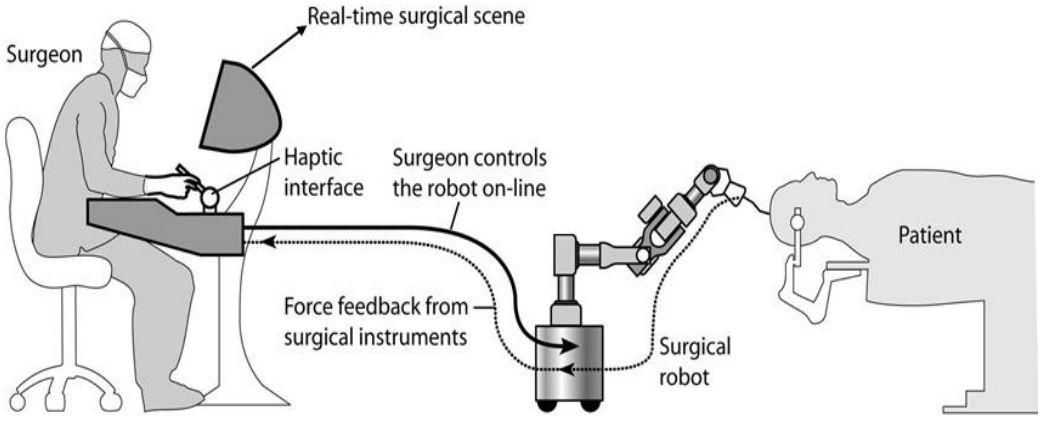

Figure 1.3. Components of surgical simulations [Photo © The da Vinci® Surgical System].

Soft tissues have a complex mechanical nature (see Fig. 1.4). Despite numerous experiments have been conducted, the specific mechanical properties of the soft tissues are still startling [12]. In general, soft tissues display nonlinear stress and strain relationships. It could extend its deformation beyond the elastic region and experiences plastic deformation where the strain could not be reversed to the original position. Moreover, soft tissues are comprised of the anisotropic and inhomogeneous structures. Besides, they are also classified as a viscous material where the stress is related to the rate of deformation. These kinds of properties require complex mathematical formulation to describe. Normally, in the soft tissue modelling, some will end up with a simplified assumption to reduce the calculation time, while other might sacrifice the time for an accurate presentation.

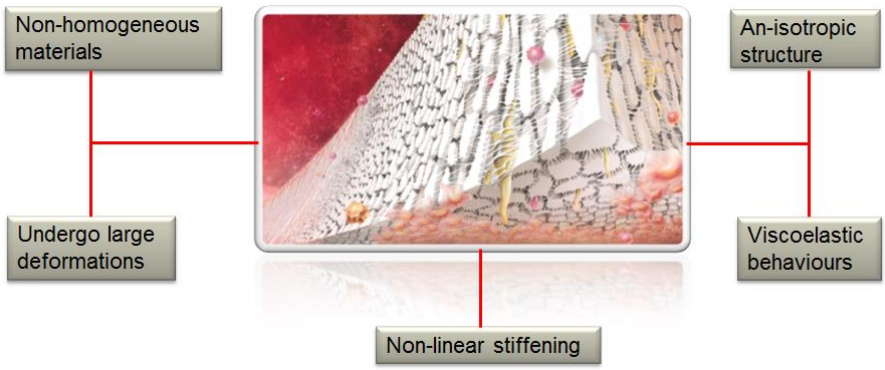

Figure 1.4. Soft tissue properties.

In general, the soft tissue modelling could be categorised into two groups; non-physics based and physics based (see Fig. 1.5). In a simple definition, the non-physics based is established on purely geometrical properties, where a model deformation is measured based on the mathematical representation of the model surface without taking any consideration of its mechanical behaviour [13,14]. The use of non-physics based significantly reduces computational effort, which provides real-time interaction. However, it does not provide realistic simulation, and relies on the expertise and patience of the user [14-15].

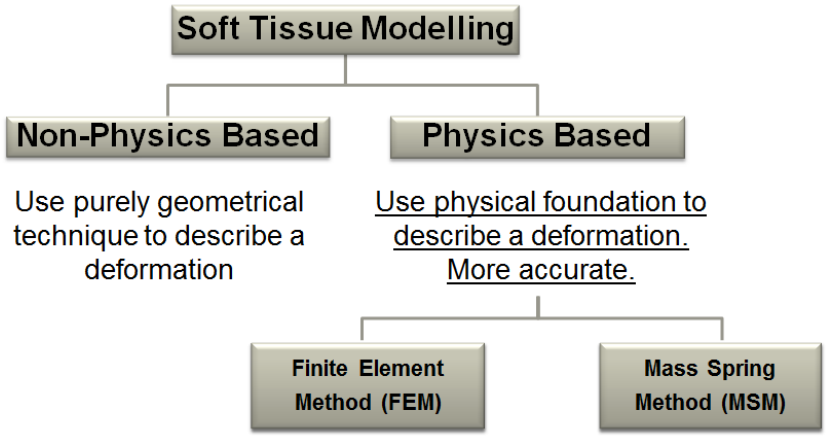

Figure 1.5. Soft tissue modelling.

On the other hand, the fast progress of technology brought upon the physics based method. The advances computing technology have made computer memories cheaper, and increasing graphics capabilities allow more complex modelling [14]. The physics based method develops a relationship between model parameters and the mechanical properties of soft tissues, thus providing more realistic performance. However, although it provides a more accurate representation of the soft tissues, it requires intense computational effort, which deters real-time interaction. Despite these limitations, there are many interesting applications for this method, especially in soft tissue modelling.

Two of the most popular physics based methods are Finite Element Method (FEM) and Mass-Spring Method (MSM). The first method is based on continuum mechanics that govern the elastic behaviour in the form of continuous medium consisting of connected volumes. The FEM based implementations are challenging. Although it portrays accurate and realistic performance, the FEM models are highly comprehensive, complicated and computationally intensive. In contrast, the second method views the elastic behaviour on a discrete basis. It discretises a model into discrete mass points connected to each other by springs. In general, traditional MSM models are governed by a much simpler mathematics than the FEM model. Hence, it offers simplicity and real-time interaction.

In this thesis, some approaches to improve the traditional MSM model were presented which could ensure highly accurate simulation of soft tissue deformations. At the same time, new methods focusing on computational time were also presented to enhance the performance of the proposed MSM model. The combination of the two methodologies enables simulation of nonlinear deformation at a real-time response.

1.2 OBJECTIVES

The general objective of this thesis is to improve the accuracy and computational time of the soft tissue modelling through the MSM model. The following points summarise the problems and the particular objectives of this research work:

- Traditional MSM is limited to linear deformation. It does not represent the deformation behaviour of soft tissues. In this study, the aim is **to develop a MSM model that can imitate nonlinear soft tissue behaviour.**
- In order to develop a simulation model as flexible as possible, the simulation models must have the ability to simulate different types of deformation. This study intents **to create a MSM model that can be initialised using build generic or pre-operative data.**
- Soft tissue modelling using the physics based approach consists of complex calculations. The calculations are directly related to the rate of response of the model. In some previous studies, simplifications were made to achieve the requirement hence disturb the accuracy of the model. In this study, the aim is to develop a method for **improving computational performance without affecting the accuracy of soft tissue deformation**.
- To simulate a real surgical procedure, the simulation needs to have a real-time response which is directly related to the computational performance of the simulation. Improvement in computational performance does not necessarily means that the real-time response is achieved. Another objective of this study is **to improve the computational performance within a real-time response.**

1.3 CONTRIBUTION OF THE DISSERTATION

This study had investigated some novel methods to improve the performance of soft tissue modelling. In particular, improvement in the accuracy and computational time of the MSM model were the main focused. The major contributions of this thesis are:

MSM model using conical spring methodology.

- The MSM model is developed without a fixed stiffness constant. The stiffness of the MSM model depends on displacement. The model will become stiffer at a large displacement which providing stiffness variety similar to the soft tissues. Hence, nonlinearity of the soft tissue can be imitated.

- The stiffness of the model is described from the geometrical properties of a conical spring. It creates flexibility in the model to simulate linear and nonlinear deformations. At the same time, different types of nonlinear deformation can be imitated too. With this flexibility, the proposed MSM model can be generated from any pre-operative data.

Localised region for soft tissue simulation.

- Localised region helps in improving the computational performance of a simulation model. The method reduced the computational burden by focusing only on a small significantly affected area instead of a whole region. It speeds up the calculation time leading to real-time interaction.
- A novel approach of the proposed localised region is it considers material properties. Different material properties lead to different deformations. By considering the material properties, the generated localised region will have a better accuracy.
- Another factor that influences the soft tissue deformations is the input load. The proposed localised region is described based on the input load. By considering the input load, the localised region that will be generated will have a higher accuracy, and can provide a dynamic localisation which optimised the computational performance of the model.
- Since the localised region method is not related to any topological features and it is simply based on the material properties and the input load, it can be applied to any modelling method to improve computations.

1.4 DISSERTATION ORGANISATION

The contents of this thesis are divided into seven chapters. The first chapter has presented the motivations for the thesis and the overview of the whole thesis. The second chapter outlines the background of the soft tissue modelling and focuses on the improvements of the MSM model.

Chapter 3: A new approach to model soft tissue deformation using conical spring model is proposed. The method is based on modifications of the spring stiffness so that the conical spring model will become stiffer at a larger displacement. The spring stiffness is modified with regards to the geometrical properties

of conical springs which leading to a greater flexibility in simulating different types of soft tissue deformation.

Chapter 4 & 5: In these chapters, methodologies to improve computational time are presented. The computational time is improved by using a localised region. The localised region is developed based on displacement distribution and uses load as the input value. In Chapters 4 and 5, the localised region is generated for isotropic and anisotropic materials respectively.

Chapter 6: Alternative approaches to generate localised regions are presented in this chapter that considers stress distribution as the foundation, and using displacement value as the input. Besides, different contact shapes are also demonstrated.

Finally, Chapter 7 concludes the thesis by summarising and discussing the research results and giving an outlook on possible new exciting directions for future research.

2 LITERATURE REVIEW

2.1 SOFT TISSUE PROPERTIES

Numerous experimental and theoretical studies in the field of soft tissue biomechanics have been carried out in recent years [15]. The purpose of these studies is to determine the mechanical characteristics of soft tissues. The following review summarises the literature related to this topic.

Deformation behaviour: The deformation behaviour of soft tissues is strongly influenced by the concentration and structural arrangement of its constituents [16]. Most of the time, the deformation behaviour of soft tissues is given in form of stress-strain diagrams. Stress is a measure of the average force per unit area of a surface of a deformable body when internal forces are applied on it. Meanwhile, strain is the geometrical measure of deformation representing the relative displacement between particles in the material body. In general, the stress-strain relationship of soft tissues is assumed to be nonlinear. However, looking at the details, the stress-strain relationship for soft tissues comprises of three regions, as illustrated in Fig. 2.1 [16]. In the first region, which occurs at a small deformation, the deformation behaviour is linear but as the strain progresses into the second region, the behaviour becomes nonlinear. In the second region, a larger load is required for soft tissue to deform. Thus, a sudden addition in the stress value can be observed. Finally, in the third region, the deformation has reverted to a linear behaviour.

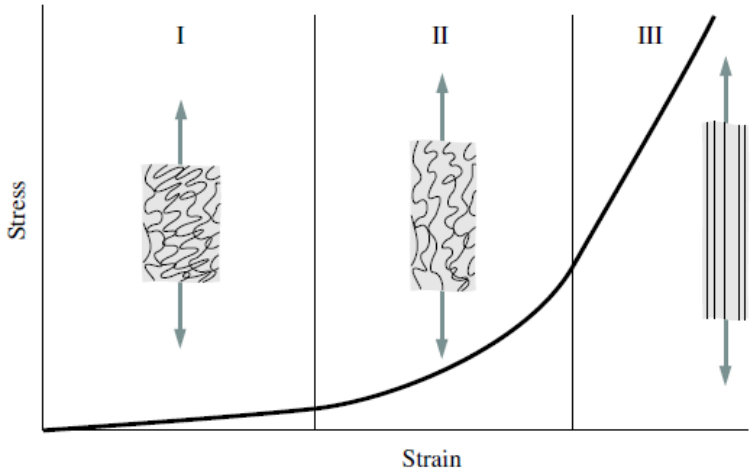

Figure 2.1. Stress-strain curve for soft tissue [16].

Viscoelastic: Moreover, soft tissues have been found to exhibit viscoelasticity [15, 16]. Viscoelastic materials refer to a material where the relationship between stress and strain depends on time, and they possess one of the following properties:

- Stress relaxation: A phenomenon that occurs when a tissue is stretched and held at a fixed length. Over time, the force presents within the tissue continually declines.
- Creep: A phenomenon that occurs in a tissue held at a fixed stress. Over time, the strain presents within the tissue continually increases.
- Hysteresis: A phenomenon that produces different deformation paths during the loading and unloading processes.

Complexity: The mechanical properties of soft tissues also depend on the topography, gender species (see Fig. 2.2), age (see Fig. 2.3), and chemical environmental factors such as temperature, osmotic pressure, and pH [17]. In the meantime, the extraction of soft tissue material properties is strongly related to the quality and completeness of experimental data, which comes from in vivo or ex vivo tests having the aim of mimicking real loading conditions. Therefore, presenting specific mechanical values for a specific tissue is still is a challenging task.

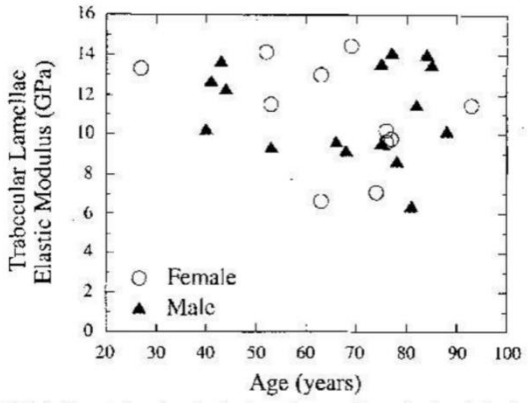

Figure 2.2. Graph showing the independence lamellar-level elastic modulus of trabecular tissue from age and gender [17].

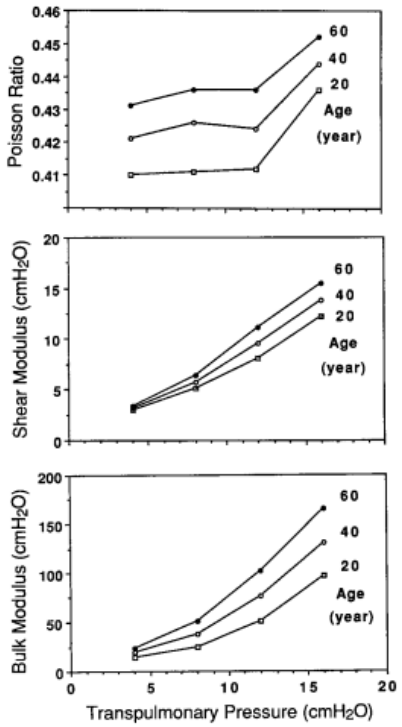

Figure 2.3. Values of Poisson ratio, shear modulus, and bulk modulus vs. trans-pulmonary pressure at 20, 40, and 60 years [17].

Anisotropic and Inhomogeneous: Soft tissues are multi-composite materials containing cells, intracellular matrix, fibrous, and other microscopic and macroscopic structures. The variation in materials shows that the mechanical properties of soft tissues vary from point to point within the tissue which explains inhomogeneity of the soft tissues. Essential aspects of modelling include the spatial distribution of material stiffness and the organisation of fibrous structures such as collagen and elastin fibres, which frequently have some preferred orientation. The dependency on directions makes the soft tissues anisotropic [15,16].

2.2 MODELLING METHODS

The deformable model can be classified into non-physics and physics based approaches. These approaches are different in the principles used to describe a deformable body. Methods categorised the non-physics approach are based on geometrical properties alone. One of these methods is the splines method. In this method, the curve or surface is represented by a set of control points. The designer adjusts the shape of the objects by moving control points to new positions through adding or deleting control points or by changing their weights. By moving the control points, the form of the respective curve, surface, or volume changes accordingly. The elevated number of parameters equips this deformable model with a substantial level of control over the shape and the physical properties of the mesh. However,

these parameters can only be chosen arbitrarily and are difficult to determine empirically. Another modelling method under the non-physics approach is the Free Form Deformation (FFD); FFD is a method which provides a higher and more powerful level of control than adjusting individual control points. The FFD changes the shape of an object by deforming the space where the object lies. This technique can be applied to many different graphical representations, including points, polygons, splines, parametric patches, and implicit surfaces [18-20]. Nevertheless, it requires expertise and patience to handle it carefully and modify it when the objects are being manipulated.

Meanwhile, the physics based approach is superior to the non-physics based approach in many aspects, especially in accuracy. Through the physics based approach, deformations that take place can be explained based on the physical properties. The level of inclusion of the physical properties varies from a simple linear elastic to a relatively complex hyper-elastic relation. In most of the cases, methods that are based on this approach can be further divided into two groups; first, methods that use discrete mechanics, and second, methods based on continuum mechanics.

2.2.1 Discrete mechanics

Mass Spring Method (MSM): The MSM is frequently used to simulate deformable objects because of their conceptual simplicity and computational speed. Since the early work by Terzopoulos et al. [21,22], MSM has been a standard tool to model deformable objects in surgical simulations. MSM requires discretisation of an object into mass points that are connected by elastic links (see Fig. 2.4). The discretisation can be defined on the surface or in the volume of the object. A common selection for the elastic link is linear spring which is based on the Hooke's law. The global deformation behaviour is determined by solving differential equations derived from Newton's second law of motion.

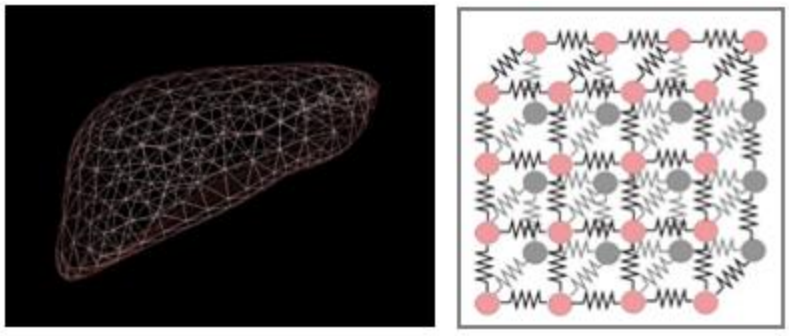

Figure 2.4. An example of a structure for MSM models.

Chainmail Method: The Chainmail algorithm represents a non-rigid body as a set of linked elements that resembles a chain, as shown in Fig. 2.5 [23]. The motion of a single mesh node is absorbed by the link

interface between adjacent nodes. If the link between two nodes is stretched or compressed beyond predefined limits, then displacements are transferred to neighbouring nodes. As a result, small displacements of a single node within a relaxed medium result in local deformations, while displacements within a fully stressed medium cause global motion. This approach is computationally efficient and can accommodate simple mesh topology changes. However, there is uncertainty in the accuracy of the simulation.

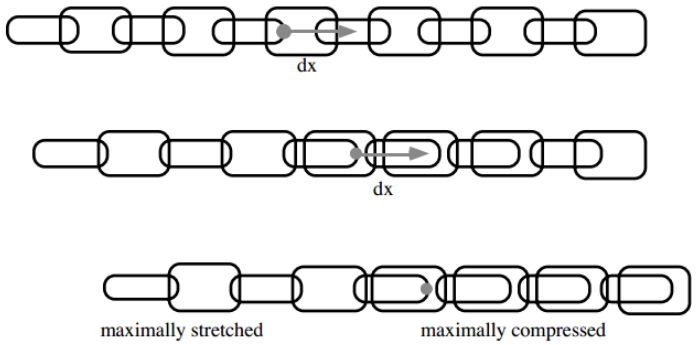

Figure 2.5. A one-dimensional chainmail structure undergoing deformation [23].

2.2.2 Continuum mechanics

Finite Element Method (FEM): In FEM, a body is divided into a number of finite elements that are connected to each other through continuum mechanics [24-26] (see Fig. 2.6). The displacements and positions in an element are interpolated from discrete nodal values. For every element, the partial differential equations governing the motion of material points of a continuum are formulated, resulting in a discrete system of differential equations. The main advantage of the FEM over the node-based discretisation techniques include a more flexible node placement and the substantial reduction of the total number of degrees of freedom needed to achieve the required accuracy of the solution.

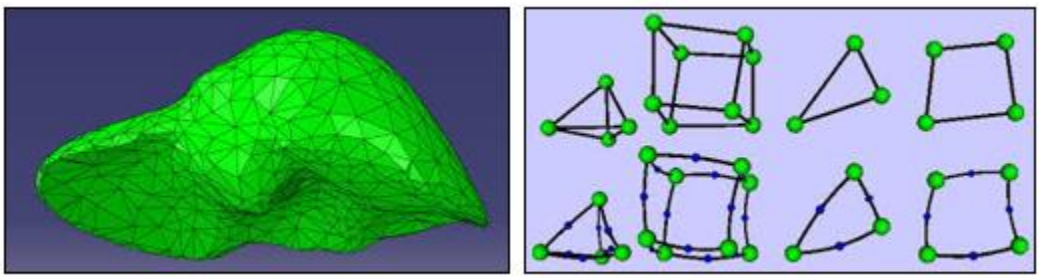

Figure 2.6. An example of a structure of a FEM model and types of element.

Boundary Element Method (BEM): Similar to FEM, this method is also based on continuum mechanics. However, the underlying partial differential equations were formulated as integral equations in boundary integral form [27], which has further simplified the FEM formulation leading to a better computational performance. In the meantime, the drawback of the method is it was established on the linear elasticity, thus, it does not accommodate large displacements. Moreover, it is also limited to the homogeneous and isotropic materials, which might not be the general case for soft tissues.

Meshless method: Further improvement on the FEM model has led to the development of the meshless method. The meshless method still uses the continuum mechanics principles, but instead of having finite elements, an object is approximated by a set of points without explicit connectivity. It eliminates the needs for updating the meshing steps. Consequently, it has a huge advantage in simulating a topological changed case such as cutting and insertion. Yet, it still consumes considerable computational resources, and requires localised solutions for optimisation [28].

Tensor Mass Model (TMM): TMM combines continuum mechanics with discrete mechanics in the sense that the internal forces are described based on energy based continuum formulations, and it is passed onto the vertices of the meshed elements which then provide movement by solving Newton's second law of motion [29,30]. The calculated internal forces are independent of the mesh topology which allows easy integration of interactive modifications such as cutting or tearing. The implementation improved the computational performance for the linear elastic case. But for the nonlinear elastic case, a high amount of computational resources is still required.

2.2.3 Comparison of MSM and FEM

Due to its mechanical realism, the physics based approach is the best option for surgical simulations that requires a high level of accuracy. Based on studies on the modelling methods, the physics based methods are fundamentally based on either the MSM or the FEM. Therefore, it is essential to have a further comparison between these two methods.

In the MSM model, the whole object is discretised into numbers of point mass which are connected to each other by spring connections. The mathematical principle of this method lies on the Hooke's Law equation which is easier to implement, and offers less computational time. Due to these properties and the suitability for parallel computation, it is the best method to present real-time application [31-34]. However, this method has low accuracy, and most of the time, it is developed for linear properties that is only valid for a small deformation. On the other hand, nonlinear capability is required for a large deformation, and to mimic a complete soft tissue deformation. Even though some literature had reported

the successful implementation of the nonlinear property in MSM [31,35-37], however, another challenge lies in finding the relationship of the model with the soft tissues. Moreover, several studies reported on generating the anisotropic properties in the MSM model [48, 66, 75]. It was done by manipulating the stiffness constant of each spring connection. For examples, Choi et al. [75] differentiated the stiffness value of the vertical and horizontal springs, while Hammer et al. [66] modified the stiffness constant for several springs by assigning a specific angle. In terms of viscoelasticity, most of the MSM models used the simple rheological models, such as Kelvin Voigt's model, to exhibit viscoelasticity [31, 58, 78].

In the meantime, Finite Element Method (FEM) is a well-known method for accuracy. It is able to describe the behaviour of soft tissues accurately. Unlike MSM, FEM allows material properties to be accurately implemented using in-depth mathematical formulations. It is based on continuum mechanics where a set of elements are used to present the whole model. This uniqueness allows the model to accurately simulate the mechanical properties of soft tissues [38-40]. On the other hand, despite its accuracy, FEM suffers from lower computational efficiency that brings down its real-time ability. Most of the FEM simulations that achieved real-time interaction had used linear properties, or incorporated nonlinear elements into a linear model [41-43]. Moreover, FEM simulations that can provide real-time interaction with nonlinear deformation require high computational cost and usually it will be equipped with parallel computations [26,40,44-46].

Two main modelling methods have been briefly compared and the wide presence of both formulations in simulation field shows that both are good candidates. Logically, each one of them has its advantages and disadvantages. In terms of accuracy, even though the FEM model has a superior accuracy, the MSM model still can provide a plausible outcome. The focal point is the computational time as the surgical simulation requires a real-time interaction. Comparing the two methods, the MSM model can provide better computational time with lower computational cost. Therefore, this study chose to focus on the MSM model for improvement.

2.3 IMPROVEMENT IN MSM MODEL

There are numerous studies available in the literature that focus on the improvement of the MSM model. In general, most of the studies focusing on improving the MSM model had discussed the nonlinear behaviour, the optimisation process, and the computational time of the MSM model.

2.3.1 Nonlinear behaviour

Existing research on the nonlinear MSM model has been reviewed. It was observed that several existing methods have some similarities. Therefore, to get a better understanding of the available methods, methods that have similarities have been grouped accordingly.

Quadratic stiffness and displacement function: Perhaps one of the earliest nonlinear MSM models was proposed by Cooper and Maddock [49]. They described the nonlinear behaviour of soft tissues as a quadratic function. A nonlinear spring was used where its displacement function was derived using the quadratic function. The main drawbacks of the method are, it was applicable only for two-dimensional objects, and there were no validation data presented. Later, Teschner et al. [50] described the nonlinear behaviour of their MSM model by modifying the stiffness of the spring. Instead of having a quadratic function on the displacement function like Copper and Maddock, Teschner et al. used the quadratic function on the spring stiffness. They have proposed three different stiffness functions for the user to select between linear, small nonlinear and large nonlinear. However, their approach is only valid for the stiffness values that converge to linear at small deformation. These limitations show that this method requires additional work to find the proper stiffness value. Also, the deformation behaviour of their method is limited to only those three functions. Similarly, Duysak et al. [51] also defined nonlinear deformation by using a nonlinear stiffness function, and included a nonlinear damping function. In contrast to Teschner et al., Duysak et al. generated the nonlinear function using neural networks. The study claimed that the method can achieve a satisfactory accuracy, but there were no indicators of the nonlinear behaviour presented, and the method also requires significant iterations before the values can be converged. The same approach can also be found in Mohammadi [52]. In addition, Pourhosseni et al. [53] reported the use of a nonlinear function that relates load and elongation. The study also introduced so-called nonlinear constraint to control the behaviour of the soft tissue model, however, no evidences of nonlinear deformation were presented.

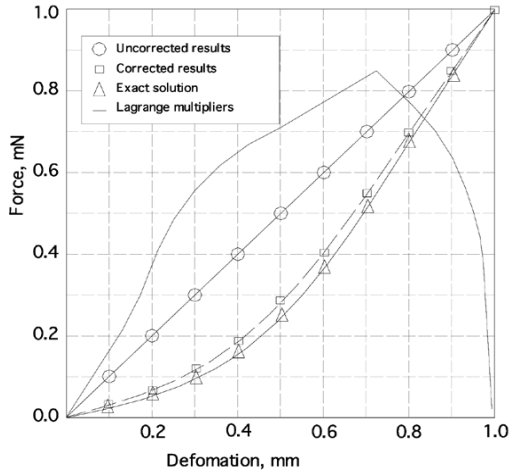

Figure 2.7. The nonlinear deformation behaviour is taken from Mohammadi [52].

Duffing's equation: In this method, a second order nonlinear differential equation called Duffing's equation is used. Duffing's equation is typically used to describe an oscillator system with third order polynomial. Luo and Xiao [54] had initially proposed this approach. Their study had managed to simulate nonlinearity, however, no validation process was presented. Cui et al. [35] also reported the use of a similar approach. The difference between these two studies is the method of defining global and local deformation. Moreover, in the study reported by Chen et al. [37], more details on the Duffing's equation was presented. The study shows different types of spring behaviour can be achieved by modifying parameters in the Duffing's equation. However, the outcome was not validated, hence, the accuracy of the method is uncertain. There are also several other studies that had used a similar approach, including Sulaiman et al. [55].

Spring configurations: The next approach was reported by Gaizka et al. [36]. In the study, the nonlinear response was achieved by a combination of linear springs in a cubical structure (see Fig. 2.8). Gaizka et al. used three combinations of spring configurations; edge spring, diagonal spring, and internal diagonal. All springs at each configuration have a specific stiffness constant, and used to control the nonlinearity of the model. Subsequently, Shah et al. [56] modified the initial work by using two instead of three configurations. Shah et al. only used the edge and diagonal spring configurations. On the top of that, a cubic spring constant was also introduced in the internal force equation for stability. Even though methods belong in this approach had managed to simulate nonlinearity, the optimisation process is still required. A few other studies also used a similar approach, for example, Garg et al. [57].

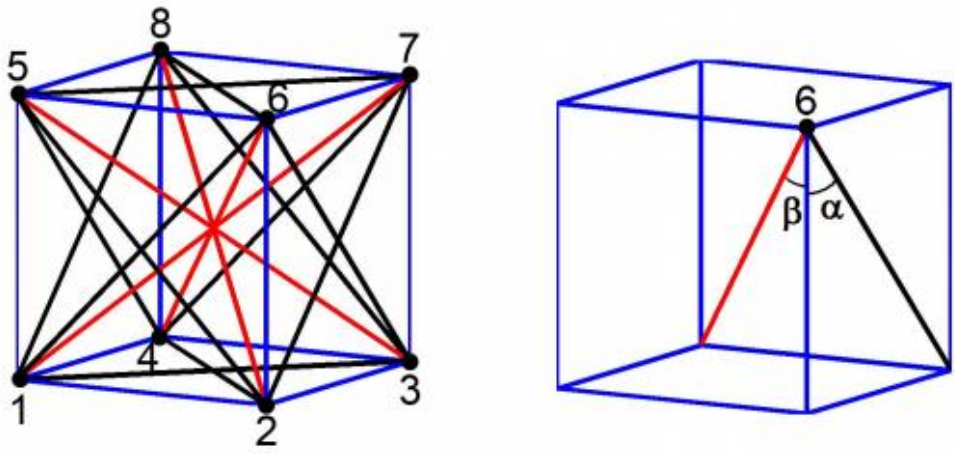

Figure 2.8. The nonlinear MSM using spring configuration given by Gaizka et al. [36].

Force propagation: Another MSM model that can produce a nonlinear response is the load propagation approach. The approach can be found in a series of studies by Choi et al. [58-59]. They developed a deformable model based on a successive force propagation process. In this method, the number of springs involved during deformation was increased with the depth of the deformation. As a result, the larger resistance force was recorded with the increasing of depth resulting in nonlinear response. Even though the methods are able to simulate nonlinearity, the nonlinearity of the models is not smooth, and it appears to be a combination of two linear functions (see Fig. 2.9). A similar approach was also used in Mun et al. [60] and Chang et al. [61].

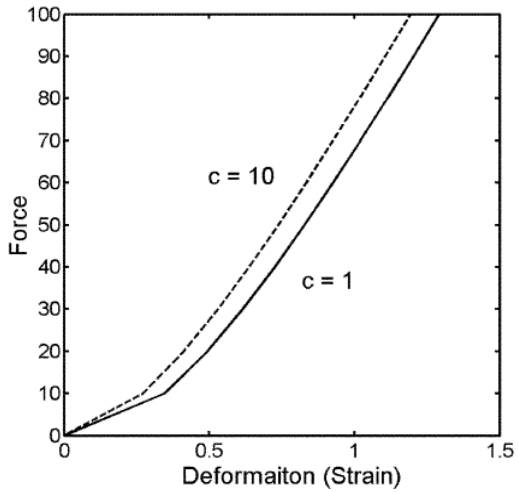

Figure 2.9. The nonlinear deformation behaviour, as taken from Choi et al. [58].

Piecewise function: Another approach to model nonlinearity is the use of the piecewise method. Here, the deformation behaviour is divided into sections, and each section has its formulation. Generally, there are two types of piecewise method, linear and nonlinear. In the nonlinear type, the nonlinear function is

used. For example, Basafa et al. [31,62] proposed the nonlinear piecewise approach where the deformation behaviour was split into two parts (see Fig. 2.10). The first part is linear and is governed by a linear function until a transitional point is met. Meanwhile, the second part takes place over the transition point and is defined by a nonlinear function. A similar approach was also reported by Nikolaev [63]. On the other hand, for the linear type, more than two linear functions are required to get a smooth nonlinear response. It can be observed by comparing the work of Keeve et al. [64] and Garcia et al. [65]. Keeve et al. used two linear functions while Garcia et al. used more than two linear functions to describe nonlinear behaviour. The result has shown that even though greater accuracy can be recorded with more linear functions, it will consume larger computational effort. Besides, defining the transition points is a tedious effort. Another example of the piecewise approach can be found in Hammer et al. [66].

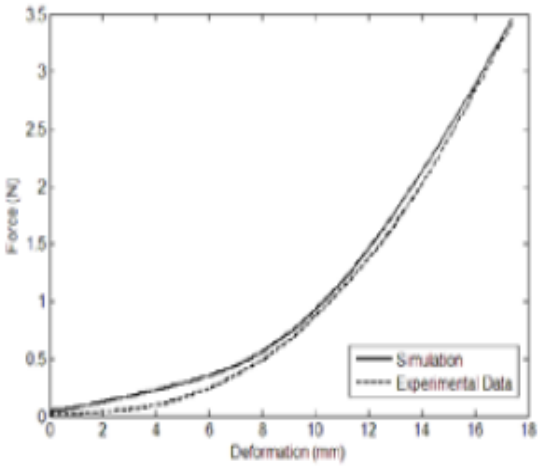

Figure 2.10.The nonlinear deformation behaviour, taken from Basafa et al. [31].

Hybrid approach: In this approach, researchers have taken advantage of the continuum mechanics and adopted it to the MSM model. Studies conducted by Cotin et al. [67] and Picinbono et al. [68] can be described as the pioneers of this approach, while Xiaoping et al. [30,69] also applied this method in their more recent study. In this method, the internal forces of the model were derived based on the nonlinear continuum mechanics while deformation was solved explicitly as the MSM model. Even though the implementation can provide the nonlinear response, the computational cost would increase due to the use of complex mathematical equations.

Other methods: Apart from the already mentioned methods, there are some other MSM methods that are able to simulate nonlinearity of soft tissues. Castillo et al. [70] proposed a method that relates nonlinear deformation with resistance to elongation. They modified the classic mass-spring model by increasing the elasticity of the spring with increments in elongation. The elasticity coefficient of the spring

was described as exponential evolution with the elongation. Another alternative is the work of Ahmadian et al. [71] who used empirical formulation to describe the internal resistance based on experimental data. They proposed two empirical equations for two types of soft tissue nonlinearity. The proposed method can simulate the deformation accurately, but it consumes considerable resources before finding the correct empirical formulation, and the process needs to be repeated for different subjects. Wang and Guo [72] also derived a nonlinear model using the experimental result. By using the least square method, they derived the equation and the stiffness value of the model. Meanwhile, Duan et al. [73] used inverse dynamic to define nonlinear response where the nonlinear Gaus-seidel method was used to update the position of the mass point.

2.3.2 Optimisation process

MSM requires an optimisation process since it was developed using a discrete approach and its parameters do not have any relation to material properties. The optimisation process could be divided into two groups. In the first group, the optimisation process is focused on the direct relation between the soft tissue properties and MSM parameters, while the second group is concerned with tuning the parameters for an objective function.

The first group of optimisation can further be classified into two approaches. The first approach uses a real soft tissue as reference [81-83, 88]. For example, Zerbato et al. [88] illustrated a method to calibrate MSM models with an arbitrary topology defined by a tetrahedral mesh taken from computer assisted tomography (CAT) images, and behaviours in the form of load-displacement values. In the second approach, the MSM parameters are optimised with reference to continuum mechanics. Most of the scholars had used FEM as their reference [37, 22, 56–60, 84-87], while one study used the finite difference method as a reference [61]. In the meantime, Gelder [84] used triangulated spring mesh on a MSM structure to incorporate the information from continuum mechanics. Gelder attempted to find a MSM equivalent to a triangular linear FEM model by linearising the system of equations of the MSM. Lloyd et al. [85] extended the work by providing a general method to obtain approximated stiffness values for any type of triangle, and rectangular meshes at Poisson's ratio equal to 1/3. Later on, Delingette [86] improved the works of Gelder and Lloyd et al. by using triangular mesh. The study was able to show the equivalence between a continuum formulation of the membrane energy and the energy of a set of triangular mesh with the introduction of biquadratic springs.

Another approach in the optimisation process is using an objective function to specifically tune the MSM parameters to meet the properties of the reference model. This approach belongs to the second group of

optimisations. In this light, a commonly used method is the simulated annealing method which is a probabilistic method for finding the global minimum of an optimisation problem. This method has been used to extract the system parameters for MSM models such as in the work of Choi et al. [59] where simulated annealing was employed to optimise the Force Propagation Method (FPM) for volumetric objects. Automatic parameter extraction was achieved by benchmarking against the deformable models developed by the elastic theory and finite element method. Xiaoping et al. [30] also used the same approach. The study simplified the process by setting a few parameters to an equal value. Several other studies also applied simulated annealing for the optimisation process [88, 89]. Furthermore, the genetic algorithm method presents another commonly used probabilistic method. The algorithm starts with a set of solutions called population, and the optimisation will be repeated until some conditions are satisfied. Louchet et al. [90] implement this method in their MSM model where the model was used for cloth simulation. The application of the genetic algorithm method also can be found in several other studies [91-93]. In the meantime, other notable probabilistic methods include evolutionary method [90, 94] and least square method [72].

2.3.3 Computational Time

The improvement of the traditional MSM, especially with the incorporation of nonlinear behaviour has affected the computational time. This section presents some of the methods that have been proposed to improve the MSM computational time.

Localisation: Localisation seems to be one of the most common methods to reduce the computational burden. Instead of calculating the whole model, localisation specifies and runs the calculation only in a targeted area. Several studies have implemented localisation to achieve real-time interaction. Qiao et al. [97] used the improved method of the nearest neighbour particle (NNP) to create localisation. Moreover, Zhu et al. [98] used the term influence region to develop localisation (see Fig. 2.17). The influence region was drawn using triangular mesh and depends on the location of the probe. Other studies that also reported the use of localisations include Chen et al. [37]. Meanwhile, in the Force Propagation Method (FPM) as reported by Choi et al. [58-59, 75], localisation was made by defining the localised region based on the optimum penetration depth. Despite the improvement in computational time, the main drawbacks of the current approach are they are not related to material properties, and the size of the localisation is fixed during simulations.

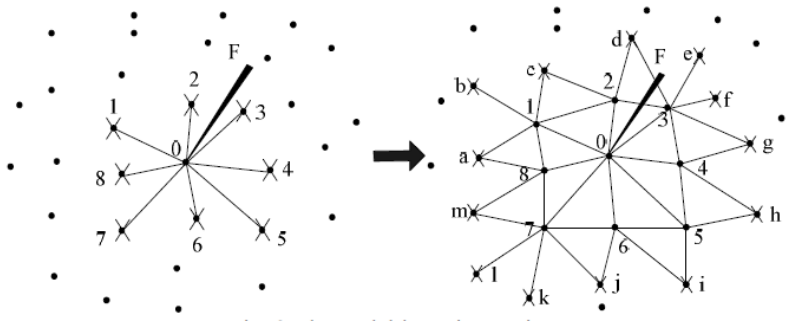

Figure 2.11.The localisation of the deformable object [37].

Parallel computation: Moreover, literature also suggests that computational time can be improved by using parallel computation which requires another computational component called General Processing Unit (GPU). In this light, MSM by its nature is parallelisable hance several studies had provided the evidence of the implementation [99-103]. Georgii and Westermann [99] used GPU to gather information on the location of the mass points and calculate the internal force of the MSM. This information was used later to update deformations. Leon et al. [102] also used GPU to calculate the internal force and to update the node position based on the previous location. In the more recent studies of Vassilev et al. [101], Rasmusson et al. [100] and Etheredge [103], parallel computation was run on the parallel computation framework called CUDA.

Numerical integration: Another common approach is to improve the numerical integration method used to solve the dynamic equation of the model [97]. Several studies have been reported on the numerical integration itself and the comparison between each of them. The process of selection does not just concern the computational time, but also the stability of the system. In general, an explicit method such as central difference method is preferable due to the low computational cost. However, some attention need to be paid on the stability of the model. On the other hand, the implicit method provides better stability, but it requires higher computational effort. Therefore, the process of choosing the best method is still crucial.

2.3.4 Conclusion

With regards to the literature on the improvement of the MSM model, several conclusions can be made. First, the current nonlinear MSM model does not consider the three phases deformation as reported by Holzapfel [16]. Second, only a small number of nonlinear MSM models provide validation either with experimental data or continuum mechanics. Moreover, there is still no method that can directly relate the MSM parameters with the material properties of soft tissue. Nevertheless, through optimisation, the accuracy of the simulation can be improved. Despite the current computational improvements,

computational time needs to be reduced in conjunction with maintaining accuracy and low computational cost.

2.4 CHAPTER SUMMARY

In this chapter, several studies related to surgical simulation were reviewed. The review began with observing the properties of soft tissues that is the most crucial part to model. Then, the current state of the art in soft tissue modelling was discussed which leads to the selection of MSM based model as the main focus for improvement in soft tissue modelling. Overview of the current improvements of the MSM model was also presented and several conclusions on the improvements have also been indicated.

3 SOFT TISSUE MODELLING USING CONICAL SPRING METHODOLOGY

It is well accepted that soft tissue deformation is a combination of linear and nonlinear responses [15, 16]. According to Holzapfel [16], soft tissues show linear deformation during a small displacement and it will exhibit nonlinear deformation at some distance beyond the small displacement value. Then, prior to rupture, soft tissues will display linear deformation again. Overall, soft tissues involve three deformation phases, as shown in Fig. 2.1. By considering nonlinearity for the whole deformation, the MSM model cannot exhibit the real behaviour of soft tissue deformation.

Moreover, the nonlinear part of soft tissue deformation is more complex than exponential or polynomial functions. Even though some of the soft tissue deformations can be simulated using the exponential or polynomial functions, they are limited to a particular type of soft tissue, leading to the lack of ability of the model to simulate different types of soft tissue deformation. Another distinct property of soft tissues is it becomes stiffer during large deformation. It means that soft tissues do not have a constant stiffness. The stiffness value is varied in regards to displacement.

In this chapter, a new modelling method known as conical spring model is studied. The conical spring model takes advantage of the stiffness variation occurring in conical spring to simulate any type of deformation behaviours. The conical spring formulation is based on discretised elementary parts. Each elementary part has its own stiffness value based on its location with respect to the normal axis of the spring. During deformation, the summation of all elementary deflections will provide the total displacement of the conical spring. Furthermore, the piecewise approach is used to simulate the three phases of soft tissue deformation. A unique property of the piecewise approach used in the conical spring model is that only the calibration of the conical spring parameters is needed to simulate all the phases.

3.1 CONICAL SPRING METHODOLOGY

Conical spring methodology adopts the fundamental determination of the cylindrical spring force. It involves discretizing each coil of the conical spring into several elementary parts. The deflection of the conical spring for a given load is determined by adding the individual deflections of each part considered as a cylindrical spring.

3.1.1 Fundamental of cylindrical spring stiffness

One of the earliest studies to describe the behaviour of spring with external force was done by Wahl [104] which defined the behaviour for the cylindrical round-wire spring. To calculate deflection of the cylindrical

spring, Wahl discretised the spring into several elementary parts, and each elementary part of the spring coil is subjected to a torque moment M, given by

$$M = Pr \tag{3.1}$$

where r is the mean radius of the spring coil, and P is the load.

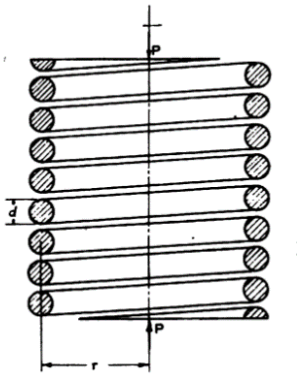

Figure 3.1. The structure of the cylindrical spring [104].

Fig. 3.2 presents a portion of the elementary part where the length dx is projected out between two planes perpendicular to the spring axis. Assuming that the plane does not bend out of shape or become twisted, it follows the shearing deformations.

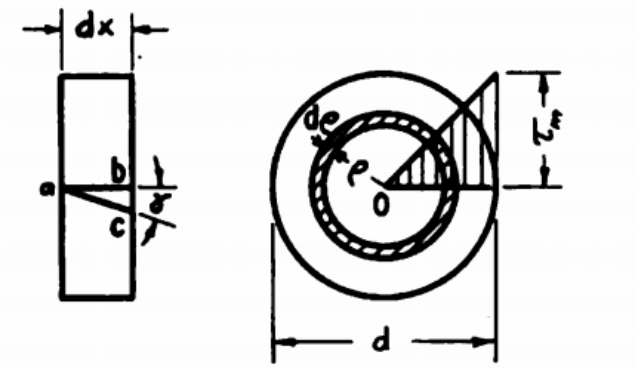

Figure 3.2. The cross-sectional element of spring wire under torsion [104].

For a distance ρ from the centre of the spring wire O, the shear stress can be calculated using the following equation

$$\tau = \frac{2\rho\tau_m}{d} \tag{3.2}$$

where τ_m is the maximum shear stress, and d is the diameter of the spring wire.

The moment produced by the shaded area of width $d\rho$ at a radius ρ is given by

$$dM = 2\pi\rho^2 d\rho \left(\frac{2\rho\tau_m}{d}\right) \tag{3.3}$$

The total torque moment of the load P at the spring wire is given as

$$Pr = \int_0^{d/2} dM = \int_0^{d/2} \frac{4\pi\tau_m\rho^3}{d} d\rho = \frac{\pi d^3\tau_m}{16} \tag{3.4}$$

By using Eq. (3.4), the maximum shearing stress can be calculated as

$$\tau_m = \frac{16Pr}{\pi d^3} \tag{3.5}$$

With the shear stress, referring to Fig. 3.2, the element will be distorted by a small angle of γ at deformation. Initial configuration of ab is transformed to ac. By considering elastic theory, the angle γ can be obtained using

$$\gamma = \frac{\tau_m}{G} = \frac{16Pr}{\pi d^3 G} \tag{3.6}$$

where G is the shear modulus.

Then, using Eq. (3.6) and assumed for a small angle, the length of bc can be defined in the form of

$$bc = \gamma\, dx \tag{3.7}$$

The elementary angle $d\alpha$ through which the cross section dx rotates with respect to the spring axis is given as

$$d\alpha = \frac{2\gamma}{d} dx \tag{3.8}$$

To calculate the total deflection angle of the spring, the spring is considered as the straight bar of length L

$$L = 2\pi n_a r \tag{3.9}$$

where n_a is the number of coils.

Hence, the total deflection β can be calculated using

$$\beta = \int_0^{2\pi n_a r} \frac{2\gamma}{d} dx = \int_0^{2\pi n_a r} \frac{32Pr}{\pi d^4 G} dx = \frac{64Pr^2 n_a}{Gd^4} \tag{3.10}$$

The effective moment arm of the load P is equal to r. Hence, the total axial deflection δ of the spring at load P can be obtained by

$$\delta = \beta r = \frac{64Pr^3 n_a}{Gd^4} \tag{3.11}$$

Based on the deflection equation Eq. (3.11), we have

$$\frac{P}{\delta} = \frac{Gd^4}{64r^3 n_a} = K \tag{3.12}$$

where K is the spring stiffness or the spring rate.

The above derivation shows that the spring force is calculated using discretisation of spring coils into several elementary parts. The total deflection of the spring is the accumulation of individual elementary deflection. Based on Eq. (3.12), when all the parameters are constant, the relation between deflection and the axial load is linear and the spring stiffness is constant. As discussed earlier, the stiffness of soft tissue is varied, hence, the above derivation is not suitable to simulate soft tissue deformation as a whole.

As observed in Eq. (3.12), different stiffness values can be generated if the radius of the spring is varied. To generate various value for the spring radius, conical shape methodology is used. The radius of conical shapes is varied from top to bottom and it can be controlled mathematically. By adding the conical shape methodology into Eq. (3.12), different stiffness values can be obtained.

3.1.2 Parameters of conical spring

As illustrated in Fig. 3.3, a conical spring is described using six design parameters. The design parameters involve diameters of the largest coil D_2 and the smallest coil D_1, number of coils n_a, diameter of the wire d, initial height of the spring L_o, and the shear modulus G.

3.1.3 Types of conical spring

The structure of conical spring can be described in many aspects such as using a constant helix angle or using a constant pitch value. However, conical springs derived using a constant helix angle is more complex. It will involve logarithmic and exponential functions. Hence, this study only focuses on derivation of conical spring using a constant pitch value. The pitch value indicates distance between coils in the conical spring. Throughout this study, the pitch value is not mentioned, but it is presented by the initial length and the total number of coils in the conical spring.

There are two types of conical spring that can be differentiated by the height in the fully compressed state. The height is called solid height L_s. The solid height can be determined from

$$L_s = \{max[0, (n_a d)^2 - (r_2 - r_1)^2]\}^{1/2} \tag{3.13}$$

For the first type of conical spring, Type I, the spring coils are stacked above one another. Hence, the height at the fully compressed state represents summation of heights of all coils. The first type of conical spring is called the nontelescopic conical spring. On the other hand, the solid height of the second type of conical spring, Type II, which is known as the telescopic conical spring, at the fully compressed state is equal to zero since all coils are compressed to the ground (see Fig. 3.3). Analytically, the type of conical spring can be distinguished using the following relations

$$(r_2 - r_1) < n_a d \qquad \text{Type I} \tag{3.14}$$

$$(r_2 - r_1) \geq n_a d \qquad \text{Type II} \tag{3.15}$$

where r_1 and r_2 are the radiuses of the smallest and the largest coil respectively.

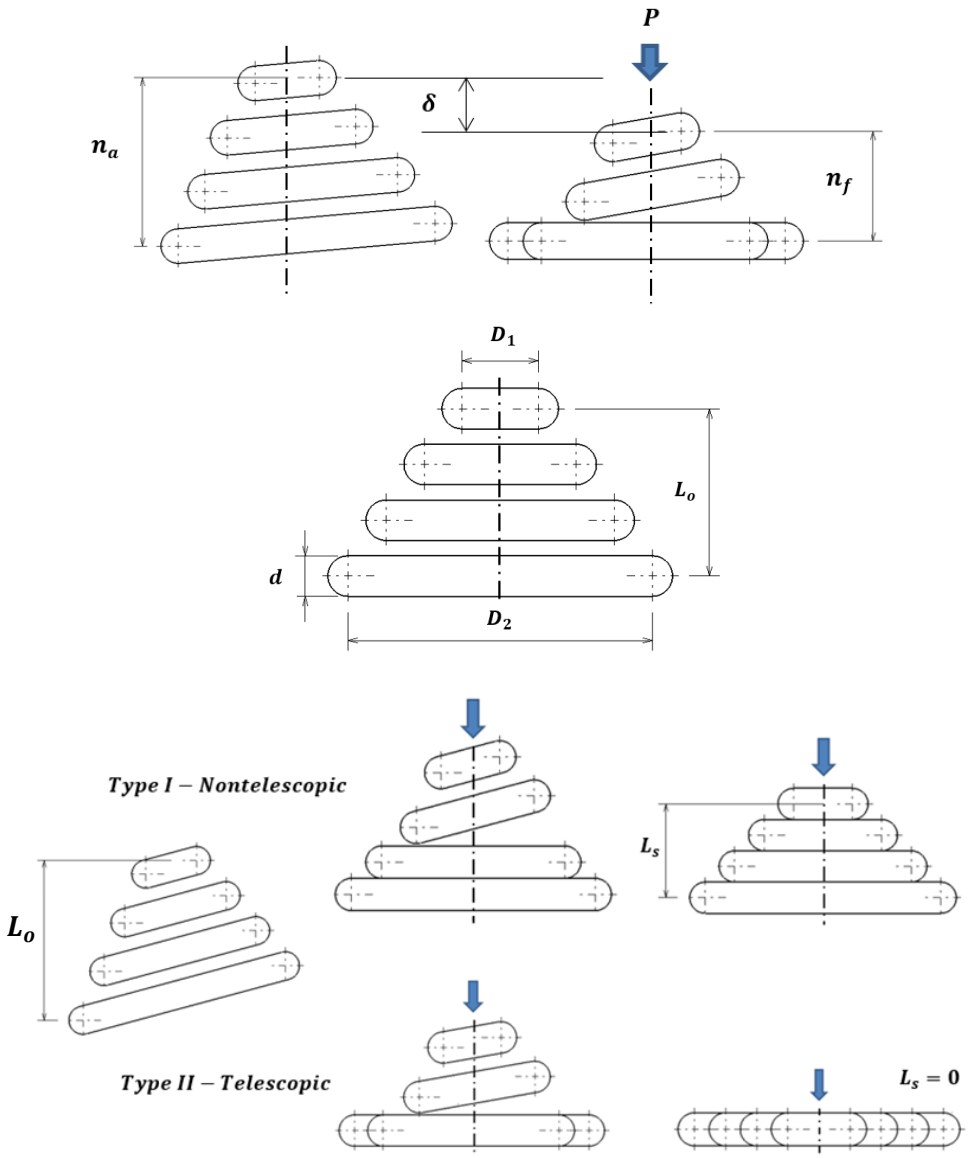

n_a	total number of coils
n	number of active coils (continuous variable from 0.0 to n_a)
d	diameter of the wire
D_2	diameter of the largest coil
D_1	diameter of the smallest coil
L_o	initial height of the spring
L_s	solid height of the spring (fully compressed)
δ	total axial deflection of the spring
G	shear modulus of the spring

Figure 3.3. Parameterisation of conical spring.

3.1.4 Formulation of conical spring

For conical spring with a constant pitch size, the radius of the active coil $r(n)$, can be determined using

$$r(n) = \left[r_1 + (r_2 - r_1)\frac{n}{n_a}\right] \tag{3.16}$$

where n represents the number of the active coil in the sequence of spring coils, which is a continuous variable from 0.0 to the total number of coils n_a.

For a given radius $r(n)$ that corresponds to the location of the current active coil, the elementary deflection $\delta_{f(n)}$ can be calculated as

$$\delta_{f(n)} = \frac{64P[r(n)]^3}{Gd^4}dn \tag{3.17}$$

On the other hand, as shown in Fig. 3.3, the maximum elementary deflection δ_s for any number of the active coil n can be calculated using

$$\delta_s = \frac{L_o - L_s}{n_a}dn \tag{3.18}$$

where L_o is the initial height of the spring.

The total spring deflection δ can be determined as the sum of elementary coils deflection δ_f (before fully compressed) and deflection made by the fully compressed coils calculated using δ_s,

$$\delta = \delta_f + \delta_s \tag{3.19}$$

$$\delta = \int_0^n \delta_f(n) + \int_n^{n_a} \delta_s \tag{3.20}$$

Solving the integration, the total spring deflection at any value of axial load can be determined by

$$\delta(P) = \frac{2P(D_1)^4 n_a}{Gd^4(D_2 - D_1)}\left[\left[1 + (\frac{D_2}{D_1} - 1)\frac{n}{n_a}\right]^4 - 1\right] + (L_o - L_s)(1 - \frac{n}{n_a}) \tag{3.21}$$

By eliminating the term n using Eq. (3.16), the inverse equation for Eq. (3.21) of load P in terms of deflection δ is given as [105]

$$P(\delta) = \left(\frac{A_1}{2}\right)^{\frac{3}{2}}\left[1-\left(1-2\left[1-\left(1+\frac{A_2}{{A_1}^2}\right)^{\frac{1}{2}}\right]\right)^{\frac{1}{2}}\right]^3 \tag{3.22}$$

where A_1 to A_7 are given as

$$A_1 = A_3 - \frac{A_2}{3A_3} \tag{3.23}$$

$$A_2 = -\frac{A_6}{A_5} \tag{3.24}$$

$$A_3 = \left[\frac{A_4}{16} + \left[\left(\frac{A_4}{16}\right)^2 + \left(\frac{A_2}{3}\right)^3\right]^{\frac{1}{2}}\right]^{\frac{1}{3}} \tag{3.25}$$

$$A_4 = \left[\frac{(A_7+\delta)}{A_5}\right]^2 \tag{3.26}$$

$$A_5 = -\frac{2D_1^4 n_a}{Gd^4(D_2-D_1)} \tag{3.27}$$

$$A_6 = -\frac{3}{8(D_2-D_1)}\left[\frac{Gd^4\,(L_o-L_s)}{n_a}\right]^{\frac{1}{3}} \tag{3.28}$$

$$A_7 = (L_o-L_s)\frac{D_2}{(D_2-D_1)} \tag{3.29}$$

The terms A_2, A_5, A_6, and A_7 can be precomputed from the conical spring parameters. The total deflection δ is equal to the displacement of the spring.

3.1.5 Stiffness variation in conical spring

The radius variation of spring coils for conical spring can be observed using projection view. For example, the projection view of conical spring with two coils is presented in Fig. 3.4. It shows the variation of the radius. By looking at Eq. (3.12), it is apparent that the spring stiffness is affected by the radius of the spring coils where the spring stiffness becomes smaller when the radius is larger. Furthermore, when conical spring is subjected to a load, the largest coil that has the smallest stiffness will be the first to deflect, where at this state conical spring will exhibit linear response because the degree of the stiffness variation is very small. Subsequently, deflection will continuously take place until all the coils are fully compressed.

Since the radius of the active element is getting smaller, the conical spring will become stiffer at large deformation which resulting in nonlinear deformation.

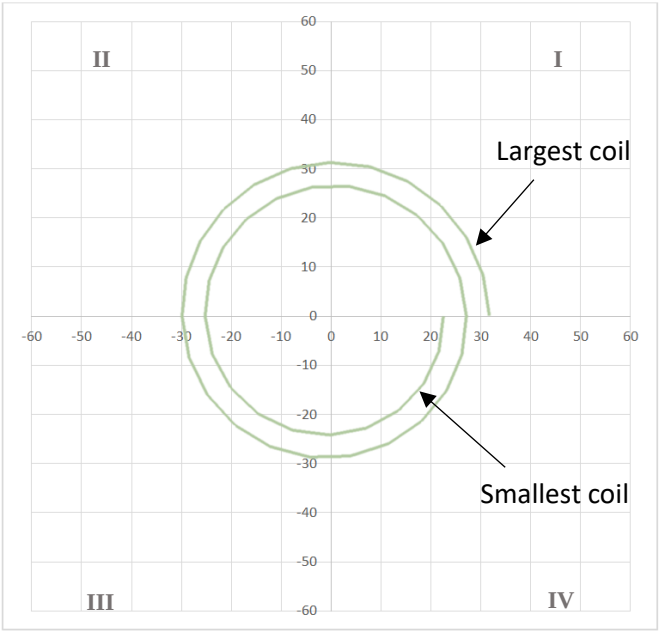

Figure 3.4. Projection view of the conical spring structure.

Moreover, by plotting the projection view of conical spring at different diameter ratios (D_1/D_2), different degrees of radius variation can be observed. As shown in Fig. 3.5, the degree of the radius variation increased for a smaller ratio. As a result, the stiffness variation in the conical spring will be larger leading to a greater nonlinearity.

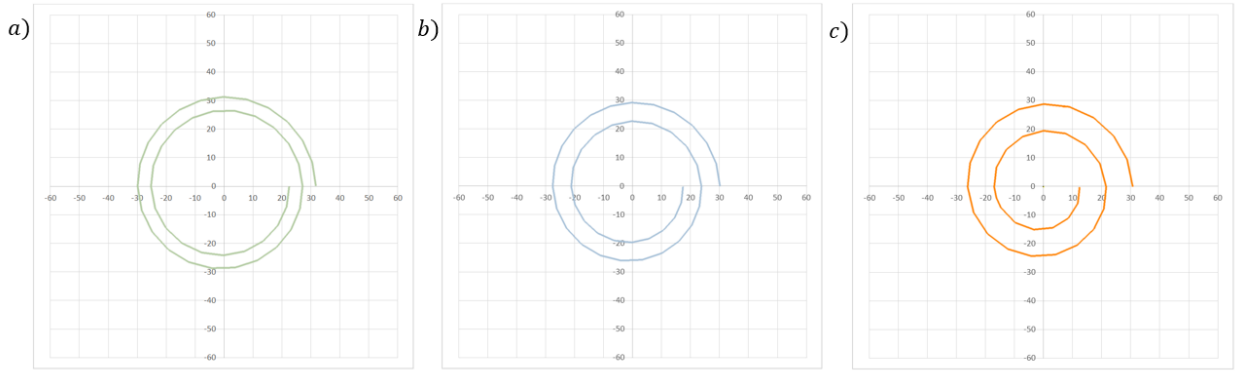

Figure 3.5. The projection view of conical spring at different ratio of the smallest and the largest coil (D_1/D_2). a) Large ratio, b) Medium ratio, and c) Small ratio.

3.1.6 Conical spring deflection behaviours

This subsection demonstrates the ability of conical spring to produce different types of deformation. During this analysis, the total number of coils n_a and wire diameter d were set to a constant value of 3.0 and 1.0 mm, respectively. The displacement range is set as 90 mm which is the maximum elementary deflection δ_s and the number of coils involved is controlled using n. Utilising Eq. (3.18), the new initial height of the spring L_o can be calculated using Eq. (3.30).

$$L_o = \frac{\delta_s \, n_a}{n} + L_s \tag{3.30}$$

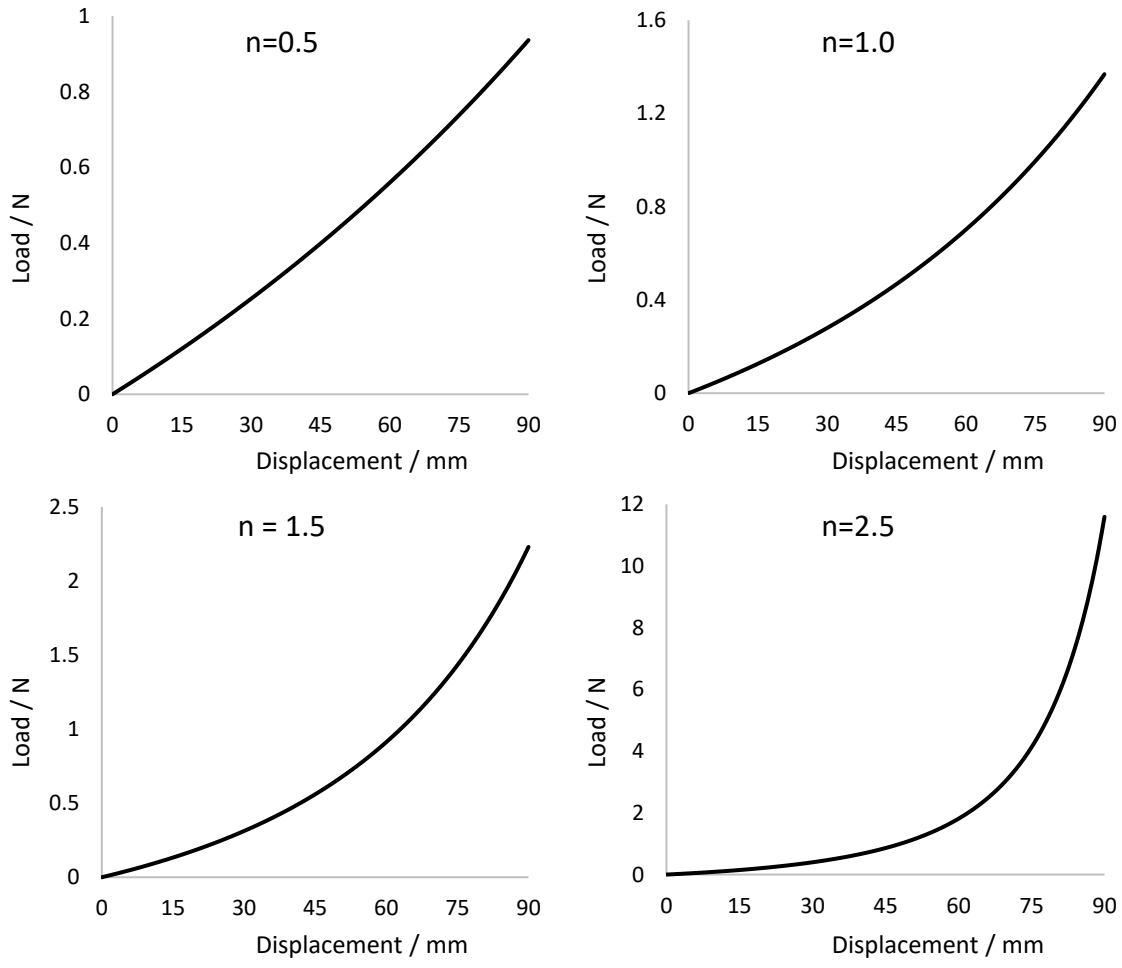

Figure 3.6. Deformation behaviour of conical spring at different number of coils involved within a given displacement value.

The amount of coil involved within a displacement range can provide different deformation responses. As shown in Fig. 3.6, conical spring shows a greater nonlinearity when more coils were involved within that displacement range. It is because of the stiffness variation that occurs is higher. Besides, when more coils

are involved, it can be seen that the conical spring becomes stiffer. This is due to the involvement of coils located in a smaller radius.

Moreover, the stiffness variation can be further controlled using the ratio of the smallest and the largest coil diameter (D_1/D_2). As given in Eq. (3.16), a smaller ratio will create a larger variation in the radius of the conical spring which consequently leads to a higher stiffness variation. As shown in Fig. 3.7, the deformation behaviour of conical spring was plotted using different ratios and it can be seen that a greater nonlinearity was recorded for a smaller ratio.

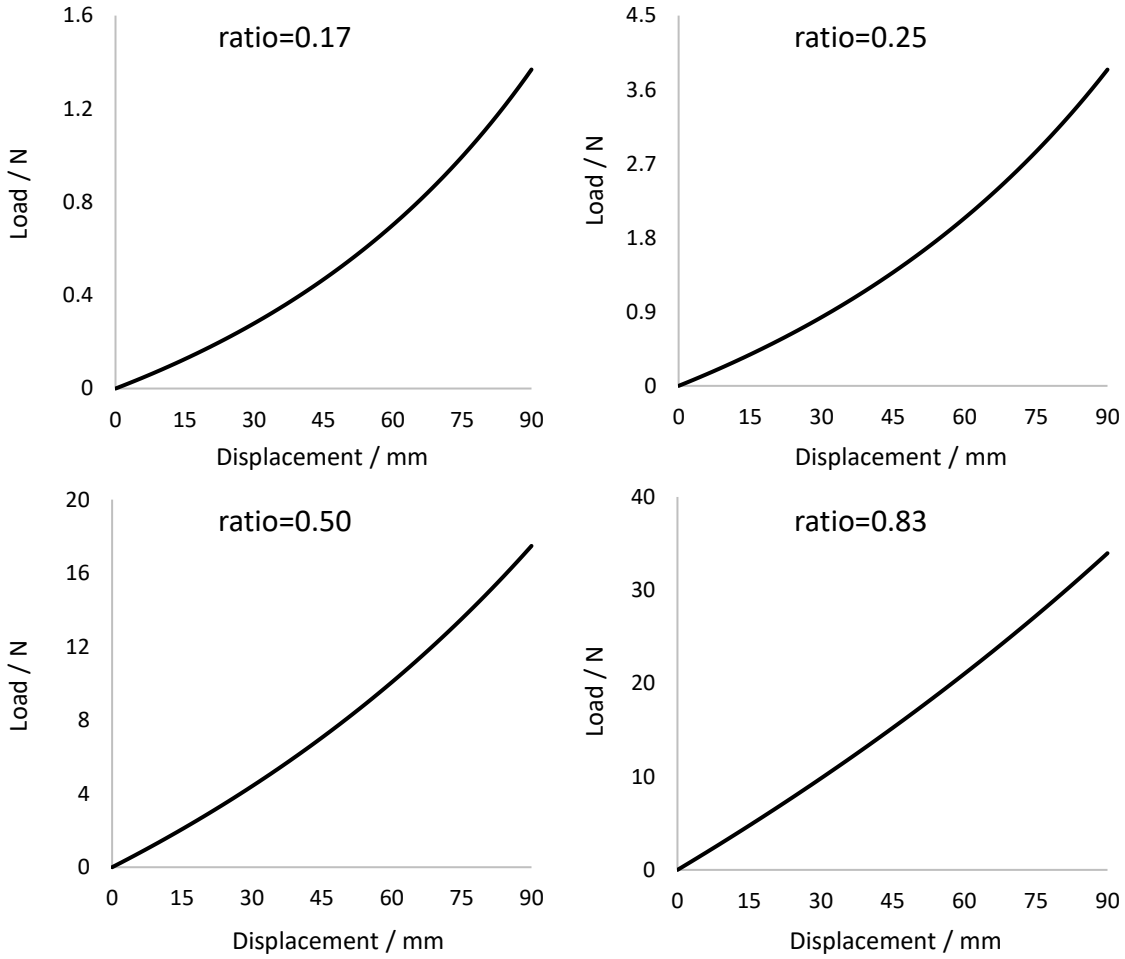

Figure 3.7. Deformation behaviour of conical spring at different values of diameter ratio (D_1/D_2).

In a special case where a linear response is intended, Fig. 3.6 and Fig. 3.7 suggest that the linear response can be obtained by reducing the stiffness variation through implementation of a smaller number of coils involved within a displacement range and a larger diameter ratio.

On the other hand, based on Eq. (3.17), for a given load P, the spring displacement δ can be controlled by the shear modulus G and the wire diameter d. It presents the strength of the spring. Since the size of the wire diameter d is fixed, therefore, the strength of the spring can be controlled using the shear modulus value G. As illustrated in Fig. 3.8, the conical spring becomes stiffer with a larger G, but the deformation behaviour remained unchanged.

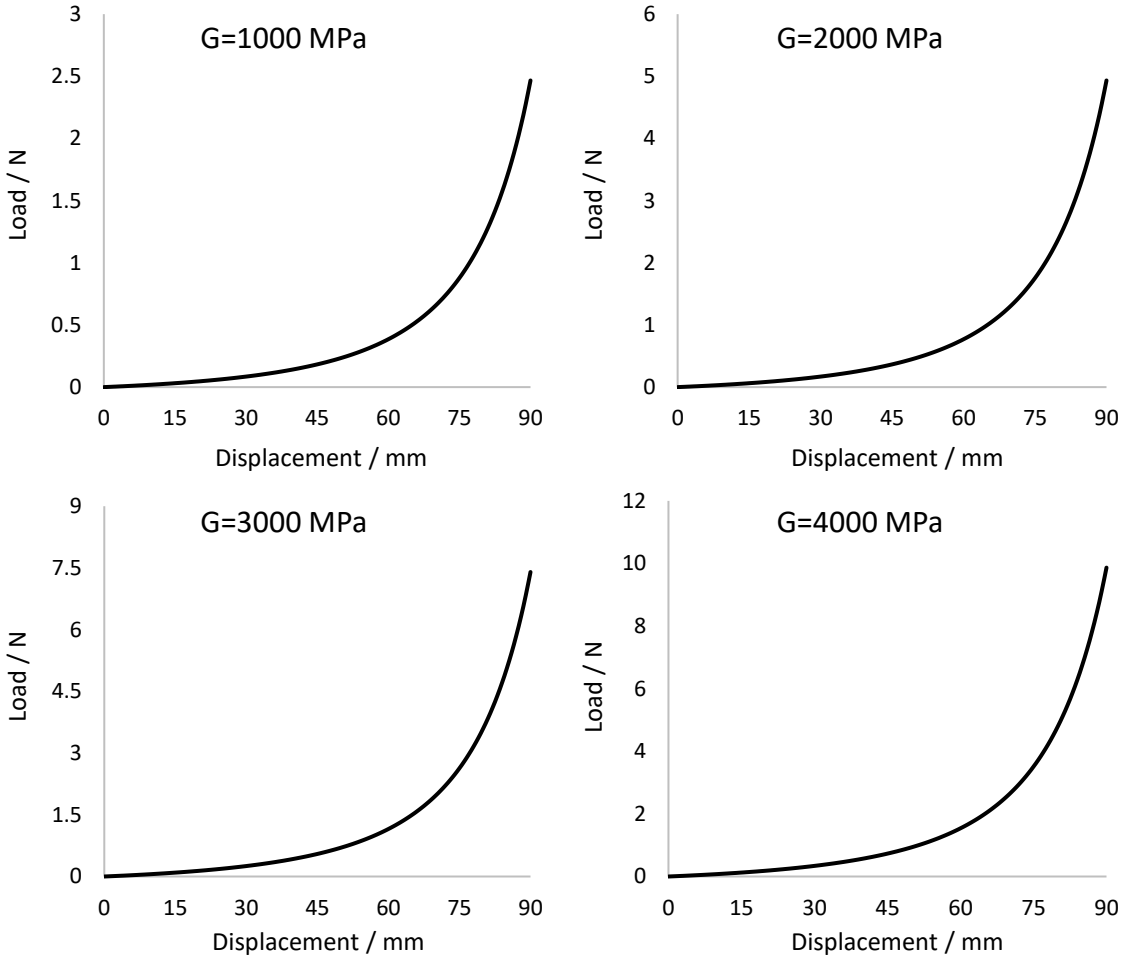

Figure 3.8. Deformation behaviour of conical spring at different values of shear modulus G.

The outcomes indicate that conical spring can produce different types of deformation. This can be achieved by controlling the stiffness variation through modifications of the conical spring parameters. This unique property provides flexibility for conical spring to model any type of deformation behaviours.

3.1.7 Model development

A cubical object is discretised into η mass points $\boldsymbol{u}_i$ with mass m_i, $i = 1, \ldots, \eta$. The mass points are connected to each other via conical spring in the shape of hexahedral element (see Fig. 3.9). Each mass

point is connected to six nearby mass points (see Fig. 3.10). When a mass point moves caused by an external force, the enforced displacement is propagated to the neighbouring mass points via the springs. This leads to the deformation of the model. The model state at time t is determined by the position $\boldsymbol{u}_i$ and velocity $\dot{\boldsymbol{u}}_i$ of every mass point.

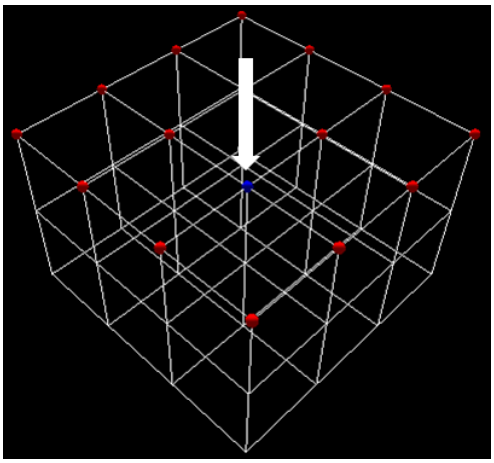

Figure 3.9. Conical spring model structure.

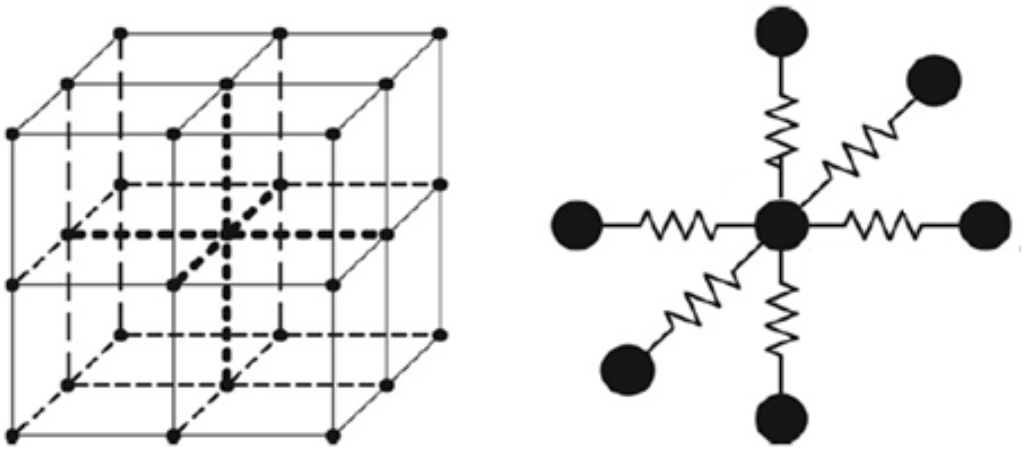

Figure 3.10. Connection illustration for the hexahedral element.

The typical dynamic motion of the MSM model is described by using Newton's second law of motion. In this regards, the total force experienced by a model consists of internal forces and external forces. The internal forces are constituted by a damping force and spring force. The damping force is responsible for generating the resistance due to the mass velocity, while the spring force defines the resistance experienced by the spring. The dynamic behaviour of each influenced mass point can be expressed as

$$m_i \boldsymbol{a}_i + \boldsymbol{F}_{di} + \boldsymbol{F}_{ki} = \boldsymbol{F}_{ext\_i} \tag{3.31}$$

where m_i is the mass at point i, $\boldsymbol{a}_i$ the acceleration at point i, $\boldsymbol{F}_{di}$ the damping force at point i, $\boldsymbol{F}_{ki}$ the spring force at point i, and $\boldsymbol{F}_{ext\_i}$ the external force applied on point i. The resultant force $\boldsymbol{F}_i$ acting at point i is given by

$$\boldsymbol{F}_i = \boldsymbol{F}_{ext\_i} + \boldsymbol{F}_{di} + \boldsymbol{F}_{ki} \tag{3.32}$$

With regards to displacement, Eq. (3.31) can be rewritten as

$$m_i \ddot{\boldsymbol{u}}_i + d_{ij} \dot{\boldsymbol{u}}_i + \boldsymbol{F}_{ki}(\boldsymbol{u}_i) = \boldsymbol{F}_{ext\_i} \tag{3.33}$$

where d_{ij} is the damping constant between points i and j. The terms $\boldsymbol{u}_i$, $\dot{\boldsymbol{u}}_i$ and $\ddot{\boldsymbol{u}}_i$ stand for the displacement, velocity and acceleration of point i respectively. The spring force at point i, is represented by the conical spring force $\boldsymbol{F}(\boldsymbol{u}_i)$, as described in Eq. (3.22).

The dynamic equation Eq. (3.33) needs to be solved using a numerical integration method. In general, there are two types of numerical integration, namely the implicit and the explicit approaches. The implicit approach is preferable because of its stability. However, it requires high computational cost to solve a large number of linear equations. On the other hand, the explicit method is simple and fast. It can treat nonlinearities as a straightforward process without any iteration. Nonetheless, the selection of time step is crucial since the explicit method can become unstable at small time steps. An improved explicit Euler integration is used in this study to optimise the advantages of both approaches as proposed by Huangfu et al. [117]. The improved explicit Euler integration is given as

$$\dot{\boldsymbol{u}}_i^{\,t+1} = \dot{\boldsymbol{u}}_i^{\,t} + \Delta t \cdot \frac{\boldsymbol{F}_i^{\,t}}{m_i} \tag{3.34}$$

$$\boldsymbol{u}_i^{\,t+1} = \boldsymbol{u}_i^{\,t} + \Delta t \cdot \dot{\boldsymbol{u}}_i^{\,t+1} \tag{3.35}$$

where t is the current time, $t+1$ is the next time step and Δt is the time step.

As shown in Eq. (3.34) and Eq. (3.35), the velocity of point i in the next time step $\dot{\boldsymbol{u}}_i^{\,t+1}$ is determined iteratively by using the explicit Euler integration, while the location of point i in the next time step $\boldsymbol{u}_i^{\,t+1}$

is computed with the implicit Euler integration. The improved method has a better stability than the traditional explicit Euler method due to the future quantity of $\dot{\boldsymbol{u}}_i^{\,t+1}$ is used to compute $\boldsymbol{u}_i^{\,t+1}$.

The detailed process of dynamic conical spring model is described in Fig. 3.11.

Step 1 Establish database on mesh and boundary conditions of conical spring model.

Step 2 Initialise the parameters of the model: $\boldsymbol{u}_i$, m_i, $\dot{\boldsymbol{u}}_i = 0$, $\boldsymbol{F}_i = 0$, d_{ij}, conical spring parameters, and save them in the adjacency list.

Step 3 Choose a threshold value to limit the force propagation. The next neighbouring mass points are determined using the Breadth First method.

Step 4 Initialise $t = 0$, and value for the time step Δt.

Step 5 Let an external force $\boldsymbol{F}_{ext}$ act on a mass point q of the model, and obtain the net resultant force $\boldsymbol{F}_q$ of q at time t.

Step 6 Solve the numerical integration using the improved explicit Euler method as follows.

i. $t = t + \Delta t$

ii. $\dot{\boldsymbol{u}}_q^{\,t+1} = \dot{\boldsymbol{u}}_q^{\,t} + \Delta t \cdot \frac{\boldsymbol{F}_q^{\,t}}{m_q}$,

$\boldsymbol{u}_q^{\,t+1} = \boldsymbol{u}_q^{\,t} + \Delta t \cdot \dot{\boldsymbol{u}}_q^{\,t+1}$

iii. Calculate the force of each mass point in the first neighbourhood of mass point q, and propagate the calculation to the next neighbourhood of adjacent mass points until the threshold.

Let $\boldsymbol{F}_i$ denote the force of point i in the n_{th} neighbours.

iv. $\dot{\boldsymbol{u}}_i^{\,t+1} = \dot{\boldsymbol{u}}_i^{\,t} + \Delta t \cdot \frac{\boldsymbol{F}_i^{\,t}}{m_i}$,

$\boldsymbol{u}_i^{\,t+1} = \boldsymbol{u}_i^{\,t} + \Delta t \cdot \dot{\boldsymbol{u}}_i^{\,t+1}$

v. Record and render the current state of the model.

vi. Repeat step i)-v) until the simulation is stopped.

Figure 3.11. Dynamic process of conical spring model.

3.1.8 Piecewise approach

As shown in Fig. 2.1, soft tissue deformation comprises of three different phases combined with linear and nonlinear responses. Instead of doing the overall simulation, better accuracy can be achieved by modelling the response according to the individual phase. The best method for the individual modelling is through the piecewise method that each phase will have a different formulation. Uniquely, for conical

spring model, the same conical spring function will be used for all the phases. Only the conical spring parameters will be modified to optimise simulation of each phase.

The piecewise function is given as

$$\boldsymbol{F}(\boldsymbol{u}) = \begin{cases} F(Set\ 1) & u_0 < u \leq u_1 \\ F(Set\ 2) & u_1 \leq u \leq u_2 \\ F(Set\ 3) & u_2 \leq u \leq u_3 \end{cases}$$

where $\boldsymbol{F}(\boldsymbol{u})$ is the conical spring equation used in Eq. (3.33), $F(Set\ i)$ is the conical spring function with parameters of $Set\ i$. The term $Set\ i$ is a set of conical spring parameters for that specific phase. Displacement value at each intersection is noted as u_i where for the three phases, $i = 1,2,3$.

A simple analysis was conducted to implement the approach. In this analysis, a load-displacement curve was divided into three phases according to the deformation response. The set of parameters used for each phase are given in Table 3.1 and to ensure a smooth transition between the phases, linearization was made at the transition points. The outcome of the simulation is shown in Fig. 3.12.

Table 3.1. Different sets of conical spring parameters used to generate the three phases of soft tissue deformation as presented in Fig. 3.12.

Parameter	Set 1	Set 2	Set 3
D1	5	2	3
D2	6	10	4
Lo	270	80	160
G	50	100	400
d	1	1	1
n_a	3	3	3
Type	Nontelescopic	Telescopic	Nontelescopic

The outcome shows that the three phases of soft tissue deformation can be simulated by the conical spring model. Moreover, the linear and nonlinear deformation responses for each phase can be simulated successfully through modifying the conical spring parameters.

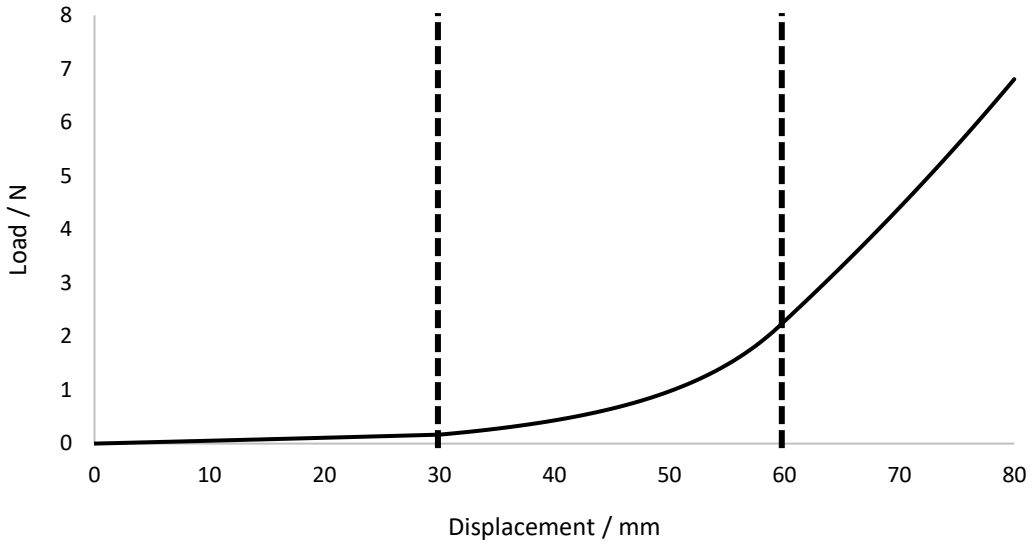

Figure 3.12. Load-displacement relationship of conical spring model using the piecewise approach.

3.2 Analysis and Discussion

The performance of the conical spring model was evaluated through several analyses. The analyses are grouped into three sections: mechanical behaviour, comparison to traditional MSM model, and interactive feedback.

3.2.1 Mechanical behaviour

3.2.1.1 Deformation behaviour

The purpose of the analysis is to simulate soft tissue deformation behaviours taken from literature, and to measure the accuracy of the simulation. Two reference data were directly adopted from Ahmadian et al. [71]. The study had observed several kinds of soft tissues and concluded that there are two general types of soft tissue deformations that can be separated according to the magnitude of the toe-region. The toe-region refers to the middle section of soft tissue deformation which is a nonlinear section. Soft tissues such as human breast and canine kidney with low nonlinearity at the toe-region belong to the first group. The second group, in contrast, has a higher nonlinearity along the toe-region.

The reference data were discretised into three sections that are linear, nonlinear and linear sections respectively. Intersections of these sections are the location of the break points. By using the information of the break points, the piecewise approach was implemented and the conical spring parameters were calibrated. To measure the behaviour of the conical spring model, a uniaxial compression load was applied

to a mass point at the surface of the model (see Fig. 3.13). The magnitude of the applied load and the resulting displacement were recorded during the loading process. The outcomes of the simulation are presented in Fig. 3.14 and Fig. 3.15.

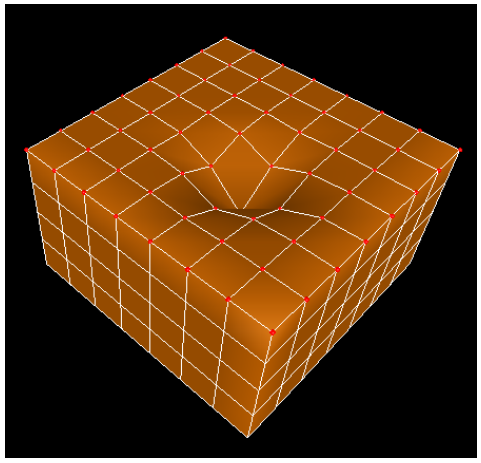

Figure 3.13. Image of the conical spring model during deformation.

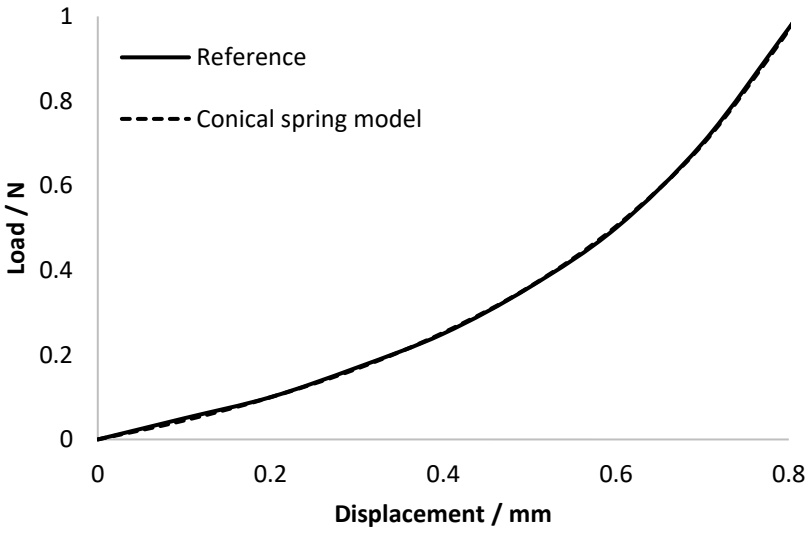

Figure 3.14. Deformation behaviour of conical spring model in comparison with the reference data of Type 1 [71].

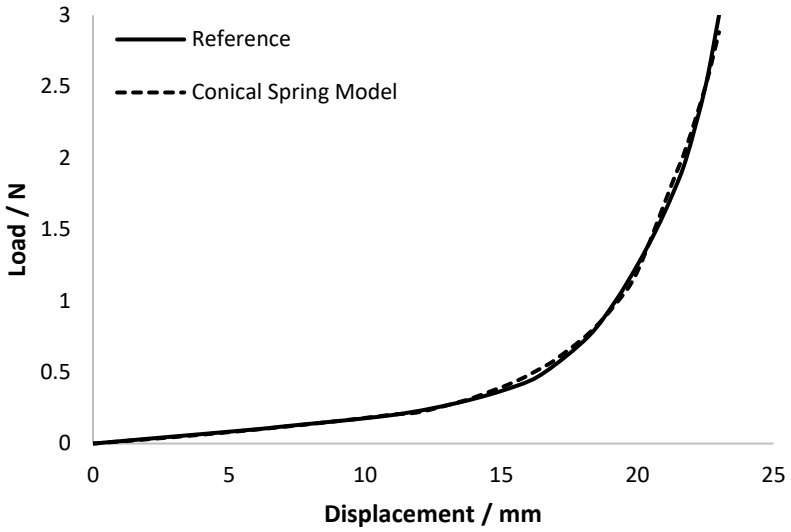

Figure 3.15. Deformation behaviour of conical spring model in comparison with the reference data of Type 1 [71].

Further analysis was conducted for a special case where soft tissues show a fully linear response. To replicate the case, a simple linear function was used to describe the linear response as in Eq. (3.36) where ℓ is set as 0.5. Since there is only a linear response, the reference data is considered as a single phase. The outcome is presented in Fig. 3.16 based on the calibration of the conical spring parameters.

$$y = \ell x \tag{3.36}$$

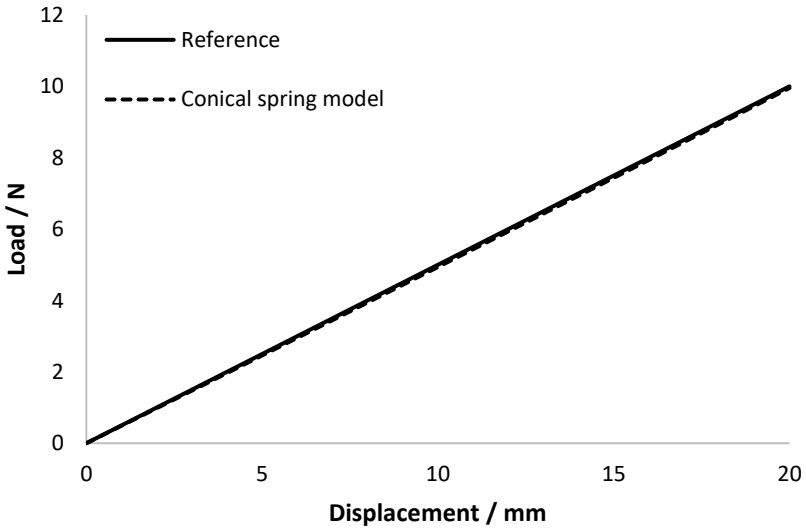

Figure 3.16. Deformation behaviour of conical spring model in comparison with the linear function given in Eq. (3.36).

The outcomes of the performance analysis show the conical spring model can simulate different types of deformation behaviours as described from the literature. In addition, the conical spring model is able to imitate a fully linear response that is a special case of soft tissue deformation. The different types of deformation are simulated by optimising the conical spring parameters. It shows the flexibility that conical spring formulation possesses. Moreover, the application of the piecewise approach provides a better accuracy of the simulation. As shown in Table 3.2, the average relative error of the conical spring model with respect to the reference data for all cases is less than 4%.

Table 3.2. The relative error of the proposed method in comparison with reference data.

Type of deformation	Reference	Average Relative Error (%)
Type I	Figure 3.14	1.89
Type II	Figure 3.15	3.75
Linear	Figure 3.16	1.18

Moreover, to show that the conical spring model can be used to simulate human organs, a kidney model based on the conical spring model was generated. Visualisations of the kidney model during compression are given in Fig. 3.17.

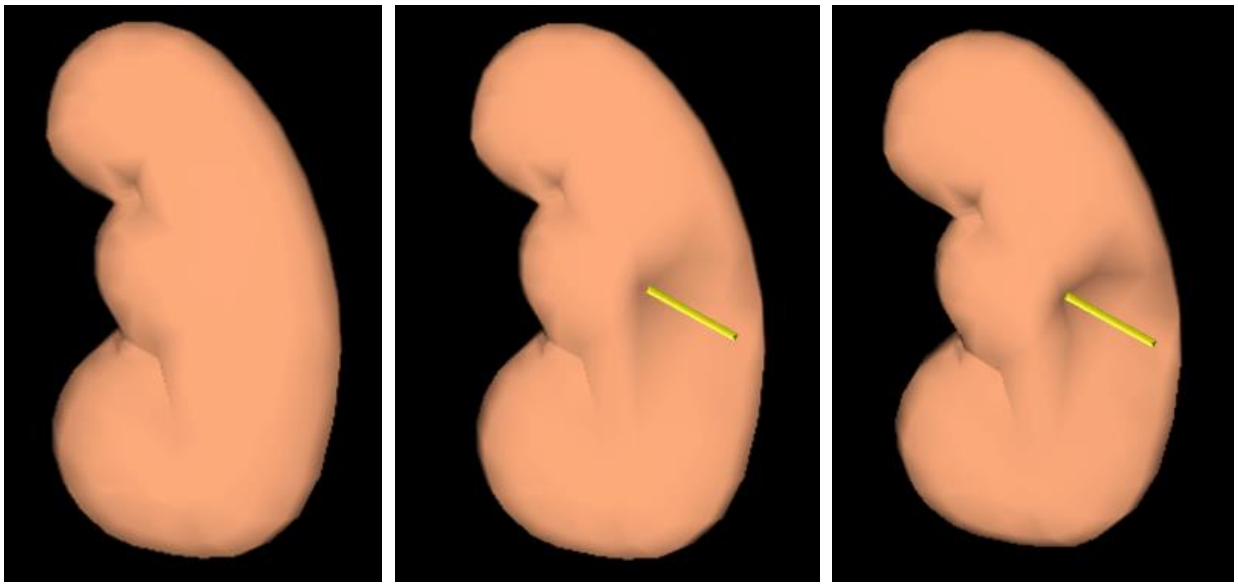

Figure 3.17. Deformation of a kidney model develops using conical spring model.

Despite the success of conical spring model in simulating different types of deformations, it has several limitations. First, the calibration of the conical spring parameters was conducted using the trial and error approach. The approach can be tedious and time consuming for a complex set of data. Second, the current calibration process is based on the hexahedral element configuration. Different configurations might give different response values due to different amount of conical springs attached to the selected node. Therefore, a generic optimisation approach needs to be developed to enhance the performance of the conical spring model.

Furthermore, the conical spring model is founded on the force propagation approach where the applied load is propagated to the next surrounding neighbours until a boundary is achieved. The approach eliminates the complexity in updating the stiffness matrix of the traditional mass spring model. However, the boundary of the propagation in the conical spring model is based on an arbitrary value that is controlled by the user. By using the arbitrary value, the propagation area can be over or under estimated resulting in unrealistic deformation. To get a proper propagation area, the area needs to be estimated by considering material properties and loading conditions.

3.2.1.2 Viscoelastic behaviour

To test the model for its viscoelastic property, first, the hysteresis test was conducted. A uniaxial compression load that is continuously increasing with time was applied to a mass point. The load was removed after a given period of time. The information regarding the load and the displacement was recorded throughout the test until the model was settled. The behaviour of the model during the hysteresis test is shown in Fig. 3.18a. The second experiment was conducted to verify the model for creeping property. A constant uniaxial load was applied on the model. The behaviour of the model was recorded for a period of time as plotted in Fig. 3.18b. Another analysis was conducted to study the force relaxation property. A constant displacement was loaded onto the model for a given period of time, and the force of the model during the process was recorded as presented in Fig. 3.18c.

A model is considered as viscoelastic if it simulates one of these properties, namely hysteresis, creep or force relaxation. Based on the hysteresis curve (see Fig. 3.18a), the loading path, which is represented by the solid line, and the unloading path, which is the dotted line, follow two distinct paths. The difference between the paths indicates energy lost during the process and it resembles the hysteresis phenomenon as observed in real tissues [15]. Creeping is the tendency of materials to deform permanently under the influence of continuous stresses, while materials with force relaxation will show reductions in the force

when it is subjected to a constant displacement. As can be seen in Fig. 3.18b, at the constant load, the model continues to deform at a small deformation rate. The observation is similar to the one reported by Mun et al. [60] and Choi et al. [75], which represent the creep property of soft tissues. Meanwhile, Fig. 3.18c demonstrates the force relaxation behaviour of the conical spring model. The reaction force shows a distinct delay resulting from force relaxation. During a sudden deformation, immediate response, in terms of the reaction force, was obsereved before it gradually declines. The observation resembles the result obtained in Basafa et al. [31].

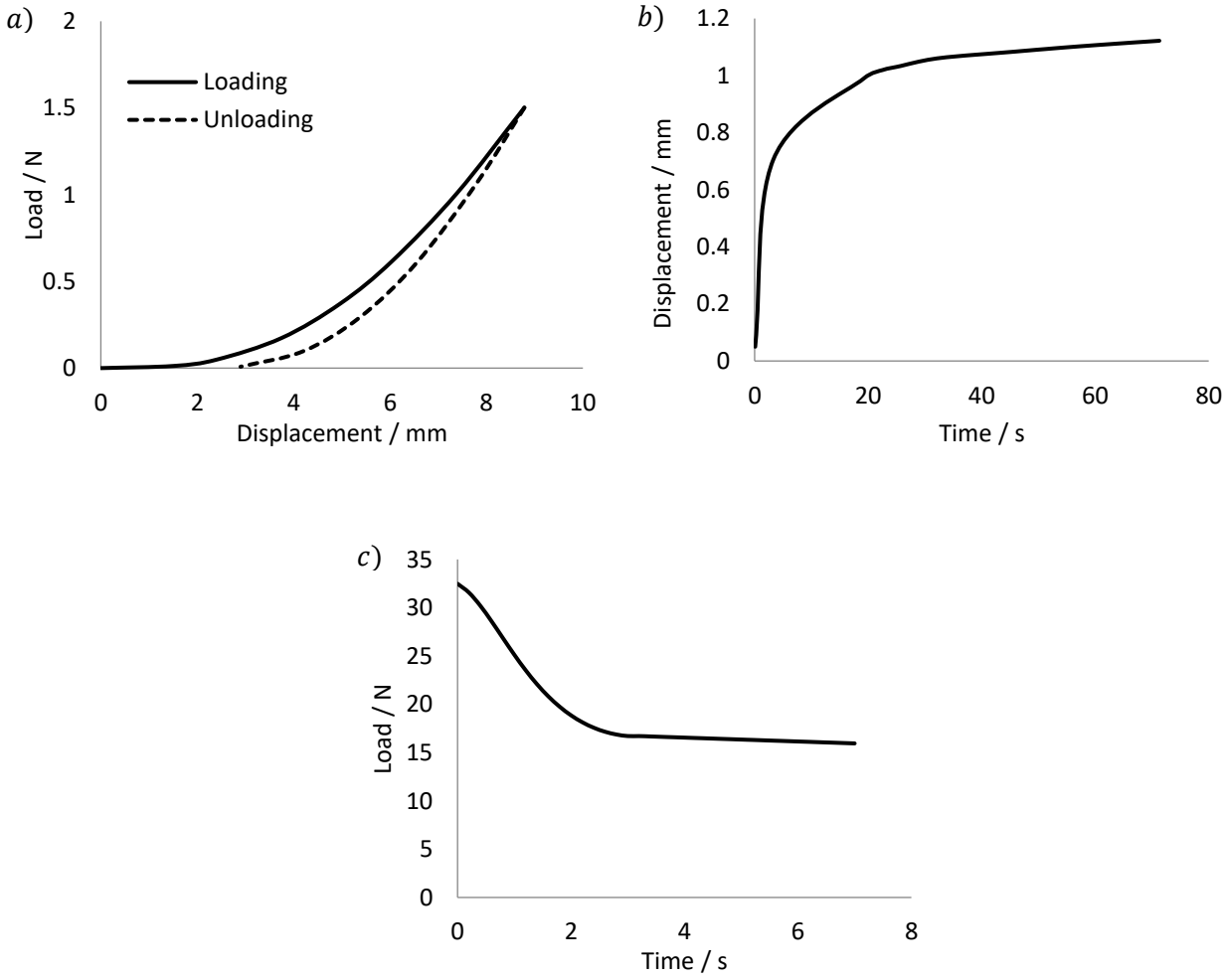

Figure 3.18. The viscoelastic properties of the conical spring model. a) Hysteresis, b) Creep, and c) Force relaxation.

The outcomes of the viscoelastic analysis suggest that the conical spring model is able to simulate the typical viscoelastic behaviour of soft tissues. However, the analyses were performed just to investigate the mechanical property of the model without any attempt to simulate any specific viscoelastic material. To achieve the purpose, it is adequate to tune the damping value as suggested by Sala et al. [74].

3.2.1.3 Anisotropic deformation

The next experiment was set up to create an anisotropic structure in the conical spring model. The anisotropic structure was developed by manipulating the properties of the conical springs. For example, in terms of the stiffness, the anisotropic property of soft tissues can be easily simulated by setting different wire diameters d in different directions. As illustrated in Fig. 3.19, two different springs were used which is differentiated by two lattice colours. The same conical spring parameters were used for both lattices except the size of the spring diameter d for the red and white springs were 0.5 mm and 1.5 mm respectively. This means that the conical springs in the red and white lattice have a different stiffness. Eq. 3.12 can be used to estimate the stiffness of each spring in regard to the largest coil diameter. The estimated stiffness value and details of the conical spring parameters are given in Table 3.3.

Table 3.3. Details of the conical spring parameters used for the red and white lattices.

Parameter	Red lattice	White lattice
D1	2	2
D2	8	8
Lo	90	90
G	50	50
d	0.5	1.5
n_a	3	3
Type	Telescopic	Telescopic
Estimated Stiffness	0.00064	0.05149

A normal load was applied to a single mass point located at the top of the model. The behaviour of the model is illustrated in Fig. 3.19 which shows that the greater deformation takes place on the red lattice than the white lattice because of the red lattice was less stiff than the white lattice. The results show that the deformation is dependent on direction, which indicates that the conical spring model can be used to simulate anisotropic property of the real soft tissues.

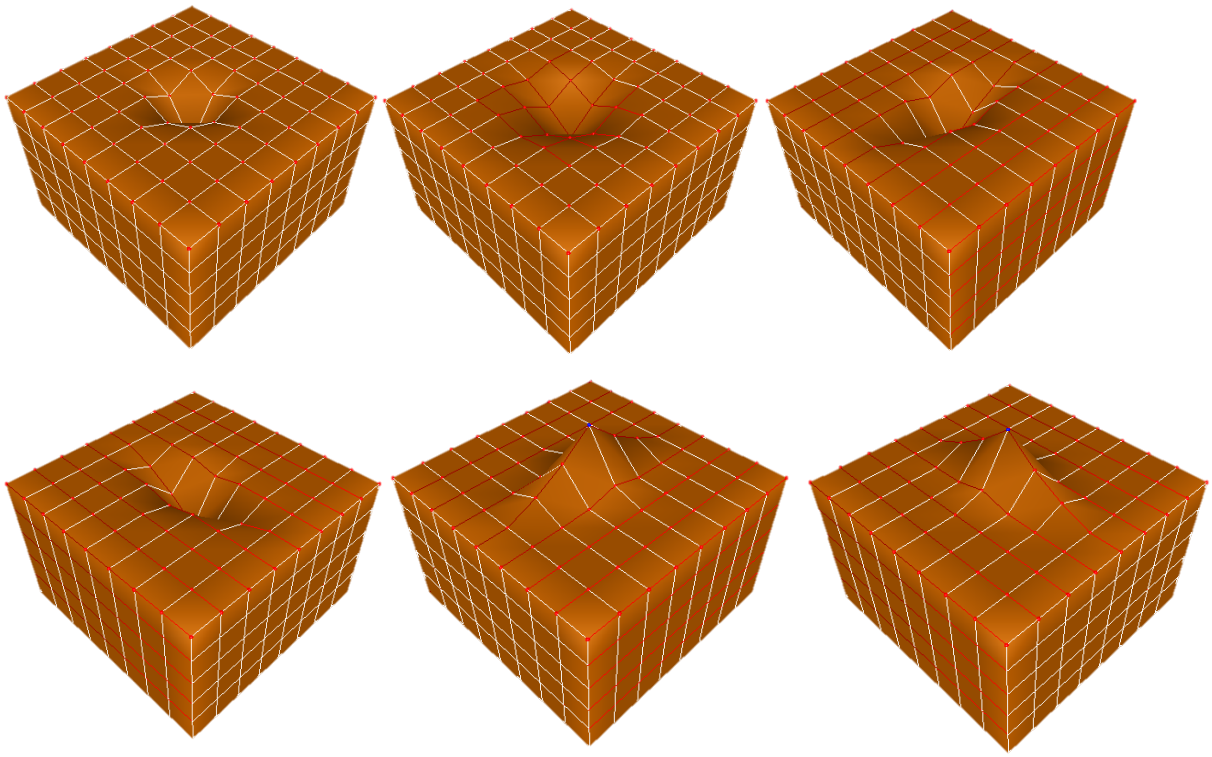

Figure 3.19. Anisotropic deformation of the conical spring model.

3.2.2 Comparison to experimental data

The conical spring model was further analysed by comparing its deformation behaviour with experimental data. The experimental data was obtained from compression test conducted on a soft tissue phantom which was generated using a special silicone mixture of Ecoflex 00-30. According to Spark et al. [106], the Ecoflex 00-30 has very high similarities to the real soft tissue properties. Hence, it is used widely as a soft tissue phantom [107]. Table 3.4 shows the technical specification of the Ecoflex 00-30 used to construct the soft tissue phantom.

Table 3.4. Material specifications of the Silicon Ecoflex 00-30.

Ecoflex® 00-30	**Mixed Viscosity**	**Specific Gravity**	**Specific Volume**	**Pot Life**	**Cure Time**
	3000 cps	1.07	26.0	45 min	4 hours

Shore Hardness	**Tensile Strength**	**100% Modulus**	**Elongation at Break %**	**Die B Tear Strength**	**Shrinkage (in./in.)**
00-30	200 psi	10 psi	900%	38 pli	<.001 in./in.

The compression test was conducted using the commercial INSTRON 50kN Compression machine as shown in Fig. 3.20. A moulded soft tissue phantom was placed on the specimen plate, and the compressive load was applied at the rate of 500 mm/min. The images of the process are presented in Fig. 3.21. The compression test was repeated for several specimens for precision. The outcome of the test is presented in Fig. 3.22.

Figure 3.20. The compression test using the commercial INSTRON Compression machine.

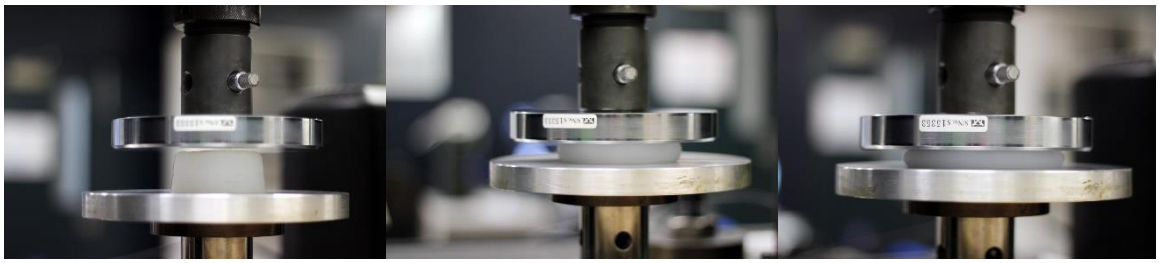

Figure 3.21. Images of the compression test on the soft tissue phantom (Ecoflex 00-30).

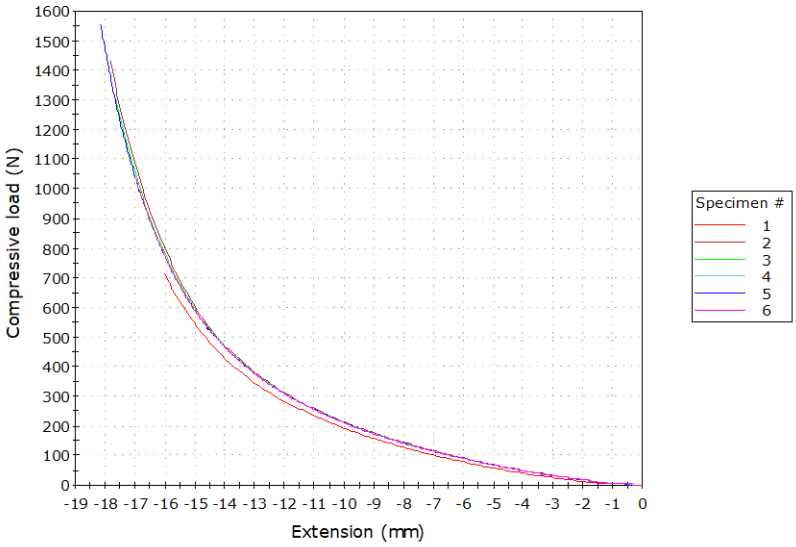

Figure 3.22. The outcome of the compression test on the soft tissue phantom for six specimens.

It can be seen that the soft tissue phantom has similar deformation behaviour with the first type of soft tissues described by Ahmadian et al. Using the data obtained from Specimen 5, calibration is made on the conical spring model to simulate the deformation behaviour. The calibration process was based on the trial and error approach. Initially, the total number of coils, the smallest coil diameter and the wire diameter were set to a constant value. Based on Section 3.1.6, the number of coils involved and the ratio between the smallest and the largest coil diameter were used to control the response behaviour, while the magnitude of the response is calibrated using the shear modulus value. The calibration process was terminated when the deformation of conical spring model agrees with the experimental data within 10 % of relative error. The outcome is presented in Fig. 3.23.

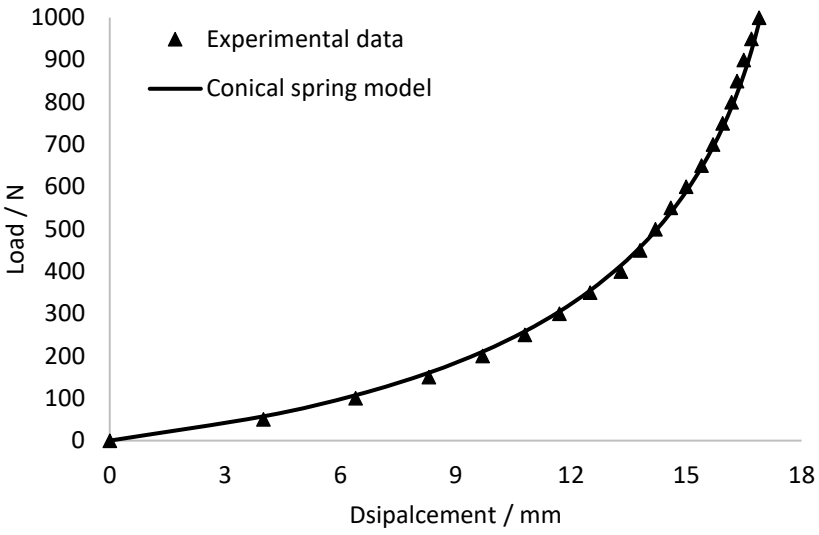

Figure 3.23. Deformation behaviour of the conical spring model in comparison to the experimental data obtained from the compression test on the soft tissue phantom of Specimen 5.

The outcome shows that the conical spring model can simulate the deformation behaviour of the soft tissue phantom. Despite the calibration process is based on the trial and error approach, similar behaviour with relative error of less than 10 % was obtained. The percentage of the relative error can be further reduced with more accurate calibration methods, such as genetic algorithm and simulated annealing.

3.2.3 Comparison to traditional MSM

In this section, the performance of conical spring model was compared to the traditional MSM model in terms of deformation behaviour and computational time. A simple cubical model consist of 320 nodes was generated. The traditional MSM model was developed in the same manner as the conical spring model except the spring force is replaced by the linear Hooke's law equation. The deformation behaviour of both models is recorded in Fig. 3.24. It can be seen that the conical spring model improved the traditional MSM model by providing nonlinear deformation. As the conical spring model provides more internal resistance at a larger displacement, greater load is required to displace the model.

However, in terms of computational time, the time clocked by the conical spring model was higher than the traditional method. The computational time was recorded by measuring the update time of the simulation, and as shown in Table 3.5, the difference is about seven milliseconds. Although both models were developed in the same manner, the models are different in terms of the mathematical treatment on the spring force calculation. The traditional MSM model has the advantage since the simple linear

Hooke's law equation was used. Yet, it is limited to linear deformation which is not representing the general soft tissue behaviour. On the other hand, while the spring force for the conical spring model is more complex, nevertheless, a more accurate simulation can be obtained. Hence, the seven milliseconds different can be considered as relatively small in comparison to the ability of achieving better accuracy.

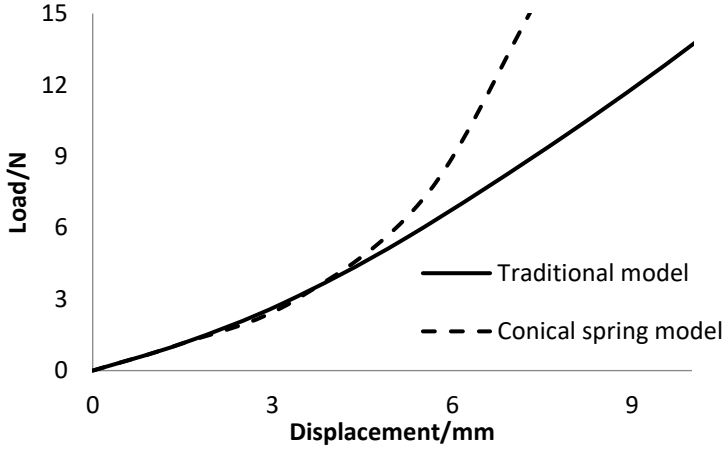

Figure 3.24. Deformation behaviour of traditional MSM and the conical spring model.

Table 3.5. Update time of the conical spring model and traditional MSM.

MSMs	Number of nodes	Update time (s)
Conical spring model	320	0.090
Traditional MSM	320	0.083

3.2.4 Interactive feedback

Moreover, the interactive deformation of virtual human organs was achieved with the help of SOFA framework software [108]. SOFA is an open source framework that allows independently developed algorithms to interact together within a common simulation. This application allows the real-time interaction with numbers of the available model. In terms of a human organ, liver is an example.

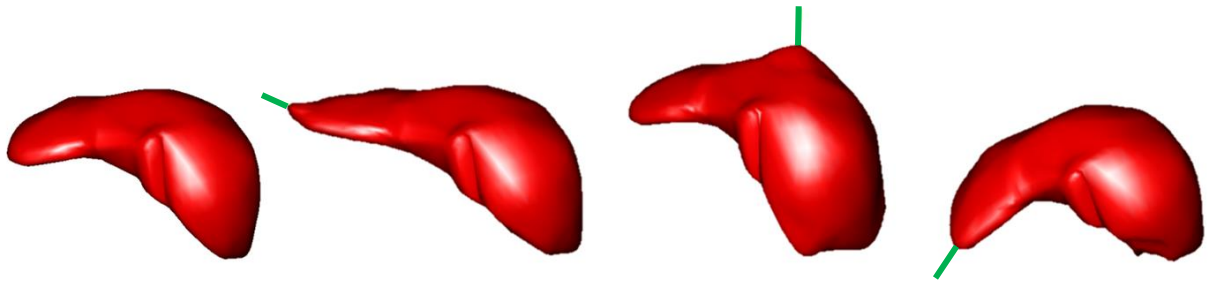

Figure 3.25. Implementation of the proposed method in SOFA open source. Image of the original liver model followed by deformed model.

Modifications on the header and inline files were made to implement the proposed method in the SOFA framework. Specifically, the files related to the Spring-Force were modified using the conical spring equation. Fig. 3.25 shows the deformations of the modified liver model consist of 507 nodes. With the help of SOFA framework, the result shows that the proposed method can be run at a real-time interactive phase which is required for haptic feedback.

3.3 CHAPTER SUMMARY

The purpose of the current study is to provide a new framework for the exploration of soft tissue deformation. Instead of oversimplifying the soft tissue deformation as nonlinear, this study suggests the deformation behaviour is determined with regards to the three phases of soft tissue deformation. To model the deformation phases individually, piecewise approach using conical spring formulation has been introduced. The outcome shows that the proposed method can simulate the three phases of soft tissue deformation. Moreover, by using the stiffness variation that can be generated by conical spring, the proposed method has more flexibility in modelling different types of soft tissue deformation with high accuracy and within a real-time interaction. Further, the proposed method also exhibits the typical mechanical properties of soft tissues that are viscoelastic and anisotropic.

4 LOCALISED REGION USING ESTIMATION OF DISPLACEMENT FOR ISOTROPIC MATERIAL WITH KNOWN INPUT LOAD

The mass-spring method (MSM) and finite-element method (FEM) are two common physics-based modelling techniques. MSM focuses on the computational performance which models a deformable object as a system of mass points connected by springs. In contrast, FEM concentrates on the modelling accuracy. It models the mechanical behaviours of soft tissues based on rigorous mathematical analysis of continuum mechanics. However, both techniques calculate the deformation based on the entire object model, which is time-consuming, particularly for a model with a large number of elements.

Soft tissue deformation commonly occurs within a localised region. As the effect of the deformation outside the local region is small, it can be ignored in real practice [109]. Accordingly, modelling of soft tissue deformation by focusing on the affected local region rather than the entire model, can significantly reduce the computational load. However, random localisation can disturb the accuracy of the simulation. Hence, the purpose of localisation is not just to improve the computational performance, but it should also preserve the accuracy of the modelling.

This chapter presents a new methodology to generate a more comprehensive localised region. Estimation methods are established based on linear elastic theory to estimate displacement distribution inside the soft tissues. By using a particular displacement value, the boundary of the localised region is determined in accordance with a distance from the contact surface of the soft tissues. The method considered the material properties of soft tissues, and the magnitude of the input load.

4.1 ANALYSIS ON DISPLACEMENT DISTRIBUTION

Displacement distribution inside an elastic object subjected to an external load was studied with reference to a finite element model. The finite element model was developed using a commercial software called ABAQUS. A cubical body consisting of hexahedral elements was developed using the linear and isotropic material where its elastic modulus and Poisson ratio were set as 90 kPa and 0.4 respectively. The cubical body was held fixed at all its faces, except at the loading surface. A normal load was applied onto the body in the form of uniform pressure acting on a circular area at the centre of the surface. The radius of the circular area is 0.1 m while the normal pressure is 10 Pa.

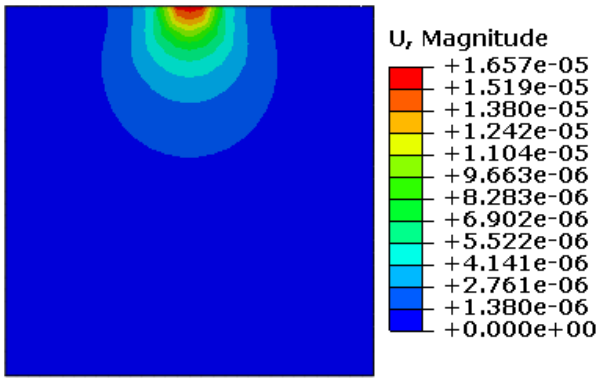

Figure 4.1. Total displacement distribution inside isotropic body subjected to normal loading.

Fig. 4.1 presents the result of the finite element model in the form of total displacement *U*. The result is presented using a sectional view which shows the displacement at the centre of the cubical body. It can be seen that the displacement value gradually reduces further away from the contact point. The displacement is distributed in the form of wave pattern. It can also be observed that the displacement distribution is only taking place in a small area. It indicates the affected area during deformation is small in comparison to the whole body. Besides, the outcome also shows that under a normal loading, the affected area has a larger value for its depth than its width.

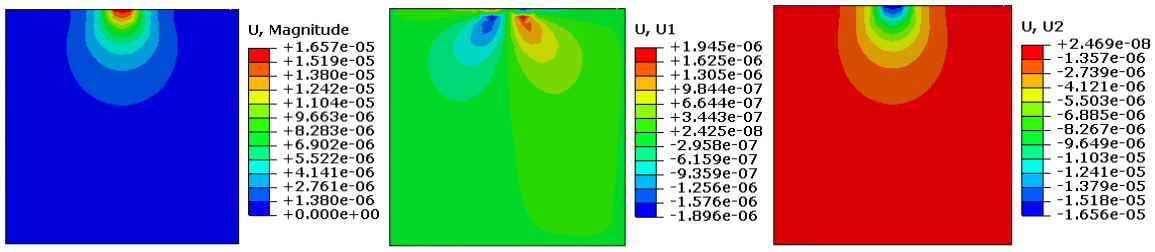

Figure 4.2.Total, horizontal and vertical displacement components of the isotropic body subject to normal loading.

Further analysis was carried out by observing components of the displacement. Fig. 4.2 shows the results of the observations. In the figure, *U1* and *U2* indicate horizontal and vertical displacement component respectively. It is apparent that the vertical displacement is more dominant than the horizontal displacement. This is due to the direction of the input load that is in the normal direction. In terms of the magnitude of the input load, as illustrated in Fig. 4.3, different displacement value is plotted along the vertical axis underneath the contact point which suggests larger input load will produce larger displacement distribution.

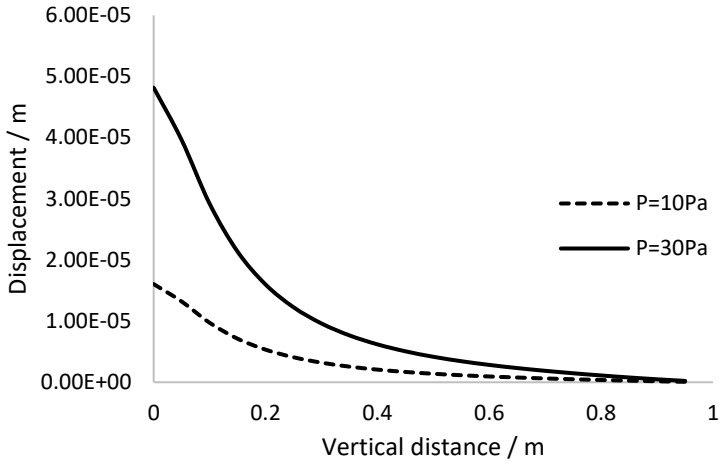

Figure 4.3. Total displacement distribution of FEM model at different input load measured vertically underneath the contact point.

The effects of material properties, particularly the effect of elastic modulus and Poisson ratio on the displacement distribution were examined. These two are the most common properties used to describe material behaviour. As illustrated in Fig. 4.4, total displacement was recorded along the vertical axis underneath the contact point using different elastic modulus values. It is seen that the displacement is larger for a smaller elastic modulus value. The displacement value is different at the contact point as well as along the vertical axis. It shows that for a larger elastic modulus, the material becomes stiffer leading to a smaller deformation. Hence, smaller displacement was recorded.

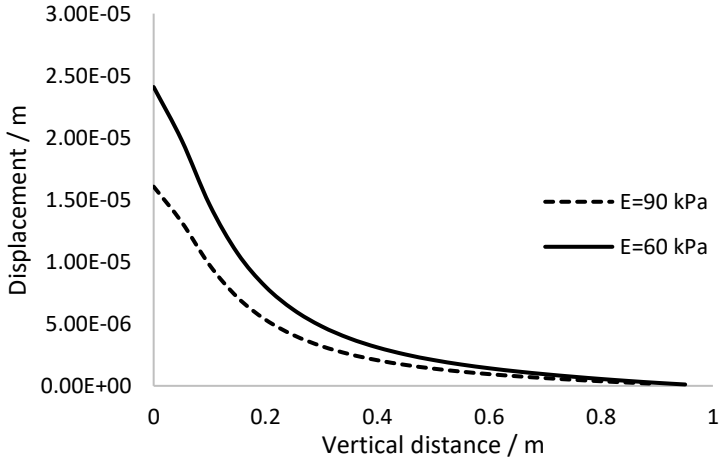

Figure 4.4. Total displacement distribution of FEM model at different elastic modulus measured vertically underneath the contact point.

On the other hand, the Poisson ratio has different effect on the displacement distribution. As shown in Fig. 4.5, different Poisson ratio values were used to plot the total displacement value along the vertical

axis underneath the contact point and it causing only a small variation in the total displacement value. However, when plotting the total displacement value along the surface of the model, the effect of the Poisson ratio is significant which is shown in Fig. 4.6. The result suggests that a larger displacement is recorded for a smaller Poisson ratio.

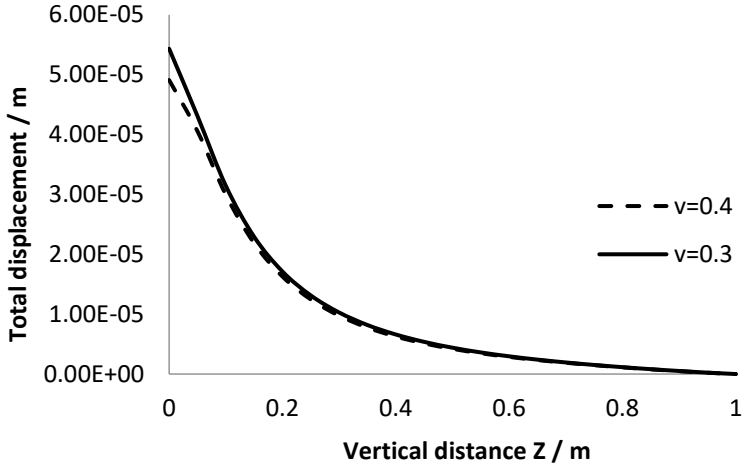

Figure 4.5. The total displacement of the model using different Poisson ratio value measured along vertical axis underneath the contact point.

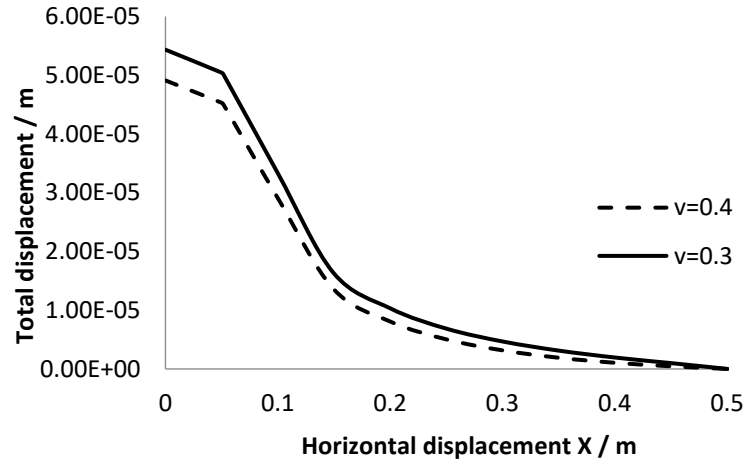

Figure 4.6. The total displacement of the model at different Poisson ratio value measured along the surface parallel to the contact point.

Several conclusions can be made from the behaviour analysis. First, the displacement inside an elastic body is related to the input load and it is proportional to the magnitude of the input load. Second, the material properties, the elastic modulus and Poisson ratio, affected the displacement distribution where the displacement value becomes smaller in a stiffer material. The findings indicate the important factors need to be considered to generate a proper localised region.

4.2 METHOD

Load applied on soft tissue surface creates displacements within the soft tissue mass. In this regard, the complexity of soft tissues make the estimation of the induced displacement at a point of a particular depth in a soft tissue mass challenging [15]. However, by treating soft tissues as an isotropic and elastic linear material, displacement distribution inside the semi-infinite body of soft tissues can be obtained in various ways. The Kelvin, Boussinesq and Cerruti solutions are some of the well-known methods. The Kelvin method solves the case where one point inside the elastic body is subjected to a normal force. Mindlin extended Kelvin's work to develop solutions for the tangential and normal force. The Boussinesq and Cerruti methods are ones where a point on the surface of an elastic half-space is subjected to force. To be specific, the Boussinesq method solves for the force in a normal direction, while Cerruti provides a solution for tangential loading.

In most cases, the interaction between surgical tools and soft tissues take place on the surface of the soft tissue and in a normal direction. For example, a pure normal loading is used in the indentation process. In this regards, the Boussinesq method was used in this study as it focuses on the case where the interaction happens on the surface and in normal direction.

The Boussinesq method is derived by solving the Navier's equation of elasticity using the method of potentials. The Navier's equation of elasticity is described as

$$\mu\nabla^2\boldsymbol{u}_i + (\lambda+\mu)\frac{\partial e_v}{\partial x_i} + \boldsymbol{F}_i = 0 \tag{4.1}$$

where the pair of constant λ and μ are called Lame's constants. The term μ is also referred to as the shear modulus G. The terms $\boldsymbol{u_i}$ and $\boldsymbol{F}_i$are represent the displacement and body force component respectively. The remaining e_v denotes the bulk strain and x_i denotes the Cartesian coordinates. The operation ∇^2 is the Laplace's operator represented by

$$\nabla^2 = \frac{\partial^2}{\partial x_1^2} + \frac{\partial^2}{\partial x_2^2} + \frac{\partial^2}{\partial x_3^2} \tag{4.2}$$

In the absence of the body force, Eq. (4.1) can be written in vector form as

$$(\lambda+G)\overline{\nabla}(\overline{\nabla}\cdot\overline{\boldsymbol{u}}) + G\,\nabla^2\overline{\boldsymbol{u}} = 0 \tag{4.3}$$

where $\overline{\nabla}$and $(\overline{\nabla}\cdot)$ are the gradient and divergence operator. The term $\overline{\boldsymbol{u}}$ denotes the displacement vector.

According to Helmholtz's theorem [110], the vector field $\overline{\boldsymbol{u}}$ can be written in terms of its scalar $\phi = (x_1, x_2, x_3)$ and vector $\overline{\boldsymbol{\psi}} = (x_1, x_2, x_3)$ potentials as follows

$$\overline{\boldsymbol{u}} = \overline{\nabla}\,\phi + \overline{\nabla}\times\overline{\boldsymbol{\psi}} \tag{4.4}$$

where $(\overline{\nabla}\times)$ is the curl operator. Substituting the potentials in Eq. (4.3), the Navier's equation in terms of the potentials is given as

$$(\lambda + 2G)\overline{\nabla}(\nabla^2\phi) + G\overline{\nabla}\times\nabla^2\overline{\boldsymbol{\psi}} = 0 \tag{4.5}$$

Any set of potential functions ϕ and $\overline{\boldsymbol{\psi}}$ which satisfies Eq. (4.5) will produce, when substituted into Eq. (4.4), a displacement field $\overline{\boldsymbol{u}}$ which satisfies Navier's equations.

The Boussinesq method solved Eq. (4.4) by using the Neuber-Papkovich representation [110]. This representation uses a combination of harmonic functions to represent the displacement vector $\overline{\boldsymbol{u}}$. The expression is given as

$$2G\overline{\boldsymbol{u}} = \overline{\boldsymbol{A}} - \overline{\nabla}\left[B + \frac{\overline{\boldsymbol{A}}\cdot\overline{\boldsymbol{X}}}{4(1-v)}\right] \tag{4.6}$$

where $\overline{\boldsymbol{A}}$ is a vector field, B a scalar field, and $\overline{\boldsymbol{X}}$ is the position vector. Substituting Eq. (4.6) into Eq. (4.3) yields

$$G\nabla^2\overline{\boldsymbol{A}} - (\lambda + 2G)\overline{\nabla}(\nabla^2 B) - \left(\frac{\lambda + G}{2}\right)\overline{\nabla}(\overline{\boldsymbol{X}}\cdot\nabla^2\overline{\boldsymbol{A}}) = 0 \tag{4.7}$$

Eq. (4.7) is satisfied if

$$\nabla^2\overline{\boldsymbol{A}} = 0 \tag{4.8}$$

$$\nabla^2 B = 0 \tag{4.9}$$

Therefore, for the vector field $\overline{\boldsymbol{A}}$ and the scalar field B, any harmonic functions A_1, A_2, A_3, and B can be substituted in Eq. (4.6) and the resulting $\overline{\boldsymbol{u}}$ will satisfy Navier's equations.

Solution of the Boussinesq method for displacements inside a linear elastic body is given by

$$u_x = \frac{P}{4\pi G}\left[-\frac{(1-2v)\,l_x}{\rho(\rho + l_z)} + \frac{l_x\, l_z}{\rho^3}\right] \tag{4.10}$$

$$u_y = \frac{P}{4\pi G}\left[-\frac{(1-2v)\,l_y}{\rho(\rho + l_z)} + \frac{l_y\, l_z}{\rho^3}\right] \tag{4.11}$$

$$u_z = \frac{P}{4\pi G\rho}\left[2(1-v) + \frac{{l_z}^2}{\rho^2}\right] \tag{4.12}$$

where u_i represents the displacement component in respective direction, P denotes the normal load applied at the origin of the Cartesian coordinates, G symbolises the shear modulus, and v is the Poisson ratio. The terms l_x, l_y and l_z indicate distance of the point from the origin in respective directions, while ρ is given as

$$\rho = \sqrt{{l_x}^2 + {l_y}^2 + {l_z}^2} \tag{4.13}$$

Detailed derivation of Eq. (4.10) to Eq. (4.12) is given in Appendix 1.

4.3 LOCALISED REGION

The purpose of localised regions is to identify a small region that is significantly affected by the external load in order to avoid the computations on the entire body. Localised regions can be generated by finding distances from the contact point (origin) to locations where displacement is small and insignificant. The small displacement is called $\boldsymbol{u_{min}}$. Once the distances are obtained, the half-space concept is used to identify the localised region.

The illustration of the proposed localised region is presented in Fig. 4.7. The localised region is developed in the form of a rectangular volume which is defined by three parameters; width, length and depth. The length is measured in x direction and the width is in y direction, while the depth is in z direction. The length and width are measured on the surface while the depth is measured along the vertical axis of the model.

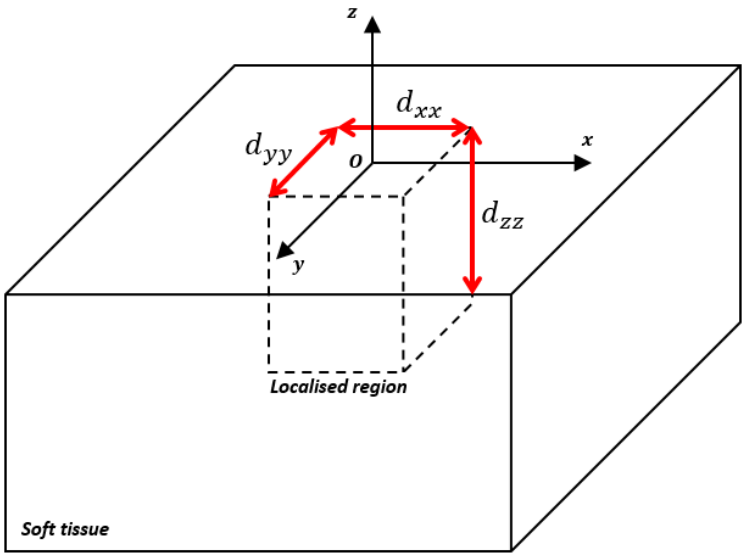

Figure 4.7. Illustration of the localised region.

The analysis of the displacement distribution in FEM model shows that under a normal loading, vertical displacement is more significant than the other components. Based on the finding, simplification can be made where only the vertical displacement is used to determine the localised region. In this regards, the width and length of the localised region are determined from vertical displacement value measured at the surface, while the depth of the localised region is calculated using vertical displacement measured in vertical direction underneath the contact point. The displacement equations in respective direction are given as

$$u_{z\ at\ surface\ x} = \frac{P_N}{4G\pi l_x}[2(1-v)] \tag{4.28}$$

$$u_{z\ at\ surface\ y} = \frac{P_N}{4G\pi l_y}[2(1-v)] \tag{4.29}$$

$$u_{z\ at\ depth\ z} = \frac{P_N}{4G\pi l_z}[1+2(1-v)] \tag{4.30}$$

Rewritting Eq. (4.28) to Eq. (4.30) in terms of distance from the contact point to the location where the $\boldsymbol{u}_{\boldsymbol{min}}$ occurs gives

$$l_x = \frac{P_N}{4G\pi u_{\ min}}[2(1-v)] \tag{4.31}$$

$$l_y = \frac{P_N}{4G\pi u_{\ min}}[2(1-v)] \tag{4.32}$$

$$l_z = \frac{P_N}{4G\pi u_{min}}[1 + 2(1 - v)] \tag{4.33}$$

where l_i, $i = x, y, z$, is the distance where the $\boldsymbol{u_{min}}$ occurs in the respective directions. The value of $\boldsymbol{u_{min}}$ is controlled by the user. Therefore, the parameters of the localised region are given as

$$d_{xx} = 2l_x \tag{4.34}$$

$$d_{yy} = 2l_y \tag{4.35}$$

$$d_{zz} = l_z \tag{4.36}$$

The process of generating the localised region is given in Fig. 4.8.

Step 1	Pre-computation i. Set the material properties for the model ii. Set the intended value of $\boldsymbol{u_{min}}$
Step 2	Computation i. Determine the loading direction ii. Determine the magnitude of the applied load iii. Solving Eq. (4.31) to Eq. (4.33) for distance where u_{min} occurs iv. Generate the localised region using the half-space concept

Figure 4.8. The process of generating localised region.

4.4 ANALYSIS

4.4.1 Behaviour analysis

The analysis on the FEM model shows that the displacement distribution is affected by material properties and magnitude of the input load. In this section, analysis was conducted on the proposed localised region to show that it also exhibits the same behaviour as the FEM model. The first analysis focuses on the magnitude of the input load. The main idea is to find distances where the small displacement value occurs. In this analysis, the small displacement $\boldsymbol{u_{min}}$, was set at 0.002 m for all directions. Then, by using Eq. (4.31) to Eq. (4.33), the distance where the $\boldsymbol{u_{min}}$ occurs was calculated for all directions. Details of the parameters used and the results are given in Table 4.1.

Table 4.1. Parameters of the localised region at different input load.

Parameter	Input load / N	Elastic modulus / kPa	Poisson ratio	Distance / m
l_x & l_y	20	30	0.4	0.089
l_z				0.163
l_x & l_y	40	30	0.4	0.193
l_z				0.331
l_x & l_y	60	30	0.4	0.306
l_z				0.497

It can be observed that the distance of the small displacement occurs is different between the horizontal and vertical parameters which resembles the FEM model. The vertical parameter has a larger value which means that the localised region is longer in the vertical direction. Moreover, it is seen that different distance values are recorded at different input load. The small displacement value occurs further for a larger input load. The effect of the input load can be viewed clearly by plotting the vertical displacement value along the vertical axis underneath the contact point as given in Fig. 4.9. It can be seen that the larger input load produces a larger displacement value which suggests that the size of the localised region will be larger when a larger load is applied.

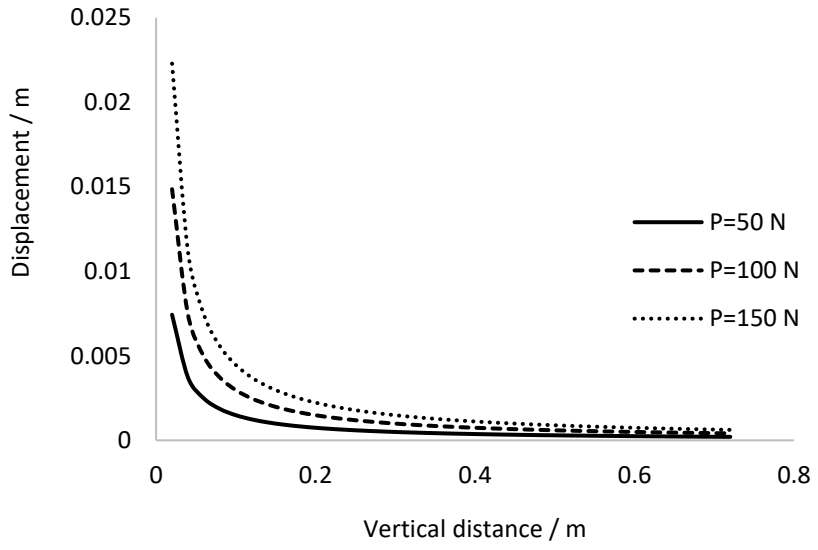

Figure 4.9. Vertical displacement along the vertical axis underneath the contact point.

The analysis was extended to see the effect of material properties on the proposed localised region. By using the same concept, the distance where the small displacement $\boldsymbol{u}_{\boldsymbol{min}}$ occurs in vertical direction was calculated using different elastic modulus values. The small displacement $\boldsymbol{u}_{\boldsymbol{min}}$ was set as 0.002 m for all directions. It can be seen in Fig. 4.10 that different distance is recorded at different elastic modulus values. The distance where the $\boldsymbol{u}_{\boldsymbol{min}}$ occurs became smaller as the elastic modulus is larger. This indicates that the localised region becomes smaller for a stiffer material.

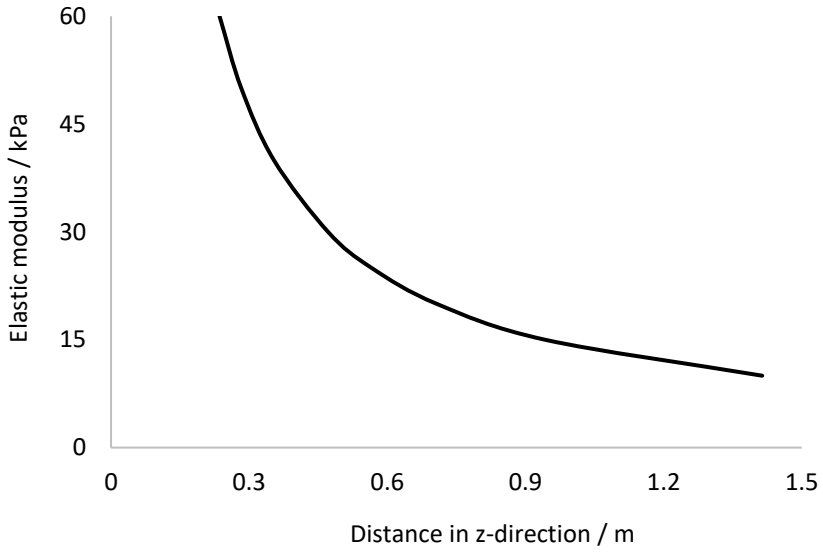

Figure 4.10. The relationship between the elastic modulus and distance of the small displacement u_{min}.

Moreover, for the effect of Poisson ratio, displacement distribution under different Poisson ratio values is recorded along the vertical distance underneath the contact point and along the surface of the model. The outcomes are presented in Figs. 4.11(a) and 4.11(b) respectively. It shows that the effect of Poisson ratio on the proposed method is similar to the FEM model. Poisson ratio has a small effect on displacement measured vertically while the effect is more significant for displacement measured horizontally. As shown in Fig. 4.11(b), displacement value along the horizontal direction is larger for a smaller Poisson ratio. This means that the localised region will have larger horizontal parameters for material with a smaller Poisson ratio.

The outcomes of the analyses indicate that displacement distribution of the proposed localised region exhibits the same properties as the one in FEM model. Displacement distribution of the proposed localised region depends on the magnitude of the input load as well as the material properties.

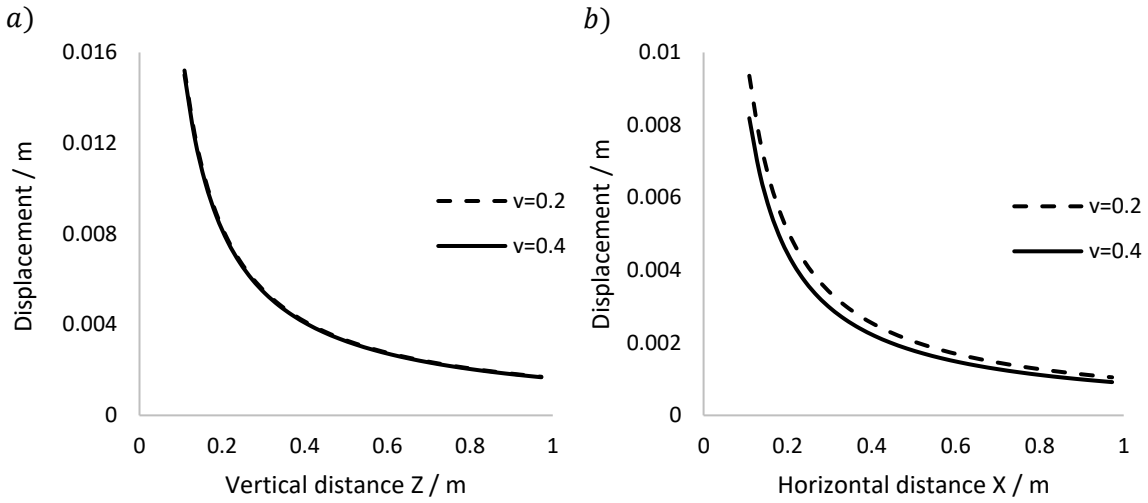

Figure 4.11. Displacement distribution of the model using different Poisson ratio values measured along: a) The vertical axis underneath the contact point (vertical), and b) The surface parallel to the contact point (horizontal).

4.4.2 Performance analysis

In Section 4.4.1, it is found that the behaviour of the displacement distribution of the proposed method matches the behaviour recorded in the FEM analysis. In this section, two analyses have been conducted to study the performance of the method in comparison to FEM result.

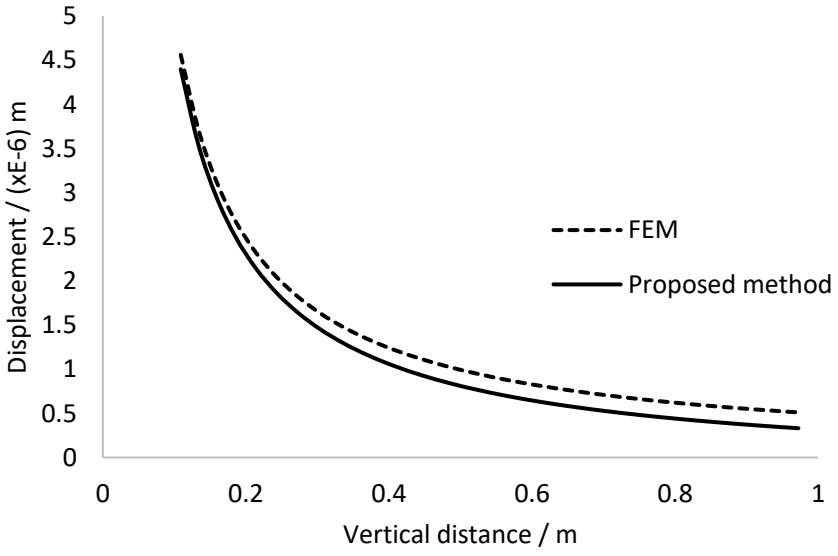

Figure 4.12. The displacement distribution recorded by the proposed method and the FEM simulation.

In terms of displacement distribution, comparison between the proposed method and the FEM data is given in Fig. 4.12. It can be seen that in general the behaviour of displacement distribution is the same for the FEM result and the proposed method. However, the results are varied largely further away from the

contact point. The average relative error between the data is around 17.3% with minimum and maximum error of 3.5% and 32.9% respectively. Despite the large maximum error that occurs at the furthest point of comparison, it can be neglected because the location of the point is almost one meter from the surface and the value of the displacement that occurs here is too small.

For the second comparison, the distance at which the small displacement $\boldsymbol{u}_{\boldsymbol{min}}$ occurs, which was obtained from the proposed method was compared to the static FEM result in order to study the performance of the proposed localised region. The static FEM result for a linear and isotropic model was obtained from the ABAQUS software. A normal load was applied on the FEM model, and displacement value along the surface and the vertical axis underneath the contact point was recorded. Two comparisons were made at different elastic modulus values. For a particular $\boldsymbol{u}_{\boldsymbol{min}}$ value, the distance where it occurs in the FEM model and the analytical model was recorded. Due to the isotropic properties, horizontal parameters d_{rr} and $d_{\partial\partial}$ are considered as similar. The details of the parameters used and the comparison are given in Table 4.2.

Table 4.2. The parameters used and the outcomes of the comparison between the proposed method and FEM.

Case	E (kPa)	v	Load (N)	Parameter	$\boldsymbol{u}_{\boldsymbol{min}}$	Distance (m)		Relative error (%)
						Analytical	FEM	
Case 1	30	0.4	50	d_{rr}	0.0022	0.1955	0.2	2.3
				d_{zz}	0.0025	0.3312	0.3	10.4
Case 2	60	0.4	50	d_{rr}	0.0011	0.1978	0.2	1.1
				d_{zz}	0.0018	0.2231	0.2	11.5

Based on Table 4.2, the estimation of the horizontal parameter d_{rr} is more accurate than the vertical parameter d_{zz}. The relative error that is the comparison between the result obtained from FEM simulation and the proposed method of the horizontal estimation is less than 3%, while estimation of the vertical parameters in both cases is less than 12%. Even though the proposed method is not so accurate, yet, it indicates a promising result. Besides, it should be noted that there might be some errors in the FEM analysis as the normal load is applied only on one node. This condition might lead to load concentrated in a very small area which is a common problem for the ABAQUS software.

To further study the performance of the localised region, the method was implemented in the conical spring model described in Chapter 3. A simple cubical structure of the conical spring model consisting of

68921 nodes was generated. A normal load was applied to a node at the surface of the conical spring model. Two models were generated using two different small displacement values. The first model has a smaller localised region where the small displacement value was set at 0.02 m for all directions. The number of nodes involved during calculation was 90 out of the total 68921 nodes. For the second model, the small displacement value was 0.002 m for all directions, and the number of nodes involved was 216 from the total. Both models were subjected to the same load of 5 N, while the elastic modulus and Poisson ratio were assigned as 30 kPa and 0.4 respectively. Fig. 4.13 shows that deformation area of the first model is smaller than the second model due to fewer nodes involved in the deformation. Moreover, in terms of computational performance, the first model also has a better performance. As shown in Table 4.3, in comparison to the whole model, the model with the proposed localised region has a superior computational performance, and the level of the superiority depends on the size of the localised region as presented in Fig. 4.14.

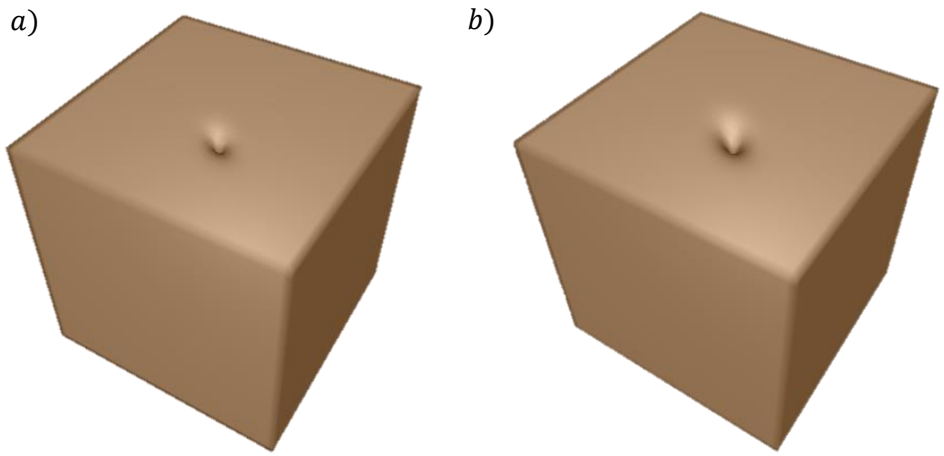

Figure 4.13. Deformation of conical spring model with different sizes of localised region, a) Model 1 (small) and b) Model 2 (large).

Table 4.3. Computational performance of conical spring model with different sizes of localised region.

Model	Number of nodes involved	u_{min} (m)	Rendering time (FPS)
Model 1	90	0.02	97
Model 2	216	0.002	91
Model without localised region	68921	-	3

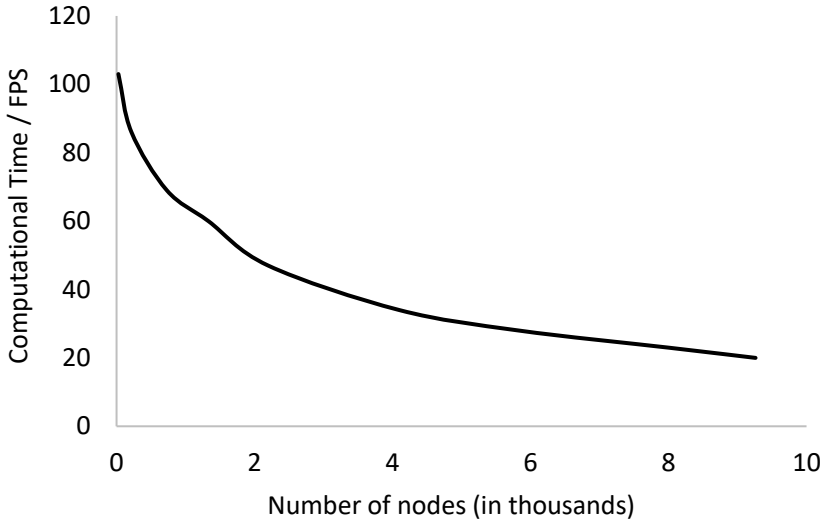

Figure 4.14. The computational performance of the proposed localised region with regards to the size of the localised region interpreted by the number of nodes.

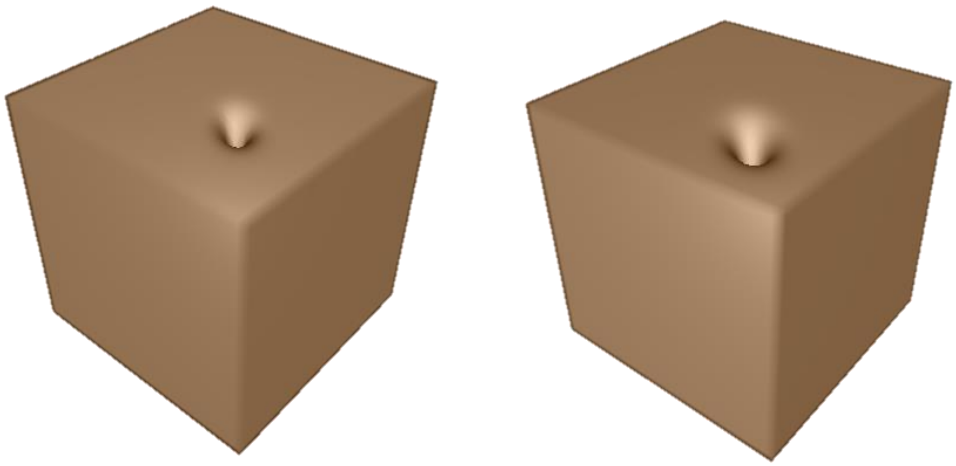

Figure 4.15. Deformation of conical spring model with different input loads, a) Load = 10 N, and b) Load = 20 N.

The proposed localised region is directly related to the magnitude of the input load. This indicates that the size of the localised region will be adjusted based on the value of the input load. In surgical simulations, the input load will be updated at each time step. Since the localised region is generated based on the input load, therefore, the localised region will also be updated at each time step. To demonstrate this ability, Fig. 4.15 presents the deformation of the conical spring model at different input loads but with a similar small displacement value of 0.002 m. The small displacement value was set equal for all directions. The first model was subjected to 10 N while the second model was subjected to 20 N. It is seen that the larger load creates a larger deformation area. Even though similar small displacement value is used, both

models have a smooth deformation. It is because of different sizes of localised region are produced with respect to the input loads. With this unique property, the computational performance of surgical simulations can be optimised and the accuracy can be preserved.

4.5 DISCUSSION

The Boussinesq method has been widely used in soil mechanics to determine displacement induced by structural footing at the surface of the soil. Even though it is a classic method, yet it is still being used nowadays due to its simplicity. As presented in the analysis, the outcome of the performance analysis suggests that the estimated displacement is not so accurate, yet, it is promising. There are plenty of rooms for improvements since many recent methods are available in the literature. In this study, the Boussinesq method was used because it is the foundation of the recent approaches. Hence, it is suitable for this initial study.

For a given small displacement value, the localised region was generated by considering the material properties and input load. Since soft tissues have different material properties, the generated localised region will accommodate the differences as well as the effect of the input load. The dependency of the proposed localised region on the input load will eliminates problems faced by a static localisation leading to optimisation of the computational performance.

There are some limitations of the method. First limitation is that the localised region was generated by assuming soft tissues as linear and isotropic material. The assumption is only valid for small deformation of soft tissues. During a large deformation, the generated localised region might be different from the real ones. Nevertheless, the proposed localised region is still applicable to reduce the computational performance. Second limitation is to define the small displacement value. Even though the user can control the value for the intended computational performance, an appropriate value needs to be selected to maintain the accuracy. Thus, the best option is to find it through experiment or computational analysis using commercial software such as ABAQUS where the setting of $\boldsymbol{u_{min}}$ can be back calculated from the corresponding FEM result. Furthermore, the study focuses only on the normal loading while interaction between soft tissues and surgical tools can happen in different directions.

4.6 CHAPTER SUMMARY

This chapter had proposed a new approach to generate localised regions to improve the computational performance of soft tissue modelling. The implementation of the localised region helps to reduce the number of nodes involved in the computational calculations. The proposed localised region is determined based on the linear elastic theory that considers the material properties and the input load. The outcomes of the analyses proved the relation of the proposed localised region to the material properties and input load. The study also has validated the accuracy of the localised region by comparing it with the FEM results obtained from the commercial ABAQUS software. The implementation of the localised region in conical spring model has shown improvement in the computational performance, and helps in optimisation of the simulation. However, the value of the smallest displacement needs to be carefully selected as it could affect the accuracy of the simulation model.

5 LOCALISED REGION USING ESTIMATION OF DISPLACEMENT FOR ANISOTROPIC MATERIAL WITH KNOWN INPUT LOAD

According to Holzapfel, soft tissues are composed of complex fibre-reinforced composite structures. The mechanical behaviour of soft tissues relies strongly on the orientation of its constituent elements such as collagen and elastin. Soft tissues are considered as isotropic when the orientation of the constituents is uniformly distributed which resulting in equal mechanical properties in any direction. However, this is not a general case for soft tissues and it usually occurs only during a small deformation [15]. The mechanical properties of soft tissues normally have a tendency to vary in different directions which are considered as anisotropic.

The previous chapter had proposed a method to form localised region for isotropic materials. The outcome of the method shows the effectiveness of the method to optimise the computational time. This chapter extends the method for isotropic materials to anisotropic materials to study localised region in certain directions.

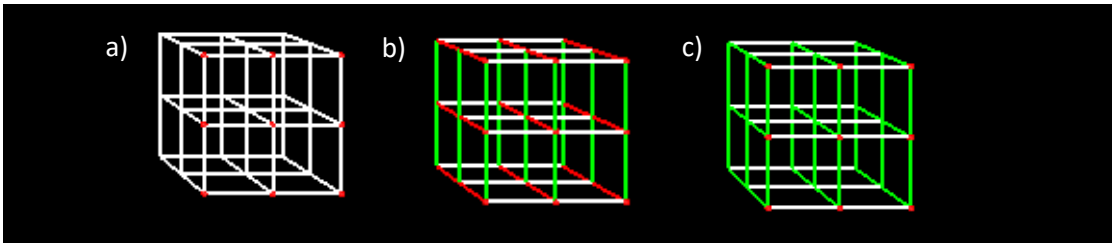

Figure 5.1. The illustration of isotropy and different types of anisotropy structure. a) Isotropic structure, b) Orthotropic structure, and c) Cross-anisotropic structure.

The modelling of fully anisotropic materials is challenging since it will involve a large number of elastic constants. Simplification can be made by considering only the three mutually orthogonal directions. As shown in Figs. 5.1(b) and 5.1(c), there are two types of anisotropy presented that are orthotropic and cross-anisotropic respectively. The orthotropic materials consist of different properties in all three directions which are illustrated by three different lattice colours. Despite the simplification, the orthotropic materials still require nine elastic constants in order to completely characterise its mechanical behaviour. However, the number of elastic constants involved can be reduced to five by assuming that the same properties are occur in one plane (e.g. in x-y plane) and different properties occur in the direction normal to this plane (e.g. z-axis). This kind of anisotropic behaviour is called cross-anisotropic. For the purpose of this chapter, it suffices to focus initially on this simplest representation of material anisotropy.

5.1 ANALYSIS ON DISPLACEMENT DISTRIBUTION

Chapter 4 had presented the finite element analysis on the displacement distribution in isotropic materials subjected to different loading magnitudes and material properties. This chapter presents the similar studies conducted to observe the displacement distribution inside the cross-anisotropic materials. A similar finite element model but with different material properties was generated using the ABAQUS software. The material properties of the cross-anisotropic body were assigned using engineering constant option in the material module. Two sets of cross-anisotropic material properties were used as given in Table 5.1. The directions of the material properties are given by the number behind each symbol, where E is elastic modulus, v is Poisson ratio, and G indicates shear modulus. The vertical direction, indicated by the number 2 was chosen as the characteristic direction for the cross-anisotropic body.

Table 5.1. Material properties of cross-anisotropic finite element model.

Material property	Set 1	Set 2
E1	42000	108000
E2	60000	60000
E3	42000	108000
v 12	0.2	0.2
v 13	0.26	0.14
v 23	0.37	0.08
G12	16667	47368
G13	17500	45000
G23	21875	27835

A normal pressure with the magnitude of 10 Pa was applied on a circular area with a radius of 0.1 m at the centre of the top surface. In Fig. 5.2, total displacement distribution for the material of Set 1 and Set 2 is presented together with the corresponding isotropic material with $E = 60$ kPa and $v = 0.2$. It can be observed that different displacement distributions were plotted. In comparison to the corresponding isotropic material, the material of Set 1 has a larger displacement distribution while the material of Set 2 has a smaller displacement distribution. The observation is due to the different material properties in horizontal direction. The material of Set 2 has a larger elastic modulus in horizontal direction and a smaller Poisson ratio which creates a larger shear modulus. As a result, the displacement distribution of material of Set 2 is smaller. On the other hand, the material of Set 1 demonstrates contradictory property which yields a larger displacement distribution.

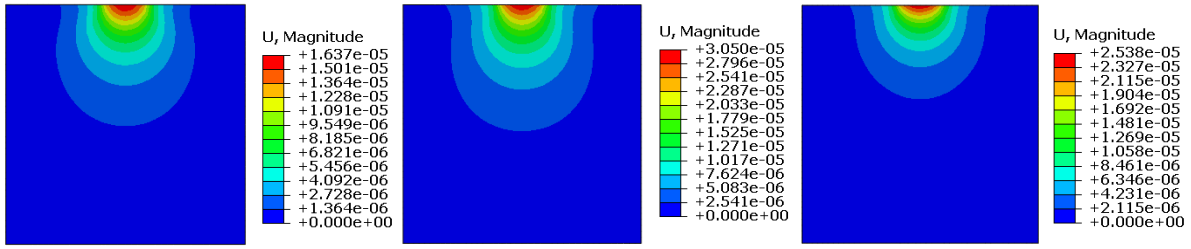

Figure 5.2.Total displacement distribution for a different set of material properties. a) Isotropic, b) Cross-anisotropic Set 1, and c) Cross-anisotropic Set 2.

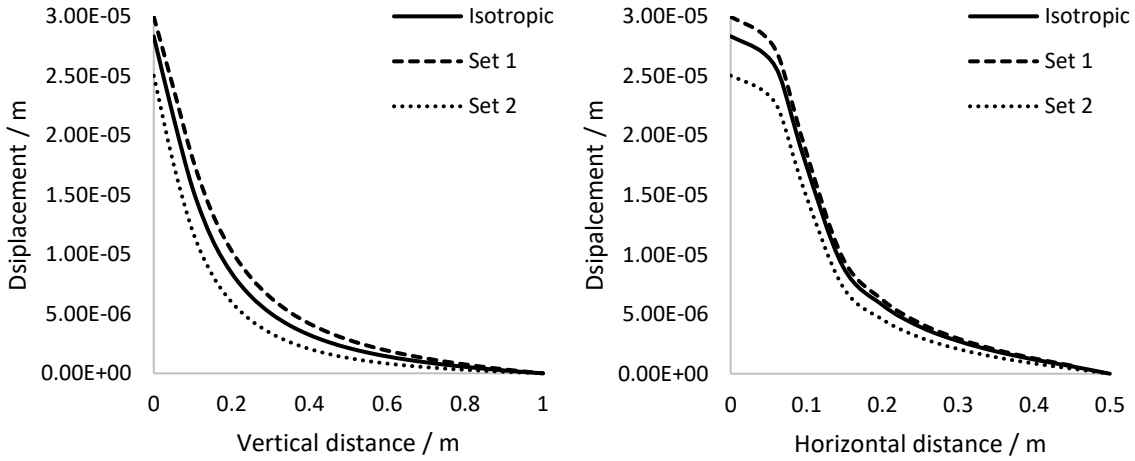

Figure 5.3. Total displacement distribution for isotropic, and material of Set 1 and Set 2 measured a) Along the vertical direction, and b) At the surface.

Further the observations were made by plotting the total displacement value along the surface and vertical direction underneath the contact point for all the materials as shown in Fig. 5.3. The result validated the initial finding. For both measured directions, the material of Set 1 has a larger displacement value compared to the isotropic material while the material of Set 2 has the smallest value.

a) Isotropic normal loading displacement components

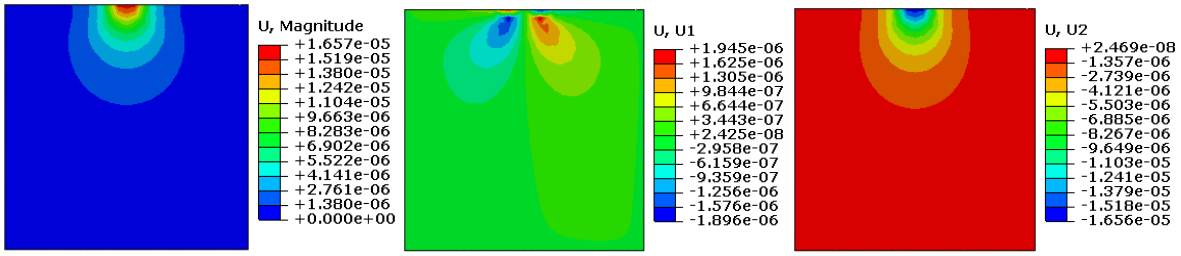

b) Cross-anisotropic (Set 1) normal loading displacement components

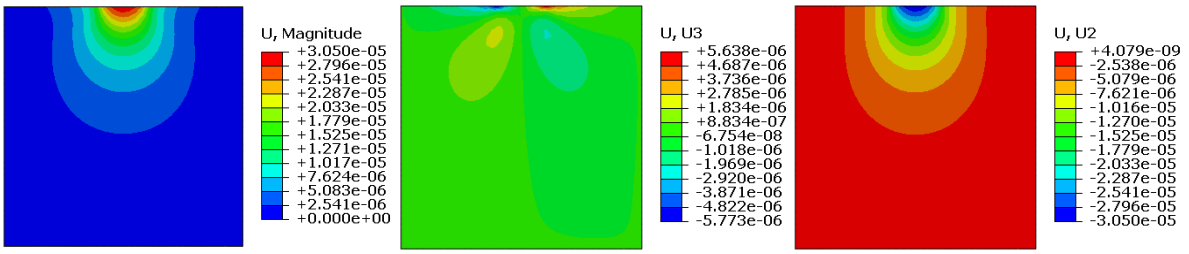

c) Cross-anisotropic Set 2 normal loading displacement components

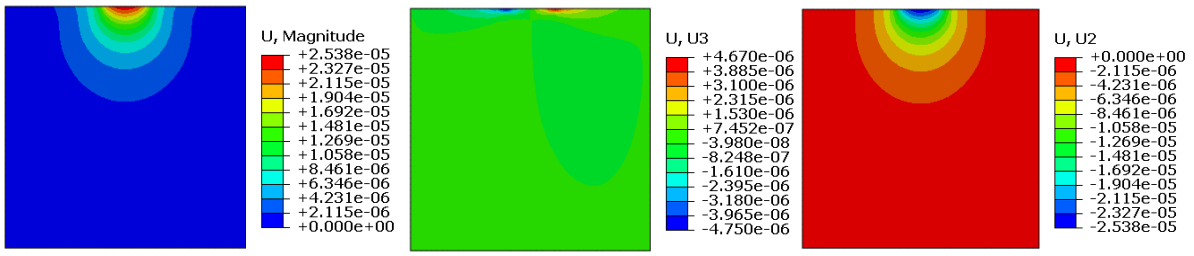

Figure 5.4.Total, horizontal and vertical displacement components of isotropic and cross-anisotropic body subject to normal loading.

By observing the displacement components for each material, it was observed that in general, the behaviour of cross-anisotropic material is similar to the isotropic material which the vertical displacement is the dominant component (see Fig. 5.4). Even though the total displacement is wider at the surface, still, as illustrated in Fig. 5.5(a), there is only a slight variation between the total displacement and vertical displacement. Meanwhile, Fig. 5.5(b) shows that total displacement measured in the vertical direction is similar to the vertical displacement component. This indicates the simplification used on isotropic materials that only considers the vertical displacement in determining the displacement distribution is also applicable for the cross-anisotropic case.

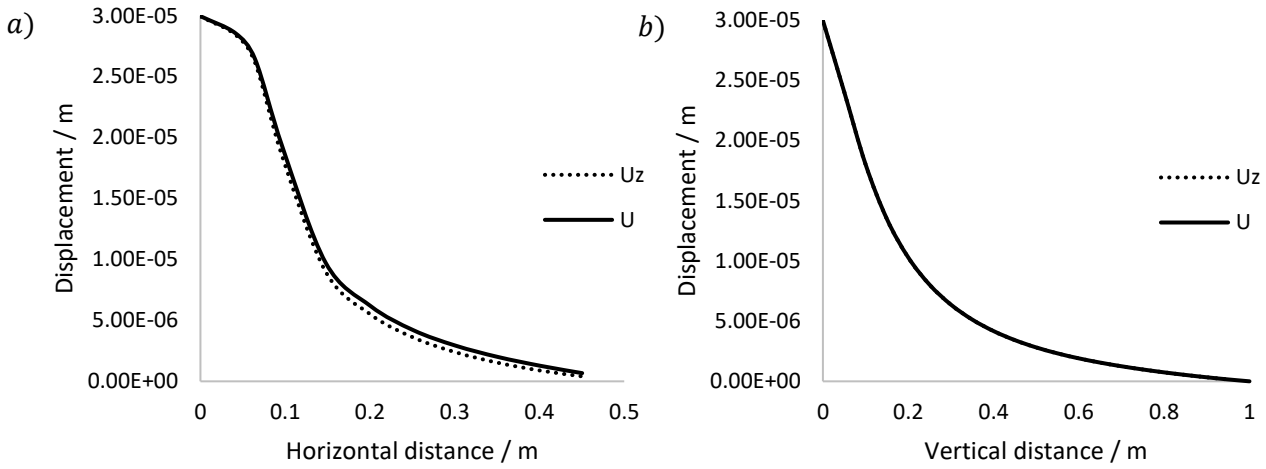

Figure 5.5. Comparison of total displacement and vertical displacement component measured a) At the surface, and b) Along vertical direction.

Several conclusions can be drawn from the analysis of displacement distribution inside the cross-anisotropic body. First, displacement distribution of cross-anisotropic materials depends on the direction of the material properties. The displacement distribution can be distorted in certain directions according to the properties. The findings confirmed the effect of the anisotropic properties to the displacement distribution, and the importance of considering anisotropic properties in generating a localised region for anisotropic materials. Second, the observation of the dominant displacement component supports the finding in Chapter 4 where vertical displacement is the dominant component.

5.2 METHOD

The most general form of Hooke's law for a linear elastic material is given as

$$\sigma_{ij} = E_{ij}\varepsilon_{ij} \tag{5.1}$$

where σ represents stress, ε denotes strain and E indicates the elastic modulus. The subscript indicates the material directions. For isotropic materials, the relation is similar for all directions due to the use of the same elastic modulus. For cross-anisotropic materials, allowing k as the characteristic direction, the relationship of the elastic modulus is given as $E_{ii} = E_{jj} \neq E_{kk}$.

A homogeneous elastic material exhibiting cross-anisotropy is defined by five elastic constants which are the elastic modulus in vertical direction E_z, the elastic modulus in horizontal direction E_x, the effect of horizontal strain on horizontal strain v_1, the effect of horizontal strain on vertical strain v_2, and the effect

of vertical strain on horizontal strain v_3. By allowing the elastic modulus in vertical direction E_z to be equal to E, the elastic modulus in the horizontal direction can be described as $E_x = nE$, where n is the anisotropic intensity. Isotropy is a special case of the anisotropy, where n is equal to 1 and all the Poisson ratios have the same value.

The plane strain-stress for the cross-anisotropic materials can be expressed as

$$\varepsilon_x = \frac{1}{nE}\sigma_x - \frac{1}{nE}v_1\sigma_y - \frac{1}{E}v_3\sigma_z \tag{5.5}$$

$$\varepsilon_y = \frac{1}{nE}\sigma_y - \frac{1}{nE}v_1\sigma_x - \frac{1}{E}v_3\sigma_z \tag{5.6}$$

$$\varepsilon_z = \frac{1}{E}\sigma_z - \frac{1}{E}v_2\sigma_x - \frac{1}{E}v_2\sigma_y \tag{5.7}$$

$$\varepsilon_{zx} = \frac{1}{G_1}(\sigma_{zx}) \tag{5.8}$$

$$\varepsilon_{zy} = \frac{1}{G_2}(\sigma_{zy}) \tag{5.9}$$

$$\varepsilon_{xy} = \frac{1}{G_3}(\sigma_{xy}) \tag{5.10}$$

where ε_{ij} and σ_{ij} represent the strain and stress in respective directions. Transposing Eq. (5.5) and Eq. (5.6) to Eq. (5.7), the stress components can be described in terms of the strain components as

$$\sigma_x = \frac{nE}{\emptyset}(1 - v_2v_3)\varepsilon_x + \frac{nE}{\emptyset}(v_1 + v_2v_3)\varepsilon_y + \frac{nE}{\emptyset}(1 + v_1)v_3\varepsilon_z \tag{5.11}$$

$$\sigma_y = \frac{nE}{\emptyset}(v_1 + v_2v_3)\varepsilon_x + \frac{nE}{\emptyset}(1 - v_2v_3)\varepsilon_y + \frac{nE}{\emptyset}(1 + v_1)v_3\varepsilon_z \tag{5.12}$$

$$\sigma_z = \frac{E}{\emptyset}(1 + v_1)v_2\varepsilon_x + \frac{E}{\emptyset}(1 + v_1)v_2\varepsilon_y + \frac{E}{\emptyset}(1 - {v_1}^2)\varepsilon_z \tag{5.13}$$

where

$$\emptyset = (1 + v_1)(1 - v_1 - 2v_2v_3) \tag{5.14}$$

Hooke's law for the cross-anisotropic material in matrix form is given as

$$\begin{bmatrix}\sigma_1\\ \sigma_2\\ \sigma_3\\ \sigma_4\\ \sigma_5\\ \sigma_6\end{bmatrix} = \begin{bmatrix} C_{11} & C_{12} & C_{13} & 0 & 0 & 0 \\ & C_{11} & C_{13} & 0 & 0 & 0 \\ & & C_{33} & 0 & 0 & 0 \\ & & & C_{44} & 0 & 0 \\ & & & & C_{44} & 0 \\ & & & & & C_{11}-C_{12} \end{bmatrix} \begin{bmatrix}\varepsilon_1\\ \varepsilon_2\\ \varepsilon_3\\ \varepsilon_4\\ \varepsilon_5\\ \varepsilon_6\end{bmatrix} \tag{5.15}$$

By comparing Eqs. (5.11) to (5.13) with the Hooke's law given in Eq. (5.15), the stiffness constants can be expressed in terms of the elastic constants as

$$C_{11} = \frac{nE}{\emptyset}(1 - v_2 v_3) \tag{5.16}$$

$$C_{12} = \frac{nE}{\emptyset}(v_1 + v_2 v_3) \tag{5.17}$$

$$C_{13} = \frac{nE}{\emptyset}(1 + v_1)v_3 = \frac{E}{\emptyset}(1 + v_1)v_2 \tag{5.18}$$

$$C_{33} = \frac{E}{\emptyset}(1 - {v_1}^2) \tag{5.19}$$

which then gives

$$C_{11} - C_{12} = \frac{nE}{1 + v_1} \tag{5.20}$$

Through the comparison, the following relationship is also obtained

$$n = \frac{v_2}{v_3} \tag{5.21}$$

The other stiffness constant can be found by looking at the shear stress. Referring to Appendix 2, the final stiffness constant is given as

$$C_{44} = \frac{E v_2}{(v_2 + v_3 + 2v_2 v_3)} \tag{5.22}$$

Restrictions are placed on the stiffness constants by the fact that the strain energy function must be positive in which the stiffness constant must obey the following conditions

$$C_{11} > {C_{12}}^2 \tag{5.23}$$

$$C_{33}(C_{11} + C_{12}) > 2{C_{13}}^2 \quad (5.24)$$

$$C_{33}C_{11} > {C_{13}}^2 \quad (5.25)$$

By substituting the stiffness constants with the elastic constants, the conditions can be rewritten as

$$1 > {v_1}^2 + 2v_2v_3 + 2v_1v_2v_3 \quad (5.26)$$

$$1 > v_1 + 2v_2v_3 \quad (5.27)$$

Another constraint is in the form of dilatation. Dilatation is also known as the volumetric strain. According to Boresi [111], the dilatation in the first-order terms of the principal strains is given as

$$e = \varepsilon_x + \varepsilon_y + \varepsilon_z \quad (5.28)$$

For a purely elastic material, the dilatation can be assumed to have the same sign as the principle stress [112]. By using the dilatation, the stress-strain relationship for the principle stresses can be rewritten as

$$\sigma_x = \frac{nE}{\emptyset}(1 - v_2v_3)e - \frac{nE}{\emptyset}(1 - v_3 - v_1v_3 - v_2v_3)\varepsilon_z - \frac{nE}{(1 + v_1)v_3}\varepsilon_y \quad (5.29)$$

$$\sigma_y = \frac{nE}{\emptyset}(1 - v_2v_3)e - \frac{nE}{\emptyset}(1 - v_3 - v_1v_3 - v_2v_3)\varepsilon_z - \frac{nE}{(1 + v_1)v_3}\varepsilon_x \quad (5.30)$$

$$\sigma_z = \frac{E}{\emptyset}(1 + v_1)v_2e + \frac{E}{\emptyset}(1 - v_2 - v_1v_2 - {v_1}^2)\varepsilon_z \quad (5.31)$$

Regarding the shear stresses, substituting the shear modulus with the elastic constants (Refer Appendix 3), the new shear stress equations are given in the form of

$$\sigma_{zx} = \frac{Ev_2}{(v_2 + v_3 + 2v_2v_3)}(\varepsilon_{zx}) \quad (5.32)$$

$$\sigma_{zy} = \frac{Ev_2}{(v_2 + v_3 + 2v_2v_3)}(\varepsilon_{zy}) \quad (5.33)$$

$$\sigma_{xy} = \frac{nE}{(1 + v_1)}(\varepsilon_{xy}) \quad (5.34)$$

Michell [113] provided a stress-strain relationship for the cross-anisotropy as in the following expressions

$$P = A\theta + (F - A)g - 2Nf \quad (5.35)$$

$$Q = A\theta + (F - A)g - 2Ne \quad (5.36)$$

$$R = F\theta + (C - F)g \tag{5.37}$$

$$S = La \tag{5.38}$$

$$T = Lb \tag{5.39}$$

$$U = Nc \tag{5.40}$$

Barden [112] derived the parameters in the stress-strain relationship given by Mitchell by comparing the relationship with the stress-strain terms given in Eqs. (5.29) to (5.34). Through the comparison, the parameters are derived in terms of elastic constants as

$$A = \frac{nE}{\emptyset}(1 - v_2 v_3) \tag{5.41}$$

$$C = \frac{E}{\emptyset}(1 - {v_1}^2) \tag{5.42}$$

$$F = \frac{E}{\emptyset}(1 + {v_1}^2)v_2 \tag{5.43}$$

$$L = \frac{Ev_2}{(v_2 + v_3 + 2v_2 v_3)} \tag{5.44}$$

$$N = \frac{nE}{(1 + v_1)} \tag{5.45}$$

where $\emptyset$ is given in Eq. (5.14).

According to Barden, the vertical displacement at the surface of a material can be calculated using

$$u_{z\ surface\ anisotropic} = \frac{P}{2\pi r} \cdot \sqrt{\frac{A}{L}} \cdot \frac{\left[\left(\sqrt{AC} + L\right)^2 - (F + L)^2\right]^{1/2}}{AC - F^2} \tag{5.46}$$

where parameters A, C, F, and L are defined in Eqs. (5.41) to (5.45).

Eq. (5.46) can be further simplified as

$$u_{z\ surface\ anisotropic} = \frac{P}{r} \cdot \frac{J}{E} \tag{5.47}$$

where J is a dimensionless factor given by

$$J = \frac{E}{2\pi} \cdot \sqrt{\frac{A}{L}} \cdot \frac{\left[\left(\sqrt{AC} + L\right)^2 - (F + L)^2\right]^{1/2}}{AC - F^2} \tag{5.48}$$

Correspondingly, the isotropic condition presents a special case for the derivation. By using isotropic parameters, the dimensionless factor J is reduced to

$$J = \frac{1 - {v_{iso}}^2}{\pi} \tag{5.49}$$

where v_{iso} indicates the Poisson ratio of the isotropic materials.

By using Eq. (5.49) in Eq. (5.47), the vertical displacement at the surface of isotropic materials is given by

$$u_{z\ surface\ isotropic} = \frac{P\ (1 - {v_{iso}}^2)}{\pi E r} \tag{5.50}$$

which is similar to the Boussinesq solution.

Therefore, the cross-anisotropic solution in terms of vertical displacement along the surface can be obtained from the corresponding isotropic solution by

$$u_{z\ surface\ cross-anisotropic} = \vartheta\ u_{z\ surface\ isotropic} \tag{5.51}$$

where ϑ is an anisotropic factor determined from

$$\vartheta = \frac{J\pi}{1 - {v_{iso}}^2} \tag{5.52}$$

5.3 LOCALISED REGION

The construction of the localised region is similar to the one presented in Chapter 4. The localised region is generated based on the three parameters illustrated in Fig. 4.7. As described in section 5.2, the vertical displacement value calculated at the surface of an isotropic material can be used to determine the same value for the corresponding cross-anisotropic material by using the anisotropic factor described in Eq. (5.52). Barden has been reported to use the anisotropic factor to determine vertical displacement value at the surface of several cross-anisotropic materials [112]. For simplification, it was assumed that the

anisotropic factor can also be used to determine the vertical displacement along the vertical direction underneath the contact point.

By adding the anisotropic factor into the isotropic solutions, the parameters of localised region for cross-anisotropic materials can be determined from the following equations.

$$l_x = \frac{\vartheta\ P_N}{4G\pi u_{\ min}}[2(1-v)] \tag{5.53}$$

$$l_y = \frac{\vartheta\ P_N}{4G\pi u_{\ min}}[2(1-v)] \tag{5.54}$$

$$l_z = \frac{\vartheta\ P_N}{4G\pi u_{min}}[1+2(1-v)] \tag{5.55}$$

It can be seen that in comparison to the isotropic solutions, there is only an addition of a simple multiplication step. It indicates that there will be not much difference in terms of the computational performance for both isotropic and cross-anisotropic method. The process of generating the localised region is given in Fig. 5.6.

Step 1	Pre-computation
	i. Set the material properties for the model
	ii. Determine the value of J
	iii. Set the intended value of $\boldsymbol{u_{min}}$
Step 2	Computation
	iv. Determine the magnitude of the applied load
	v. Solving Eqs. (5.53) to (5.55) for distance where $\boldsymbol{u_{min}}$ occurs
	vi. Generate the localised region using the half-space concept

Figure 5.6. The process of generating localised region for cross-anisotropic materials.

5.4 ANALYSIS

5.4.1 Behaviour analysis

Several analyses were conducted to observe the behaviour of the localised region for cross-anisotropic materials. The first analysis is to see the effect of the anisotropic intensity and anisotropic factor to the localised region. As introduced previously, anisotropic factor is a value that described the difference between the distance where $\boldsymbol{u_{min}}$ occurs in isotropic and cross-anisotropic materials. On the other hand, anisotropic intensity is a value that described the difference between the elastic modulus in vertical and horizontal directions. In this analysis, parameters of localised region for two sets of cross-anisotropic

materials were determined and compared. The small displacement value $\boldsymbol{u_{min}}$, was set as 0.0005 m for all directions, and the model was subjected to 10 N of normal load. By using the material properties presented in Table 5.1, the anisotropic intensity for Set 1 and Set 2 was calculated as 0.7 and 1.8 respectively. Moreover, for the material of Set 1, the calculated anisotropic factor was 1.22, while for the material of Set 2, the anisotropic factor was 0.92. It is noteworthy that for isotropic materials, the anisotropic intensity and the anisotropic factor both are equal to 1.0.

Table 5.2. Definition of parameters for the localised region in Configuration 1.

Parameters	Material	Anisotropic intensity, n	Anisotropic factor, ϑ	Distance / m
l_x				0.19
l_y	Set 1	0.7	1.22	0.19
l_z				0.30
l_x				0.05
l_y	Set 2	1.8	0.92	0.05
l_z				0.09

As presented in Table 5.2, the localised region for the material of Set 1 is larger than the material of Set 2. For the anisotropic intensity of $n < 1$, the resulting anisotropic factor is bigger than one, while an opposite reaction is shown for material with anisotropic intensity of $n > 1$. Based on Eqs. (5.53) to (5.55), it can be observed that the anisotropic factor is directly proportional to the parameters. Hence, in comparison to the isotropic solution, materials with anisotropic factor of $\vartheta > 1$ will generate a larger localised region. By plotting the relationships of anisotropic intensity-anisotropic factor (see Fig. 5.7) and anisotropic factor-parameters (see Fig. 5.8) at several values, it can be seen that the relations confirm the findings.

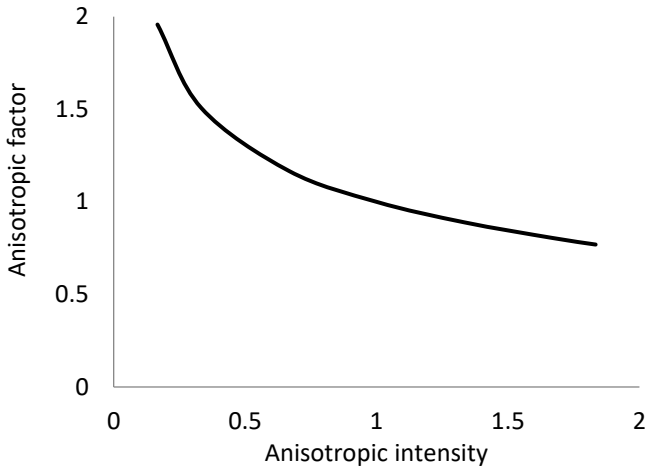

Figure 5.7. The relationship between the anisotropic dimensionless factor and anisotropic intensity.

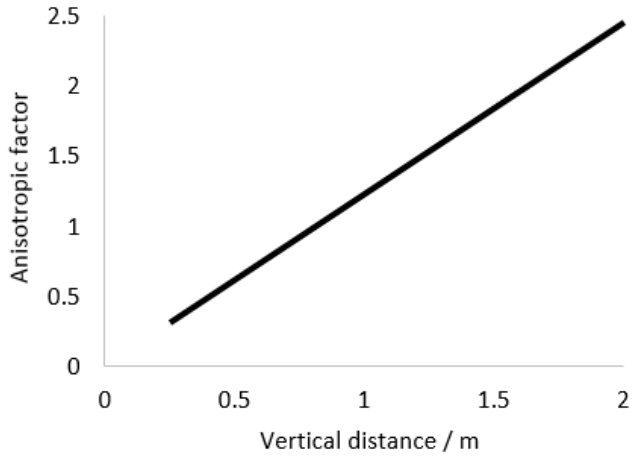

Figure 5.8.Relationship of the dimensionless factor and the distance where u_{min} occurs for the parameter l_z.

The outcomes show that the localised region for cross-anisotropic material has the same behaviour with the FEM model when the same cross-anisotropic properties were used. In comparison to Fig. 5.2, the proposed localised region also has different effects under different material properties. Moreover, the proposed localised region agrees with the result in Fig. 5.3 where a larger localised region was generated for the material of Set 1. The reason is that the material of Set 1 is less stiff, hence, leading to a larger displacement.

5.4.2 Performance analysis

To validate the localised region for cross-anisotropic materials, the study had compared the distance where the small displacement $\boldsymbol{u}_{\boldsymbol{min}}$ occurs calculated using the analytical method with the static FEM result. The static FEM result was obtained from the ABAQUS software. The cross-anisotropic properties

of the FEM model were assigned using the engineering constant module in the ABAQUS material option. A normal load was applied on the FEM model and the displacement distributions at the surface and along vertical axis underneath the contact point were recorded. Two cases were developed with different elastic modulus values in horizontal and vertical directions for each case. The Poisson ratio and the normal load were kept constant at 0.4 and 50 N respectively.

Due to the cross-anisotropic properties, different $\boldsymbol{u}_{\boldsymbol{min}}$ values were used for horizontal and vertical directions to optimise the localisation. The $\boldsymbol{u}_{\boldsymbol{min}}$ values were taken from the FEM simulation and the corresponding analytical distances were calculated. The variation between the FEM and analytical result is presented as the percentage of relative error. Details of the parameters used and the outcomes of the comparison are given in Table 5.3. The result show that the percentage of relative error is less than 20% in both cases which indicates the performance of the proposed model.

Table 5.3. The parameters used and the outcomes of the comparison between the proposed method and FEM.

Case	Ex (kPa)	Ey (kPa)	Factor	Parameter	u_{min}	Distance (m)		Error (%)
						Analytical	FEM	
Case 1	30	40	1.18	l_x and l_y	0.001679	0.234	0.2	17.0
				l_z	0.001781	0.344	0.3	14.7
Case 2	40	30	0.91	l_x and l_y	0.002322	0.174	0.2	13.0
				l_z	0.002372	0.344	0.3	14.7

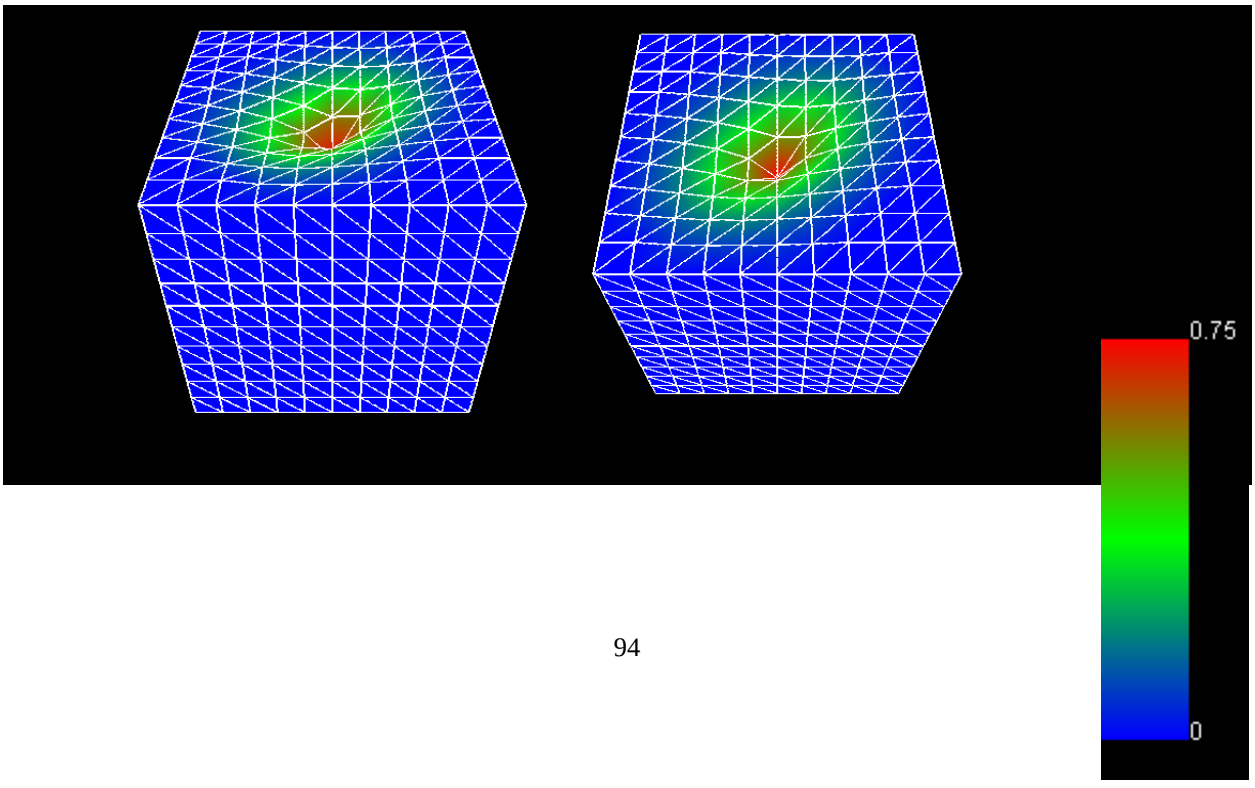

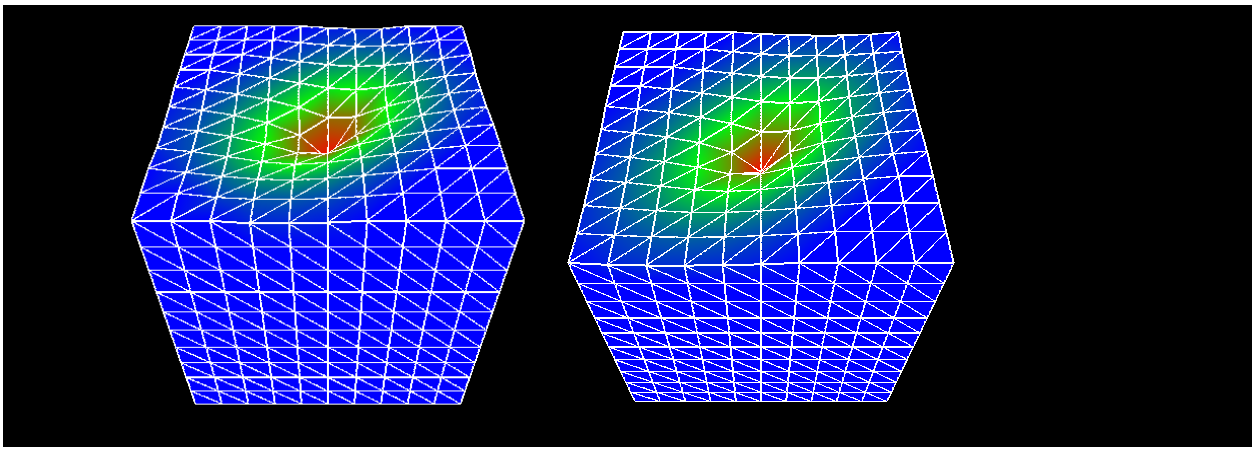

Figure 5.9. The deformation behaviour of an isotropic conical spring model with localised region a) Isotropic localised region and b) Cross-anisotropic localised region with anisotropic factor equal to 1.5. The colour contour explains the magnitude of displacement occurs.

To further study the performance of the proposed method, the method was implemented into the conical spring model described in Chapter 3. A simple cubical structure of the conical spring model consisting of 1331 nodes was generated. The isotropic material property was used since the study is only interested in observing the behaviour of the localised region, and it is difficult to control the anisotropic of conical spring model to match the FEM model. A normal load was applied to a node on the surface of the conical spring model, and the anisotropic factor was set at 1.5. As presented in Fig. 5.9, as expected, the localised region for the cross-anisotropic case was wider than those in the isotropic case since the anisotropic factor used was larger than one. This had generated a larger localised region. It should be noted that the conical spring model used here was develop based on the isotropic properties. In the real case, where the cross-anisotropic properties are implemented in the model, deformation behaviour of the cross-anisotropic models might be different.

5.5 DISCUSSION

The determination of displacement distribution in an elastic semi-infinite body with anisotropic properties involves a complex process. Past studies have proposed various methods, for methods that have higher accuracy, the solution is normally in an open form solution which is not suitable to determine the localised region. Meanwhile, there are solutions available in a closed form. Although the closed form solutions offer a simpler process, however, the process will involve several roots leading to a complex computation. This type of solution is not suitable for the localised region which aims to reduce the computational time. In

this study, a less complicated method to consider anisotropic properties was used which is using an anisotropic factor as reported by Barden.

Despite its limitations, it provides a simpler solution and with less than 20% of relative error, it still has a good level of accuracy, and the most importantly, it is suitable for real-time application. Moreover, similar to the Boussinesq method, the method proposed by Barden is also a classical approach. This study presents an initial step for the application and further improvements can be made by using recent approaches.

5.6 CHAPTER SUMMARY

The outcome of the FEM analysis signals the significance of anisotropic properties to the displacement distribution inside the subjected anisotropic materials. Since soft tissues also exhibit anisotropic properties, the localisation must also consider the properties. In this chapter, the application of the proposed localised region for isotropic materials was extended to anisotropic materials. In particular, localised regions for the cross-anisotropic materials was generated. The anisotropic properties are demonstrated by using an anisotropic factor that was derived based on the cross-anisotropic material properties. The anisotropic factor affects the parameters of the localised region in the same pattern as observed in the FEM analysis. Meanwhile, in terms of accuracy, even though the comparison with the FEM result was not so accurate, yet, the method used here is suitable to optimise computational performance for real-time interaction.

6 LOCALISED REGION USING ESTIMATION OF STRESS WITH KNOWN INPUT DISPLACEMENT

Chapter 4 and Chapter 5 had presented the methods to develop localised regions for isotropic and anisotropic materials. In both chapters, the methods are based on displacement value which was determined from a known input load. However, the accuracy of the displacement base methods in comparison to the FEM models is not highly satisfactory. Moreover, in surgical simulations, the interaction between the user and the simulation model can happen in different input values. For example, instead of load as the input value, in a case of robotic-assisted minimally invasive surgery, the displacement of the robotic tool, which is available from the encoder, is always used as input for position control of the surgical robot.

In this chapter, some alternative approaches are considered. In this regard, instead of using displacement distribution, stress distribution was used to determine parameters of localised region. Further, the interaction between the user and model was determined from a known input displacement instead of using a known input load. On top of that, the superposition method was used to show the ability of the localised region to be determined from different contact shapes.

6.1 BEHAVIOUR ANALYSIS

When a soft object is deformed by an external force, the strain energy of the object is changed. The strain energy is distributed among masses of the object to restore the deformed object to its natural state. The strain energy is zero when the object is in its natural state. It grows larger as the object gets increasingly deformed away from its natural state. According to Lagrangian mechanics, the dynamics of the soft object under an applied force are governed by

$$\mu\ddot{\boldsymbol{U}} + \gamma\dot{\boldsymbol{U}} + \frac{\partial\varepsilon(\boldsymbol{U})}{\partial U} = \boldsymbol{F} \tag{6.1}$$

where $\boldsymbol{U}$ represents the displacement of a particle at time t, μ and γ indicate the mass and damping constants of the particle, $\boldsymbol{F}$ stands for the components of externally applied force and $\varepsilon(\boldsymbol{U})$ denotes the instantaneous strain energy stored in an elastic body as a result of a deformation caused by the external force. Letting

$$\frac{\partial \varepsilon(\boldsymbol{U})}{\partial U} = \boldsymbol{G} \tag{6.2}$$

Eq. (6.1) can be rewritten as

$$\frac{\partial}{\partial t}\left(\mu \frac{\partial \boldsymbol{U}}{\partial t}\right) + \gamma \frac{\partial \boldsymbol{U}}{\partial t} + \boldsymbol{G} = \boldsymbol{F} \tag{6.3}$$

where $\boldsymbol{G}$ denotes the stress inside the object subjected to the external force to deform the object away from its natural shape.

Eq. (6.3) shows that the soft object deformation is a process of force propagation. When an elastic body is deformed under an external force, the external force is propagated among masses of the object according to material properties, leading to the stress distribution to deform the object away from the rest state. Therefore, in order to determine the object deformation, it can be done by observing the stress distributed in the object.

FEM simulations using the ABAQUS software were conducted to analyse the stress distribution in linear isotropic material subjected to a normal load. The linear elastic material was generated with the elastic modulus of 30 kPa and the Poisson ratio of 0.4. The FEM simulations were set up under an axisymmetric condition with the normal pressure of 100 Pa was applied on a circular area with radius of 0.1 m at the axis of symmetry. The illustration of the ABAQUS set up and the model under deformation are given in Fig. 6.1.

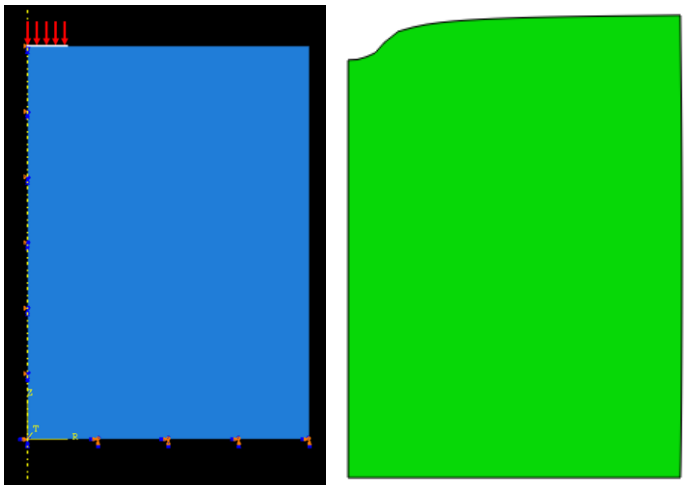

Figure 6.1. Image of the ABAQUS set up and the corresponding deformation of the FEM model.

Fig. 6.2 shows the distribution of the Von Mises stress in the FEM model. The Von Mises stress is a stress measurement that is usually used to describe the failure of a material. It can be seen that the stress at the contact point was propagated in the material in the manner of wave propagation. The stress wave gradually became smaller and finally disappeared with the increase of the distance from the contact point. Similar to displacement, stress distribution was concentrated in a small, significantly affected region during deformation. The result is in line with Shi's study which shows that most deformation takes place only in a localised region [109].

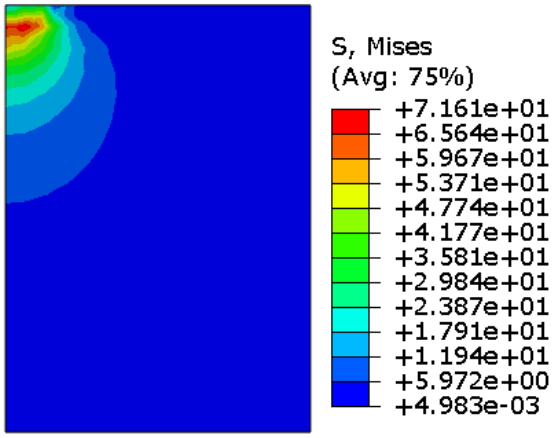

Figure 6.2. Image of the Von Mises stress distribution.

The study further examined the distribution of each stress component. Fig. 6.3 shows the distribution of the stress components. It can be seen that each stress has an individual distribution pattern. The horizontal stresses are concentrated underneath the contact area. As shown in Fig. 6.3a, the first horizontal stress component S11 propagated towards the centre of the figure at an angle of about 45 degrees. Meanwhile, the second horizontal stress component S33, lingers around the contact area. On the other hand, the vertical stress was also concentrated in the same area. However, it can be seen that the stress was propagated along the vertical axis underneath the contact area.

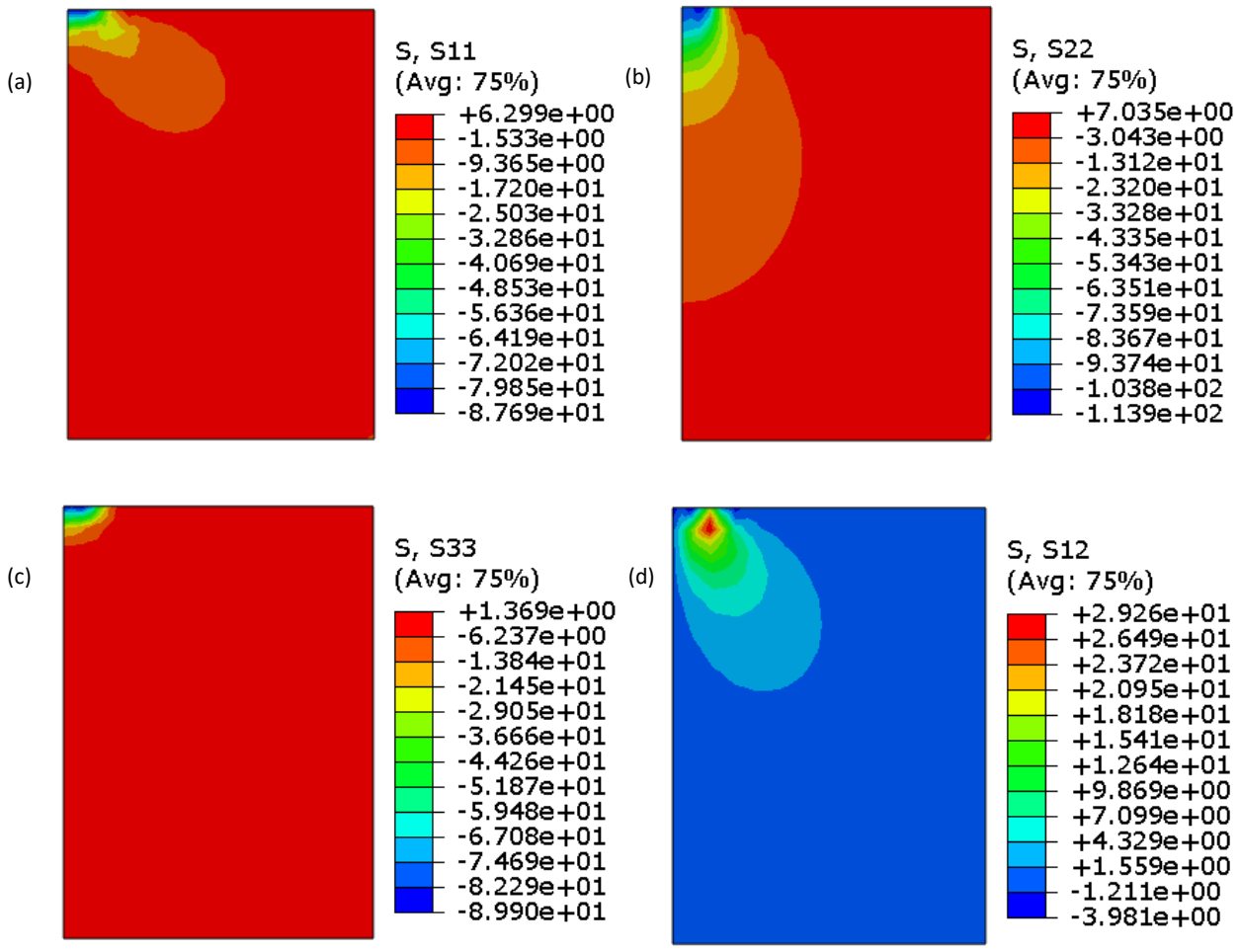

Figure 6.3. Images of stress distribution for each stress component. a) S11, horizontal stress in 11 direction, b) S22, vertical stress in 22 direction, c) S33, horizontal stress in 33 direction, and d) S12, shear stress in 12 direction.

Unlike displacement where the total displacement is clearly dominated by the vertical displacement value, the Von Mises stress shows that it is a combination of all the stress components. However, the use of the Von Mises stress to determine the localised region will consume a higher computational time due to more complex calculations involved. Alternatively, according to Olson et al. [114], the vertical stress component plays a major role in the material failure subjected to normal loading. Besides, it was also observed that the vertical stress has a larger value and distribution area than the other stress components. Therefore, to simplify the process of developing the localised region for an isotropic material subject to a normal loading, only the vertical stress component is considered.

6.1.1 Different material

To observe the effect of the material properties on the stress distribution, the loading case as illustrated in Fig. 6.1 was examined with different elastic modulus and Poisson ratio values. Fig. 6.4 shows that the vertical stress distribution in a material subjected to a normal load is affected by the elastic modulus. Larger elastic modulus provides a larger stress value which follows the Hooke's law principle. Meanwhile, as illustrated in Fig. 6.5, the Poisson ratio only has a small effect on the stress distribution. However, we can see the larger Poisson ratio produces a larger stress value especially close to the contact area. The findings suggest that the stress distribution is affected by material properties. Hence, it indicates the importance of considering material properties in developing localised region based on stress distribution.

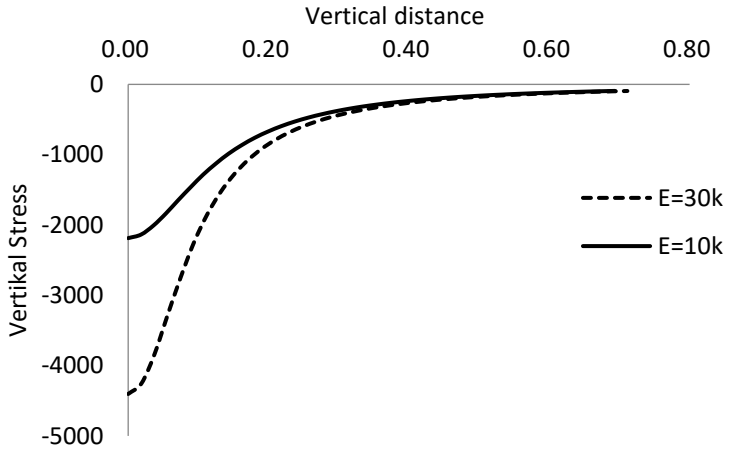

Figure 6.4. The vertical stress distributions plotted along the vertical axis underneath the contact point with different elastic modulus values.

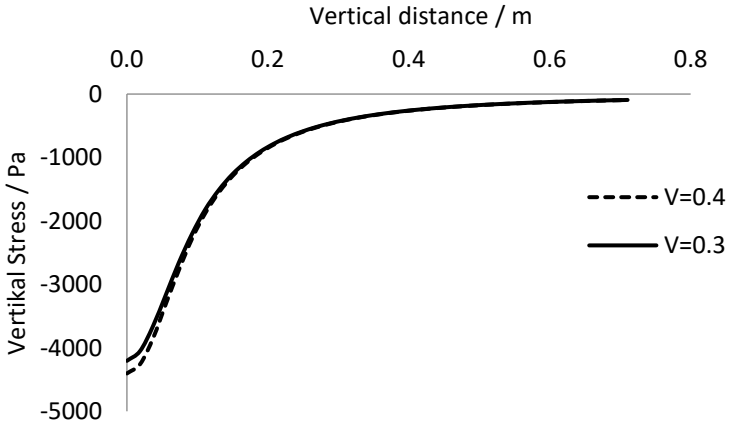

Figure 6.5. The result of the FEM simulation using indentation model for the vertical stress distribution plotted along the vertical axis underneath the contact point under different Poisson ratio.

6.1.2 Different load

Further analysis was carried out to show the effect of loading magnitude on the stress distribution. Different values of input load were applied on the FEM model. Fig. 6.6 shows that the larger load yields a larger stress value. The outcome indicates that the magnitude of the input load has a significant impact on the stress distribution.

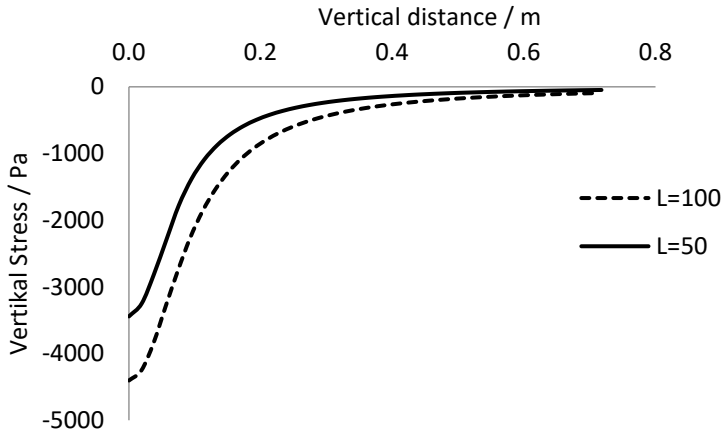

Figure 6.6. The vertical stress distribution plotted along the vertical axis underneath the contact point with different loading values.

The analyses of the factors that affect the stress distribution are crucial as they present requirements for generating appropriate localised regions. Moreover, it was observed that stress distribution is different than displacement distribution. For displacement distribution, the distribution of the vertical displacement covers the area of the other displacement components. However, for stress distribution, vertical stress distribution does not cover all the other stresses. Hence, a different approach has been proposed in the following sections to create an appropriate localisation.

6.2 METHOD

Stress distribution induced in linear material has been studied widely especially in soil mechanics. Similar to displacement distribution described in Chapter 4, Boussinesq method also can be used to determine stress distribution. Using the same derivation concept but the solutions are in terms of stresses, stresses inside linear elastic model can be estimated using cylindrical coordinate as (refer to Appendix 1)

$$\sigma_{rr} = \frac{P}{2\pi\rho^2}\left[\frac{(1-2v)\rho}{\rho + l_z} - \frac{3\, l_z\, {l_r}^2}{\rho^3}\right] \tag{6.4}$$

$$\sigma_{\theta\theta} = \frac{(1-2v)P}{2\pi\rho^2}\left[\frac{l_z}{\rho} - \frac{\rho}{\rho + l_z}\right] \tag{6.5}$$

$$\sigma_{zz} = -\frac{3P{l_z}^3}{2\pi\rho^5} \tag{6.6}$$

$$\sigma_{rz} = -\frac{3Pl_r{l_z}^2}{2\pi\rho^5} \tag{6.7}$$

where σ represents stress, and the subscripts denote direction of the stresses. Since only the vertical stress is considered, the study only focuses on Eq. (6.6).

The interaction of surgical tools with soft tissue can happen in different contact shapes. In the previous chapters, the Boussinesq method was used for point contact or point loading. Meanwhile, in this chapter, the Boussinesq method will be expanded for different loading shapes. Since the Boussinesq method is derived for point load, it can be expressed in any loading shape by using the superposition method. For example, in this study, a circular contact shape will be demonstrated.

Eq. (6.6) presents the vertical stress equation for point load problem. For a special case where only values on the vertical axis underneath the contact area is needed, the superposition method can be simplified as

$$\sigma_{zz} = -\int_{r=0}^{r=a} 2\pi r\, dr\, \frac{3Q{l_z}^3}{2\pi\rho^5} \tag{6.8}$$

where Q denotes the contact pressure applied on a circular area with radius equal to a.

The integration can be solved by replacing the r value with $l_z\, tan\, \beta$. The angle β described the relation of the vertical depth along the vertical axis and the radius of the circular area as illustrated in Fig. 6.7. The integration then appears in the form of

$$\sigma_{zz} = \int_0^{\beta} 3Q\, tan\, \beta\, cos^3\beta\, d\beta \tag{6.9}$$

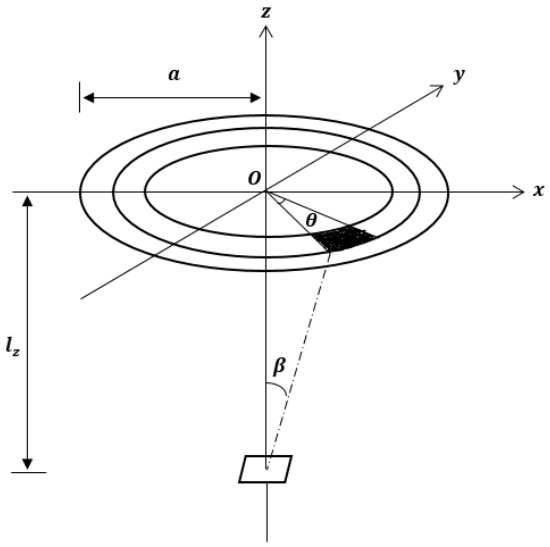

Figure 6.7.The superposition of point load for circular pressure.

Solving the integration yields

$$\sigma_{zz} = Q\left[-1 + \frac{{l_z}^3}{\left(a^2 + {l_z}^2\right)^{3/2}}\right] \tag{6.10}$$

where l_z represents the vertical depth from the contact surface for a point under the centre of the circular load, and a denotes the radius of the contact area. When l_z is equal to zero, the vertical stress is at maximum and is equal to the applied contact pressure.

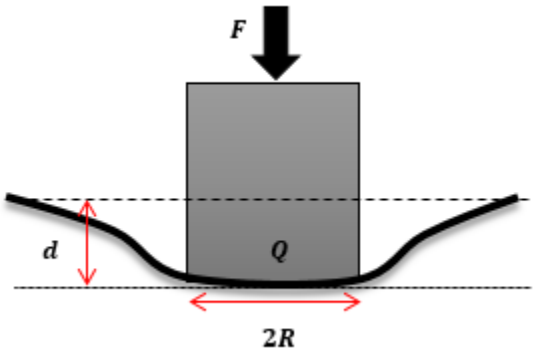

Figure 6.8. Contact interaction between the indenter and material under an external load F, where Q is the contact pressure value at some displacement d.

Eq. (6.10) can be used to determine the vertical stress distribution from a known input load. To consider simulations that work with a known input displacement, further modifications are required. As shown in Fig. 6.8, for the contact interaction between a circular flat punch and linear elastic material with elastic modulus *E* and Poison's ratio *v*, the value of contact pressure Q at a displacement *d* can be calculated using the Hertzian formula as follows [115]

$$Q = \frac{3\left(\frac{4}{3}E^{*}R^{*1/2}d^{3/2}\right)}{2\pi R^{*}d} \tag{6.11}$$

where E^{*} denotes the relative elastic modulus value given by

$$E^{*} \equiv \left(\frac{1-{v_1}^2}{E_1}+\frac{1-{v_2}^2}{E_2}\right)^{-1} \tag{6.12}$$

and R^{*} represents the relative radius value given as

$$R^{*} \equiv \left(\frac{1}{R_1}+\frac{1}{R_2}\right)^{-1} \tag{6.13}$$

The subscripts 1 and 2 given in Eq. (6.12) and Eq. (6.13) stand for the material and the flat punch respectively. In the case of interaction of surgical tools with soft tissues, surgical tools are considerably stiffer than soft tissues. Thus, the relative elastic modulus can be reduced to include only the material properties of the subjected soft tissues. Similarly, the relative radius can be reduced to consider only the radius of the circular contact area as the radius of the soft tissue surface is infinite. Hence, Eq. (6.12) and Eq. (6.13) become

$$E^{*} \equiv \left(\frac{1-{v_1}^2}{E_1}\right)^{-1} \tag{6.14}$$

$$R^{*} \equiv \left(\frac{1}{R_2}\right)^{-1} \tag{6.15}$$

Therefore, from a known displacement input value *d* that is determine from the location of the selected nodes, the input load that is in this case represented by the Hertzian contact pressure can be calculated.

Eq. (6.10) can be rewritten in terms of the Hertzian contact pressure as

$$\sigma_{zz} = \frac{3\left(\frac{4}{3}E^{*}R^{1/2}d^{3/2}\right)}{2\pi Rd}\left[-1+\frac{{l_z}^3}{\left(R^2+{l_z}^2\right)^{3/2}}\right] \tag{6.16}$$

By comparing the point load and pressure load solution, the term of the input load was replaced with the pressure value. From Eq. (6.16), it can be seen that the pressure term disappears and is replaced by the material properties and the displacement of the model. Thus, Eq. (6.16) can be solved with a known displacement value.

6.3 LOCALISED REGION

Based on the behaviour analysis, it can be observed that stress distribution has a small difference from the displacement distribution. To determine the region where stresses are significant, instead of using rectangular volume for the localised region as in the displacement based localisation, the localised region based on stress estimation is generated in the form of hemisphere volume. The localised region is described in the form of uniform radial distribution. The assumption allows the calculation of just a single parameter and uses it as the radius of the localised region.

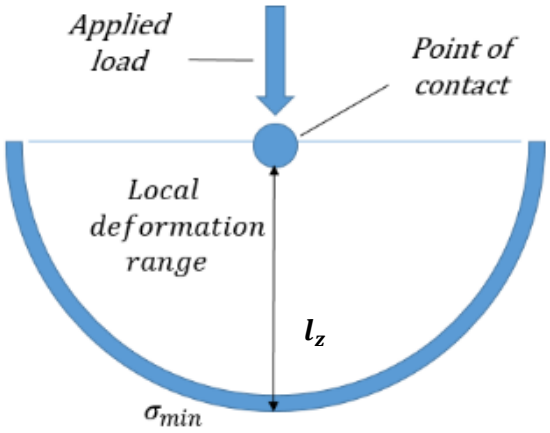

Figure 6.9. The localised region for stress based approach in the form of hemisphere volume.

In Fig. 6.9, the radius of the localised region is presented by the vertical l_z value which is identified from a limiting value. The limiting value refers to a vertical stress value inside the elastic body at a distance where deformation is insignificant which is noted as the small stress value σ_{min}. The user can control the limiting value and it can be set depending on the required computational time. The best practice is to find the value through experiment or computational analysis. The vertical distance l_z where the small

stress σ_{min} occurs can be found by solving Eq. (6.16). The calculated l_z value is then used as the radius of the localised region.

Displacement is one of the critical parameters in a dynamic surgical simulation. The value will be updated at every time step to visualise the deformation. Based on Eq. (6.16), the vertical stress is calculated in relation to the displacement, and the value will be different at different displacements. Thus, the localised region will be updated at every time step depending on the current displacement value. The sequence of the process is given in Fig. 6.10.

Step 1	Pre-computation
	i. Set the material properties for the model
	ii. Set the intended value of σ_{min}
Step 2	Computation
	iii. Determine the current displacement value
	iv. Solving Eq. (6.16) for l_z where σ_{min} occurs
	v. Generate the localised region using the half-space concept

Figure 6.10. The process of generating the stress based localised region with a known input displacement.

6.4 ANALYSIS

6.4.1 Comparison between stress and displacement estimation

Analysis was conducted to evaluate the vertical stress and vertical displacement equation for a normal point load. By using Eq. (6.7) and Eq. (4.12), the vertical stress and the vertical displacement distribution was plotted along the vertical axis underneath the contact point and was compared with the FEM result. The FEM analysis was setup with reference to the work of Helwany [116]. The result of the vertical stress is presented in Fig. 6.11 and Fig. 6.12 for stress and displacement, respectively.

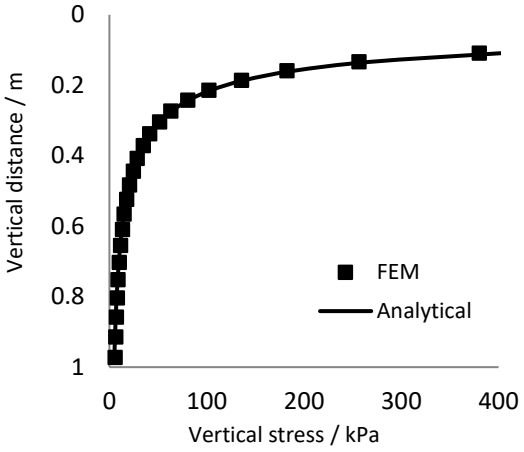

Figure 6.11. The vertical stress distribution plotted along the vertical axis underneath the contact point.

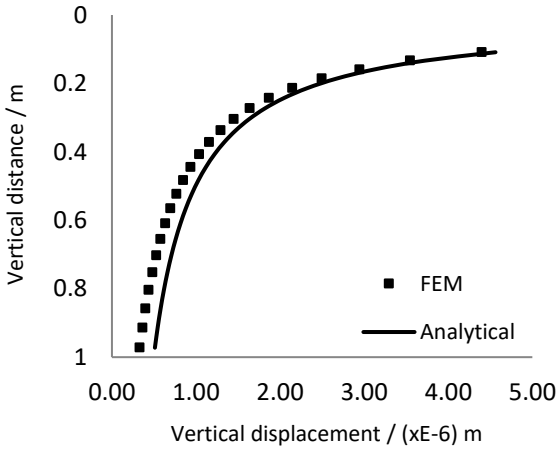

Figure 6.12. The vertical displacement distribution plotted along the vertical axis underneath the contact point.

It can be seen in Fig. 6.11 that the stress solution has an excellent accuracy with the FEM result. The variation between the results is less than 1%. In contrast to the displacement distribution presented in Fig. 6.12, the variation of the results was larger and reached more than 30% further from the contact point. The findings indicate that the stress value has a greater accuracy. However, comparing the vertical stress equation, Eq. (6.6), with the vertical displacement equation, Eq. (4.12), the main difference is there is no material properties involved in Eq. (6.6). This is a main limitation of the stress based approach.

6.4.2 Validation of Hertzian method

To validate the Hertzian method, comparisons were made with the FEM model generated using the ABAQUS software. The elastic modulus was set at 30 kPa, the Poisson ratio was set as 0.4, and the radius

of the contact area was 0.1 m. The FEM model was subjected to several contact pressures and the resulting displacements were recorded. Utilising the recorded displacements, the corresponding analytical contact pressures were calculated using the Hertzian method. As presented in Table 6.1, it can be observed that the contact pressures calculated using the Hertzian method are larger than the applied values in the FEM analysis. The relative error for all cases is consistent at around 20%. The consistency reflects the precision of the method. However, it should be noted that the displacement value used to calculate the analytical contact pressure was taken from the FEM result. Therefore, the result might be different in real practice, hence, better accuracy might be achieved.

Table 6.1. Validation of the Hertzian method with the FEM model.

Applied contact pressure / Pa	Displacement of the model / m	Calculated contact pressure using Hertzian method / Pa	Relative error / %
50	0.0003	59.6	19.1
100	0.0005	119.3	19.2
150	0.0008	178.8	19.2

6.4.3 Behaviour analysis

In the initial FEM analysis, it was discovered that stress distribution is affected by material properties and magnitude of the input load. Simple analyses were conducted to observe the effect of the same factors on the proposed method. The observations were made by plotting the stress distribution at different contact pressures, elastic modulus values and Poisson ratios. For the first analysis, different contact pressures were generated from different input displacements. During the analysis, the elastic modulus and the Poisson ratio were 30 kPa and 0.4 respectively, while the contact area comprised of a circle with a radius of 0.1 m. As illustrated in Fig. 6.13, the larger contact pressure has provided a larger stress value. The outcome is equal to the FEM model.

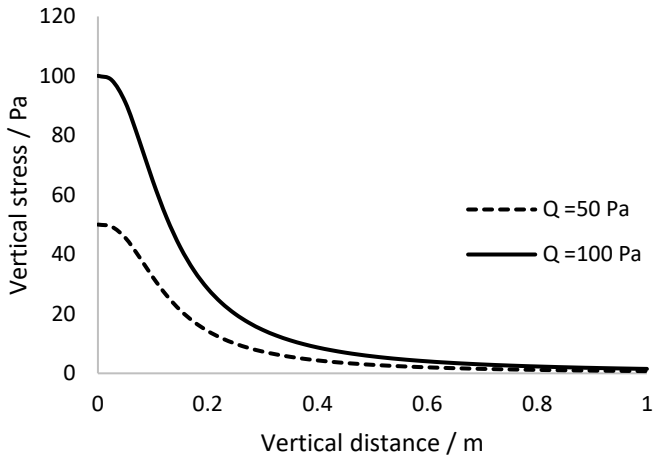

Figure 6.13. The vertical stress distribution with different contact pressures (input displacements).

Moreover, Fig. 6.14 and Fig. 6.15 present the stress distribution under different elastic modulus values and Poisson ratios respectively. For both analyses, the contact pressure was set to 100 Pa, and it was applied on a circular area with a radius of 0.1 m. It can be observed that the behaviour of the stress distributions equal the FEM model presented in Fig. 6.4 and Fig. 6.5 for different elastic modulus values and Poisson ratios correspondingly. The material with the larger elastic modulus and Poisson ratio had generated a larger stress value, and the outcomes show that the proposed method has the same behaviours with the FEM model which suggest theoretical validations. In addition, the implementation of the Hertzian method allows the calculation of the stress distribution to consider the material properties of the subject model. In this regard, the implementation has improved the original Boussinesq method.

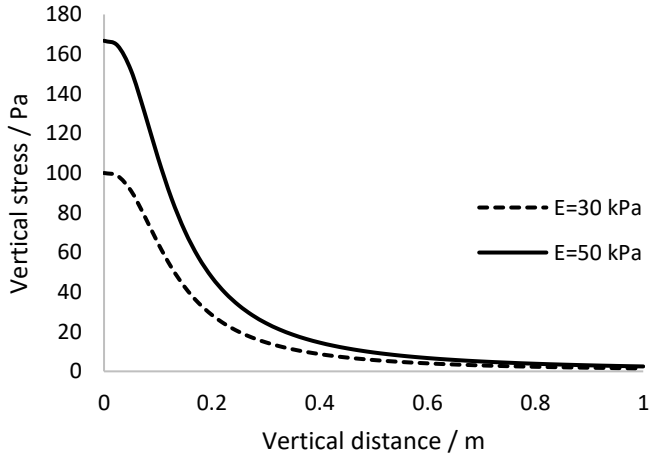

Figure 6.14. The vertical stress distribution with different elastic modulus values.

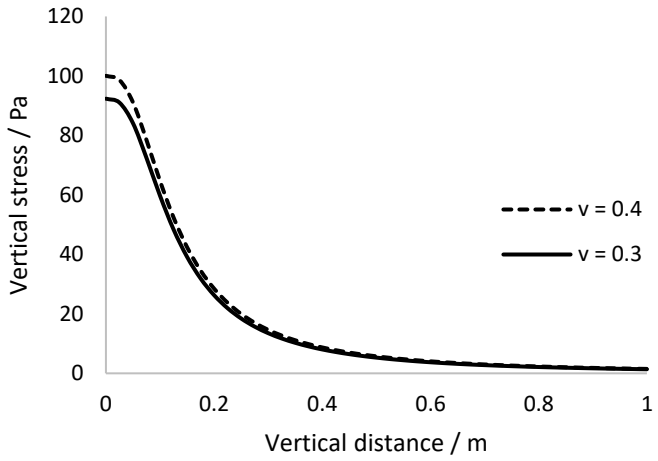

Figure 6.15. The vertical stress distribution with different Poisson ratios.

To see the behaviour of the localised region during simulation, the localised region was implemented in the conical spring model, described in Chapter 3. A simple cubical model consisting of 68921 nodes was generated. A normal pressure of 100 Pa was applied on a circular area with radius equal to 0.1 m. It was considered that the subject material has the elastic modulus and Poisson ratio of 30 kPa and 0.4 respectively. The small stress value was set at 15 Pa. As presented in Fig. 6.16, comparison was made between conical spring model without and with the localised region, and as expected, the conical spring model without the localised region has a larger deformation area due to the involvement of more nodes during deformation. The outcome is similar to the displacement based approach where implementation of the localised region reduced the number of nodes involved during the propagation of the load. Consequently, the load is propagated within the localised region, hence, a smaller deformation area can be observed.

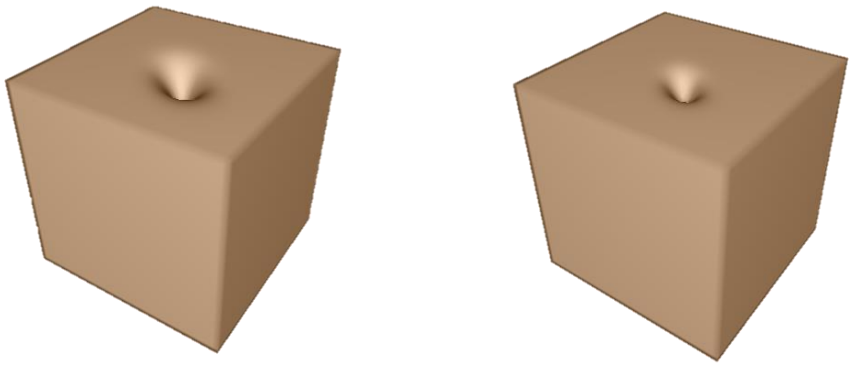

Figure 6.16. The images of the conical spring model during compression. a) Conical spring model without localised region, and b) Conical spring model with localised region.

6.4.4 Computational performance

The application of the Hertzian method and uniform circular loading presented in this chapter are also applicable to the displacement based localisation. The similar approach can be used to find a closed solution for vertical displacements along the vertical axis underneath the centre of the circular loading region. For point load, the vertical displacement equation is given by Eq. (4.12). By substituting the point load for the circular pressure, we have

$$u_z = \int_0^{\beta} \frac{2\pi r\, dr\, q\, sin\beta}{4\pi G r} [2(1-v) + cos^2\beta] \tag{6.17}$$

$$u_z = \int_0^{\beta} \frac{qz}{2G}\left[2(1-v)\frac{sin\beta}{cos^2\beta} + sin\beta\right] d\beta \tag{6.18}$$

By solving the integration, the vertical displacement is given as

$$u_z = \frac{qa}{2G}\left[\frac{\sqrt{a^2+z^2}}{a} - \frac{z}{a}\right]\left[2(1-v) + \frac{z}{\sqrt{a^2+z^2}}\right] \tag{6.19}$$

Eq. (6.19) can be rewritten with the Hertzian contact pressure as

$$u_z = \frac{3\left(\frac{4}{3}E^* R^{1/2} d^{3/2}\right)}{2\pi R d}\left(\frac{\alpha}{2G}\left[\frac{\sqrt{\alpha^2+z^2}}{\alpha} - \frac{z}{\alpha}\right]\left[2(1-v) + \frac{z}{\sqrt{\alpha^2+z^2}}\right]\right) \tag{6.20}$$

By using Eq. (6.16) and Eq. (6.20), the result of both equations was compared with the FEM analysis. The FEM analysis was setup as illustrated in Fig. 6.1, and the value of the input displacement was taken from the corresponding FEM analysis. The results of the comparison of the displacement and stress distribution are given in Fig. 6.17 and Fig. 6.18 respectively.

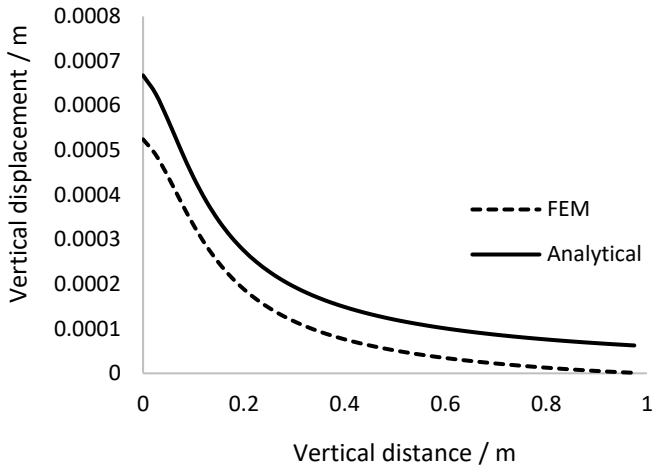

Figure 6.17. The vertical displacement distribution underneath the centre point of the circular contact area with a comparison to the FEM model.

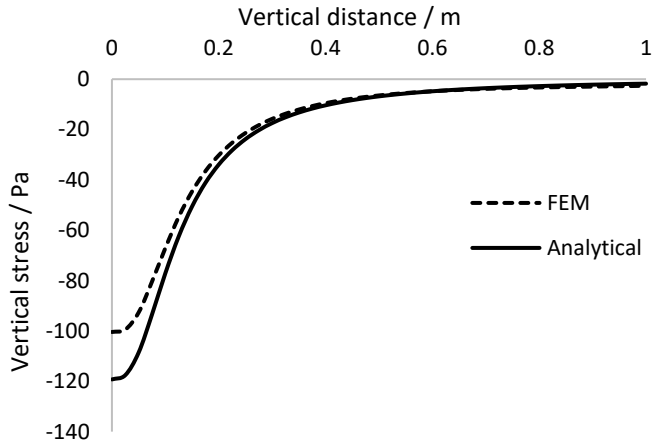

Figure 6.18. The vertical stress distribution underneath the centre point of the circular contact area with a comparison to the FEM model.

As observed in Fig. 6.17 and Fig. 6.18, the analytical method has a larger value than the FEM result in an area close to the contact area. The outcomes are associated with the calculated contact pressure using the Hertzian method. Since the calculated contact pressure is larger than the actual value, hence larger distribution is recorded. Moreover, the major difference between the displacement and stress distribution is that the stress distribution converges with FEM result further away from the contact point, but it was not observed in the displacement distribution. This shows that the stress based approach has a better accuracy than the displacement approach which is similar in the case of point load presented in Section 6.4.1.

To compare the computational performance of both approaches, a conical spring model with 68921 nodes was developed. The same structure of localised region is used that is the hemisphere volume, and the number of nodes involved during calculation is fixed at 396 nodes for both approaches. Subjected to a similar loading, Fig. 6.19 shows the deformation image of the conical spring model for both approaches, while Table 6.2 presents the computational time. There is no significant difference in terms of deformation, however, it is apparent that the stress based approach consumed a lower computational time. It might be due to the process of calculating the radius of the localised region. The formulation used in displacement based approach (see Eq. (6.20)) is more complicated than the stress based approach (see Eq. (6.16)). Hence, more iterations are required to obtain the radius.

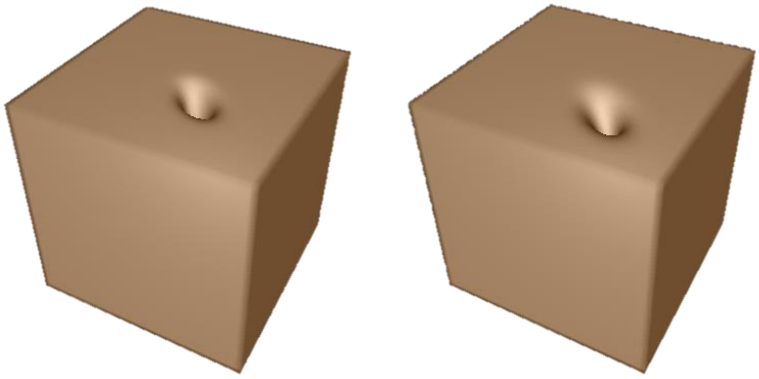

Figure 6.19. Image of conical spring model under deformation using a) Stress based, and b) Displacement based localisation approach.

Table 6.2. Computational time for stress and displacement based localisation with 396 nodes.

Localisation approach	Iteration time / milliseconds
Stress based	0.018
Displacement based	0.021

6.5 DISCUSSION

The main purpose of using the Hertzian method is to determine the applied load from a known input displacement. However, for stress based localisation, the Hertzian method also provides consideration of material properties of the subjected model. In addition, the application of the Hertzian method is not limited to the circular flat punch. It is also applicable for other contact shapes such as spherical and conical contact shapes.

In comparison to the result of the commercial ABAQUS software, stress distribution has a greater accuracy than the displacement distribution. Yet, there are some limitations to the stress based approach. According to the linear elasticity, stress is proportional to the elastic modulus, while strain is inversely proportional to elastic modulus. This means that for a stiffer material, the strain that represents displacement will be small, but the stress will be large. Therefore, the selection of the small stress value is crucial when working with different materials. This is because, if the same value is used, a larger localised region will be generated for the stiffer material instead. Consequently, over estimation can occur. Moreover, regarding the selection of the minimum value, the displacement based value has the advantage since it is directly related to deformation.

For the stress based approach, the hemisphere shape is used for the localised region instead of rectangular shape. The hemisphere localised region is generated using a single parameter while the other used three parameters. In terms of the generation process, the hemisphere approach is simpler. However, it can contain more nodes than the rectangular approach because of smaller constraints. Nevertheless, the use of the hemisphere shape is due to the behaviour of the stress distributions.

6.6 CHAPTER SUMMARY

The proposed localised region in this chapter has been established based on the same elastic theory as that of the Boussinesq method in Chapter 4. However, this chapter presented some alternative approaches in generating the localised regions. Instead of using displacement, stress property is used and instead of directly using a known input load, this chapter uses a known displacement input. Moreover, method to generate localised region from different contact shapes was also established. The analyses on the proposed method demonstrated that the stress based localisation has better accuracy in comparison to the commercial FEM software than the displacement based approach. The presented alternative approaches provide the localised region with flexibility in the sense that it can be generated in different modelling environments.

7 Conclusions and future work

This thesis presents a new method for simulating soft tissue deformations and innovative methods to improve its computational performance. The model and the improvements are applicable for a wide range of biomedical applications such as surgical training and surgical planning, as well as robotic-assisted minimally invasive surgery. The main contributions of this thesis are focused on the field of the MSM model and the development of the localised region for soft tissue deformation.

1. **Conical spring model**

A new approach in determining the stiffness of spring has been proposed to improve the traditional MSM model. Conical spring methodology is used. The stiffness of conical spring is calculated based on the location of the active coil with respect to the axis of the spring. Since the radius of the conical spring is different from top to bottom, different stiffness values can be generated. The stiffness variation can be controlled using the geometrical properties of the conical spring to suit the behaviour of the subject model. The main contributions of this topic are:

- Soft tissues become stiffer at large deformation which indicates the stiffness property is increased and not constant. The characteristic of conical spring model precisely matches the behaviour of soft tissues. It has no constant stiffness and the stiffness varies proportional to the size of deformation.
- Soft tissues show three phases of deformation response that is a combination of linear and nonlinear responses. Both types of deformation responses can be simulated by conical spring by controlling the level of the stiffness variation. The linear response can be achieved from a small stiffness variation while a large stiffness variation leads to the nonlinear response. The stiffness variation can be controlled using the geometrical properties of conical springs.
- The nonlinear response of soft tissues is more complicated than the typical polynomial functions. In this study, the nonlinearity was obtained through a combination of different stiffness values, and the degree of nonlinearity is controlled based on the level of the stiffness variation.
- To apply a modelling method into surgical simulations, the modelling method must have the flexibility to model any type of soft tissue deformations. In the conical spring model, the study has considered the three phases of soft tissue deformations which was simulated using the piecewise approach. Each phase was simulated individually using the conical spring formulations.

Since the conical spring formulations can model any type of deformation responses, the proposed method offers flexibility and accuracy in modelling.

- The ideal requirements for surgical simulation are accuracy and real-time response. FEM model offers superior accuracy allowing simulation of linear and nonlinear deformation. However, it requires additional computational equipment such as GPU and larger memory to achieve the real-time response. Alternatively, in this study, we have proposed a new MSM based model that can generate both types of deformation at a real-time response without consuming high computational cost.

2. **Localised region based on material properties**

The thesis proposes new approaches in developing localised regions. The proposed localised region is generated by finding the locations where the internal properties, displacements and stresses are insignificant during deformation. The locations are then used as parameters of the localised region. The proposed localised region is founded based on the linear elastic theory which considers the material properties. The main contributions of this topic are:

- In reality, the affected area in surgeries is small in comparison to the entire organ. The influence on the rest of the region is insignificant and can be ignored in real practice. Based on this concept, the localised region is formed. The localised region limits the computation within the affected region, and hence, the computational time of soft tissue deformations can be significantly improved.
- Material properties are one of the factors that influence soft tissue deformations. Different material properties will produce different deformations. In this thesis, the proposed localised region considers the influence. The size of the localised region varies according to the material properties of the subject model which increases the accuracy of the localisation.
- Material properties can have different values for different soft tissues. Within a soft tissue itself, the material properties can be different with regards to the material directions. The property is called anisotropy. For anisotropic materials, deformation is different from the corresponding isotropic materials. In this study, a method to generate localised regions that consider the anisotropic properties has been developed. In particular, a special case of anisotropy that is cross-anisotropic was demonstrated. An anisotropic factor was employed to the corresponding

isotropic solutions to generate localised regions for cross-anisotropic materials, and the outcomes matched the results of the FEM analysis.

3. **Localised region based on input load**

Another factor that has a significant influence on the affected area during deformation is the applied load. In the proposed localised region, applied loads with different magnitudes and contact shapes have been considered in. This study also considered two approaches to calculate the applied loads, which are from a known input load and from a known displacement input. The main contributions for this area are:

- FEM analysis shows that the applied load is proportional with soft tissue deformations. The proposed localised region is directly related to the magnitude of the applied load which indicates the number of nodes involved in calculation depends on the value of the load. Large loads will involve more nodes while small loads will contain fewer nodes. In this regard, the applications can optimise the computational performance.
- Another condition that needs to be considered during the interaction between surgical tools and soft tissues is the contact shapes. This study has presented two kinds of contact: point and circular contact. It was shown that the localised region can be formed out of these two contacts. However, the proposed localised region is not confined to these two contact conditions alone. By using the superposition approach, the solution can be expressed for different contact shapes. This ability is important particularly to simulate the interaction of robotic arm that has different tip sizes and shapes.
- In most of the surgical simulations, the magnitude of the external load is kept updated at each time step to dynamically obtained deformation. Since the proposed localised region is directly related to the external load, at each time step, the size of the localised region is changed accordingly with the current applied load. The dynamic ability of the localised region removes the probability of having over or under constraint localised region that is possessed by a static localisation.
- Deformations in elastic bodies occur due to disturbance in its equilibrium. The disturbance is usually in the form of applied load. There are two most common approaches to measure the applied load; from a known input load and from a known input displacement. In this study, we have proposed and shown that the localised region can be formed using both approaches. The

achievement is significant since it shows that the proposed method can be applied to different modelling methods and environments.

4. Future work

The MSM is an interesting alternative to the FEM, especially for real-time interactive applications. The proposed methodologies in this study show that the accuracy and the computational performance of the traditional MSM model have been improved. Nevertheless, the thesis had only presented some milestone achievements in obtaining an optimum surgical simulation. There are plenty of work to be commenced ahead, and the following are some of them.

- The main weakness of the proposed conical spring model is that there is no direct relation between material sciences and the parameters of the model. The calibration of the parameters is made using trial and error approach. Moreover, the study did not include the behaviour of the model subjects to other than uniaxial stress, such as shear and torsional stress. Further investigations and experimentations into the parameter derivation and the effect of the model under different loading are strongly recommended.
- The main weakness of the proposed localised region is that the fundamental in its development is founded on homogeneous and linear elastic materials. It will be interesting to add nonlinearity and inhomogeneity into consideration so that it can accurately represent soft tissue properties. Additionally, another exciting path is to study the generation of the localised region under different loading directions.

LIST OF PUBLICATIONS

1. **Omar, N**., Zhong, Y., Jazar, R.N., Subic, A., Smith, J. and Shirinzadeh, B., 2015. Soft tissue modelling with conical springs. *Bio-Medical Materials and Engineering*, *26*(s1), pp. S207-S214.

2. **Omar, N**., Zhong, Y., Smith, J. and Gu, C., 2016. Local deformation for soft tissue simulation. *Bioengineered*, *7*(5), pp.291-297.

REFERENCES

[1] Headquarters, W. H. O. 2006. Safe surgery saves lives.

[2] World Health Organization, 2009. WHO guidelines for safe surgery: safe surgery saves lives.

[3] Westebring–Van Der Putten, E.P., Goossens, R.H.M., Jakimowicz, J.J. and Dankelman, J., 2008. Haptics in minimally invasive surgery–a review. Minimally Invasive Therapy & Allied Technologies, 17(1), pp.3-16.

[4] Pierorazio, P.M. and Allaf, M.E., 2009, April. Minimally invasive surgical training: challenges and solutions. In Urologic Oncology: Seminars and Original Investigations, 27(2), pp. 208-213.

[5] Schreuder, H.W., Wolswijk, R., Zweemer, R.P., Schijven, M.P. and Verheijen, R.H., 2012. Training and learning robotic surgery, time for a more structured approach: a systematic review. BJOG: An International Journal of Obstetrics & Gynaecology, 119(2), pp.137-149.

[6] Hamilton, J.M., Kahol, K., Vankipuram, M., Ashby, A., Notrica, D.M. and Ferrara, J.J., 2011. Toward effective pediatric minimally invasive surgical simulation. Journal of pediatric surgery, 46(1), pp.138-144.

[7] Cant, R.P. and Cooper, S.J., 2010. Simulation-based learning in nurse education: systematic review. Journal of advanced nursing, 66(1), pp.3-15.

[8] Dunkin, B., Adrales, G.L., Apelgren, K. and Mellinger, J.D., 2007. Surgical simulation: a current review. Surgical endoscopy, 21(3), pp.357-366.

[9] Wilson, M.S., Middlebrook, A., Sutton, C., Stone, R. and McCloy, R.F., 1997. MIST VR: a virtual reality trainer for laparoscopic surgery assesses performance. Annals of the Royal College of Surgeons of England, 79(6), p.403.

[10] Al-Khlaifah, A. and Roberts, D., 2005. A survey of modeling approaches for medical simulators. International Journal on Disability and Human Development, 4(3), p.153.

[11] Misra, S., Ramesh, K.T. and Okamura, A.M., 2008. Modeling of tool-tissue interactions for computer-based surgical simulation: A literature review. Presence: Teleoperators and Virtual Environments, 17(5), pp.463-491.

[12] Chanthasopeephan, T., Desai, J.P. and Lau, A.C., 2005, July. 3D and 2D finite element analysis in soft tissue cutting for haptic display. In Proceedings of 12th International Conference on Advanced Robotics, pp. 360-367.

[13] Delingette, H., 1998. Toward realistic soft-tissue modeling in medical simulation. Proceedings of the IEEE, 86(3), pp.512-523.

[14] Gibson, S.F. and Mirtich, B., 1997. A survey of deformable modeling in computer graphics. Technical Report, Mitsubishi Electric Research Laboratories.

[15] Fung Y.C., 1993. Biomechanics: Mechanical properties of living tissues. Springer, New York.

[16] Holzapfel, G.A., 2001. Biomechanics of soft tissue. The handbook of materials behavior models, 3, pp.1049-1063.

[17] Hoffler, C.E., Moore, K.E., Kozloff, K., Zysset, P.K. and Goldstein, S.A., 2000. Age, gender, and bone lamellae elastic moduli. Journal of Orthopaedic Research, 18(3), pp.432-437.

[18] Hsu, W.M., Hughes, J.F. and Kaufman, H., 1992, July. Direct manipulation of free-form deformations. In ACM SIGGRAPH Computer Graphics, 26(2), pp.177-184.

[19] MacCracken, R. and Joy, K.I., 1996, August. Free-form deformations with lattices of arbitrary topology. In Proceedings of the 23rd annual conference on Computer graphics and interactive techniques, pp.181-188.

[20] Coquillart, S., 1990. Extended free-form deformation: a sculpturing tool for 3D geometric modelling, 24(4), pp.187-196.

[21] Terzopoulos, D. and Fleischer, K. 1988. Deformable models. The Visual Computer, 4(6), pp.306-331.

[22] Terzopoulos, D., Platt, J., Barr, A. and Fleischer, K., 1987, August. Elastically deformable models. In ACM SIGGRAPH Computer Graphics, 21(4), pp.205-214.

[23] Gibson, S., 1997. 3D chainmail: A fast algorithm for deforming volumetric objects. In Proceedings of Symposium on Interactive 3D Graphics, pp.149-154.

[24] Bathe, K.J., 1996. Finite Element Procedures. Prentice Hall, New York.

[25] Bro-Nielsen, M. and Cotin, S., 1996, August. Real-time Volumetric Deformable Models for Surgery Simulation using Finite Elements and Condensation. In Computer graphics forum, 15(3), pp.57-66.

[26] Taylor, Z.A., Cheng, M. and Ourselin, S., 2008. High-speed nonlinear finite element analysis for surgical simulation using graphics processing units. IEEE transactions on medical imaging, 27(5), pp.650-663.

[27] Brebbia, C.A., 1982. Boundary element methods in engineering. Springer, New York.

[28] Belytschko, T., Krongauz, Y., Organ, D., Fleming, M. and Krysl, P., 1996. Meshless methods: An overview and recent developments. Computer methods in applied mechanics and engineering, 139(1-4), pp.3-47.

[29] Picinbono, G., Delingette, H. and Ayache, N., 2000, October. Real-time large displacement elasticity for surgery simulation: Non-linear tensor-mass model. In International Conference on Medical Image Computing and Computer-Assisted Intervention, pp. 643-652.

[30] Liu, X.P., Xu, S., Zhang, H. and Hu, L., 2011. A new hybrid soft tissue model for visio-haptic simulation. IEEE Transactions on instrumentation and measurement, 60(11), pp.3570-3581.

[31] Basafa, E. and Farahmand, F., 2011. Real-time simulation of the nonlinear visco-elastic deformations of soft tissues. International journal of computer assisted radiology and surgery, 6(3), pp.297-307.

[32] Etheredge, C.E., 2011. A parallel mass-spring model for soft tissue simulation with haptic rendering in CUDA. In 15th Twente Student Conference on IT.

[33] Huang, P., Gu, L., Li, X., Zhang, S., Xu, J., Lin, C. and Fang, Q., 2006, July. Real-Time simulation for global deformation of soft tissue using deformable centerline and medial representation. In International Symposium on Biomedical Simulation, pp.67-74.
[34] Yang, Y., Xiao, R. and He, Z., 2011, January. Real-time deformations simulation of soft tissue by combining mass-spring model with pressure based method. In 3rd International Conference on Advanced Computer Control (ICACC), pp.506-510.
[35] Cui, T., Song, A. and Wu, J., 2009. Simulation of a mass-spring model for global deformation. Frontiers of Electrical and Electronic Engineering in China, 4(1), pp.78-82.
[36] San-Vicente, G., Aguinaga, I. and Celigueta, J.T., 2012. Cubical mass-spring model design based on a tensile deformation test and nonlinear material model. IEEE Transactions on Visualization and Computer Graphics, 18(2), pp.228-241.
[37] Chen, F., Gu, L., Huang, P., Zhang, J. and Xu, J., 2007, August. Soft tissue modeling using nonlinear mass spring and simplified medial representation. In 29th Annual International Conference of the IEEE on Engineering in Medicine and Biology Society, pp.5083-5086.
[38] Costa, I.F., 2012. A novel deformation method for fast simulation of biological tissue formed by fibers and fluid. Medical image analysis, 16(5), pp.1038-1046.
[39] Nesme, M., Payan, Y. and Faure, F., 2005, August. Efficient, physically plausible finite elements. In Eurographics, pp.2–5.
[40] Miller, K., Joldes, G., Lance, D. and Wittek, A., 2007. Total Lagrangian explicit dynamics finite element algorithm for computing soft tissue deformation. Communications in numerical methods in engineering, 23(2), pp.121-134.
[41] Zhuang, Y., 2000. Real-time simulation of physically realistic global deformations (Doctoral dissertation, University of California at Berkeley).
[42] Berkley, J., Turkiyyah, G., Berg, D., Ganter, M. and Weghorst, S., 2004. Real-time finite element modeling for surgery simulation: An application to virtual suturing. IEEE Transactions on visualization and computer graphics, 10(3), pp.314-325.
[43] Courtecuisse, H., Jung, H., Allard, J., Duriez, C., Lee, D.Y. and Cotin, S., 2010. GPU-based real-time soft tissue deformation with cutting and haptic feedback. Progress in biophysics and molecular biology, 103(2), pp.159-168.
[44] Costa, K.D., Hunter, P.J., Rogers, J.M., Guccione, J.M., Waldman, L.K. and McCulloch, A.D., 1996. A three-dimensional finite element method for large elastic deformations of ventricular myocardium: Part I - Cylindrical and spherical polar coordinates. Journal Biomechanical Engineering, 118(4), pp.452–63.
[45] Strbac, V., 2013. Nonlinear real-time finite element analysis using CUDA.
[46] Joldes, G.R., Wittek, A. and Miller, K., 2011. Real-time nonlinear finite element computations on GPU: handling of different element types. In Computational Biomechanics for Medicine, pp.73-80.
[47] Miller, K., Horton, A., Joldes, G.R. and Wittek, A., 2012. Beyond finite elements: a comprehensive, patient-specific neurosurgical simulation utilizing a meshless method. Journal of biomechanics, 45(15), pp.2698-2701.
[48] Horton, A., Wittek, A. and Miller, K., 2006, October. Towards meshless methods for surgical simulation. In Proceedings of MICCAI Workshop. Copenhagen, pp. 34-43.
[49] Cooper, L., and Maddock, S., 1997. Preventing collapse within mass-spring-damper models of deformable objects. 5th International Conference Centre Europe, Computer Graphic Visual, 2(1), pp.196–204.
[50] Teschner, M., Girod, S. and Girod, B., 2000, November. Direct Computation of Nonlinear Soft-Tissue Deformation. Vis. Model. Vis., pp. 22–24.
[51] Duysak, A., Zhang, J.J. and Ilankovan, V., 2003, June. Efficient modelling and simulation of soft tissue deformation using mass-spring systems. In International Congress Series, 1256(1), pp.337-342.
[52] Mohammadi, H., 2009. A numerical method to enhance the accuracy of mass-spring systems for modeling soft tissue deformations. Journal of applied biomechanics, 25(3), pp.271-278.
[53] Pourhosseini, M., Azimirad, V. and Kazemi, M., 2014. A new fast nonlinear modeling of soft tissue for surgical simulation. Journal of Robotic Surgery, 8(2), pp.141-148.
[54] Luo, Q. and Xiao, J., 2007. Contact and deformation modeling for interactive environments. IEEE Transactions on Robotics, 23(3), pp.416-430.
[55] Sulaiman, S., Yee, T.S. and Bade, A., 2014. Effect of time complexities and variation of mass spring model parameters on surgical simulation. Malaysian Journal of Fundamental and Applied Sciences, 9(4), pp.171–179.
[56] Shah, R. and Gupta, A., 2013. Non-linear cubic spring-mesh model for simulating biological tissues. Bio-Medical Engineering Science, 51(Supplement), pp. U-12.
[57] Garg, A., and Sreeni, K. G., 2013. Haptic Rendering of Thin and Soft Objects. Ictact Journal On Image And Video Processing, 3(3), pp.539–550.
[58] Choi K-S, Sun H, Heng P-A. Interactive deformation of soft tissues with haptic feedback for medical learning. IEEE Transactions on Information Technology in Biomedicine 2003, 7(4), pp358-363.
[59] Choi, K.S., Sun, H., Heng, P.A. and Zou, J., 2004. Deformable simulation using force propagation model with finite element optimization. Computers & Graphics, 28(4), pp.559-568.
[60] Mun, P., Zhong, Y., Shirinzadeh, B., Smith, J. and Gu, C., 2011. An improved mass-spring model for soft tissue deformation with haptic feedback. In ICMT 2011, pp. 1-6.
[61] Chang, Y.H., Chen, Y.T., Chang, C.W. and Lin, C.L., 2010. Development scheme of haptic-based system for interactive deformable simulation. Computer-Aided Design, 42(5), pp.414-424.
[62] Basafa, E., Farahmand, F. and Vossoughi, G., 2008. A non-linear mass-spring model for more realistic and efficient simulation of soft tissues surgery. Studies in health technology and informatics, 132(1), p.23-25.

[63] Nikolaev, S., 2013. Non-linear mass-spring system for large soft tissue deformations modeling. Scientific and technical journal of information technologies, mechanics and optics, 5(87), pp. 88-94.
[64] Keeve, E., Girod, S., Kikinis, R. and Girod, B., 1998. Deformable modeling of facial tissue for craniofacial surgery simulation. Computer aided surgery, 3(5), pp.228-238.
[65] García, M., Gómez, M., Ruíz, Ó. and Boulanger, P., 2005. Spring–particle model for hyperelastic cloth. In Canadian Congress of Applied Mechanics, CANCAM.
[66] Hammer, P.E., Pedro, J. and Howe, R.D., 2011, May. Anisotropic mass-spring method accurately simulates mitral valve closure from image-based models. In International Conference on Functional Imaging and Modeling of the Heart, pp. 233-240.
[67] Delingette, H., Cotin, S. and Ayache, N., 1999. A hybrid elastic model allowing real-time cutting, deformations and force-feedback for surgery training and simulation. In Computer Animation Proceedings, pp. 70-81.
[68] Picinbono, G., Delingette, H. and Ayache, N., 2003. Non-linear anisotropic elasticity for real-time surgery simulation. Graphical models, 65(5), pp.305-321.
[69] Xu, S., Liu, X.P., Zhang, H. and Hu, L., 2011. A nonlinear viscoelastic tensor-mass visual model for surgery simulation. IEEE Transactions on Instrumentation and Measurement, 60(1), pp.14-20.
[70] del-Castillo, E., Basañez, L. and Gil, E., 2013. Modeling non-linear viscoelastic behavior under large deformations. International Journal of Non-Linear Mechanics, 57, pp.154-162.
[71] Ahmadian, M.T. and Nikooyan, A.A., 2006. Modeling and prediction of soft tissue directional stiffness using in-vitro force-displacement data. Int. J. Sci. Res, 16, pp.385-389.
[72] Wang, Y. and Guo, S., 2014, August. Elasticity analysis of Mass-spring model-based virtual reality vascular simulator. In International Conference on Mechatronics and Automation (ICMA), pp. 292–297.
[73] Duan, Y., Huang, W., Chang, H., Chen, W., Zhou, J., Teo, S.K., Su, Y., Chui, C.K. and Chang, S., 2016. Volume Preserved Mass–Spring Model with Novel Constraints for Soft Tissue Deformation. IEEE journal of biomedical and health informatics, 20(1), pp.268-280.
[74] Sala, A., Turini, G., Ferrari, M., Mosca, F. and Ferrari, V., 2011, August. Integration of biomechanical parameters in tetrahedral mass-spring models for virtual surgery simulation. In Engineering in Medicine and Biology Society, EMBC, 2011 Annual International Conference of the IEEE, pp. 4550-4554.
[75] Choi, K.S., Sun, H. and Heng, P.A., 2004. An efficient and scalable deformable model for virtual reality-based medical applications. Artificial intelligence in medicine, 32(1), pp.51-69.
[76] Bourguignon, D. and Cani, M.P., 2000. Controlling anisotropy in mass-spring systems. In Computer Animation and Simulation 2000, pp. 113-123.
[77] Huang, P., Gu, L., Li, X., Zhang, S., Xu, J., Lin, C. and Fang, Q., 2006, July. Real-Time simulation for global deformation of soft tissue using deformable centerline and medial representation. In International Symposium on Biomedical Simulation, pp. 67-74.
[78] Hong, M., Jung, S., Choi, M.H. and Welch, S.W., 2006. Fast volume preservation for a mass-spring system. IEEE Computer Graphics and applications, 26(5), pp.83-91.
[79] Mesit, J., Guha, R. and Chaudhry, S., 2007. 3d soft body simulation using mass-spring system with internal pressure force and simplified implicit integration. Journal of Computers, 2(8), pp.34-43.
[80] Zerbato, D., Galvan, S. and Fiorini, P., 2007, October. Calibration of mass spring models for organ simulations. In International Conference on Intelligent Robots and Systems, IROS 2007, pp.370-375.
[81] Maciel, A., Boulic, R. and Thalmann, D., 2003. Deformable tissue parameterized by properties of real biological tissue. In Surgery Simulation and Soft Tissue Modeling, pp.74-87.
[82] Jansson, J. and Vergeest, J.S., 2002. A discrete mechanics model for deformable bodies. Computer-Aided Design, 34(12), pp.913-928.
[83] Nogami, R., Noborio, H., Ujibe, F. and Fujii, H., 2004, April. Precise deformation of rheologic object under MSD models with many voxels and calibrating parameters. In International Conference on Robotics and Automation. Proceedings. ICRA'04, 2(1), pp.1919-1926.
[84] Gelder, A.V., 1998. Approximate simulation of elastic membranes by triangulated spring meshes. Journal of graphics tools, 3(2), pp.21-41.
[85] Lloyd, B., Székely, G. and Harders, M., 2007. Identification of spring parameters for deformable object simulation. IEEE Transactions on Visualization and Computer Graphics, 13(5), pp.1081–1094.
[86] Delingette, H., 2008. Triangular springs for modeling nonlinear membranes. IEEE Transactions on Visualization and Computer Graphics, 14(2), pp.329-341.
[87] Baudet, V., Beuve, M., Jaillet, F., Shariat, B. and Zara, F., 2009. Integrating tensile parameters in hexahedral mass-spring system for simulation. Proc. 29th Int'l Conf. Computer Graphics, Visualization, and Computer Vision (WSCG '09), pp.145-152.
[88] Morris, D. and Salisbury, K., 2008. Automatic preparation, calibration, and simulation of deformable objects. Computer Methods In Biomechanics And Biomedical Engineering, 11(3), pp.263-279.
[89] Deussen, O., Kobbelt, L. and Tücke, P., 1995. Using simulated annealing to obtain good nodal approximations of deformable bodies. In Computer Animation and Simulation'95, pp. 30-43.
[90] Louchet, J., Provot, X. and Crochemore, D., 1995. Evolutionary identification of cloth animation models. In Computer Animation and Simulation'95, pp.44-54.

[91] Joukhadar, A., Garat, F. and Laugier, C., 1997, April. Parameter identification for dynamic simulation. In Proceedings, 1997 IEEE International Conference on Robotics and Automation, 3(1), pp.1928-1933.
[92] Etzmuss, O., Gross, J. and Strasser, W., 2003. Deriving a particle system from continuum mechanics for the animation of deformable objects. IEEE Transactions on Visualization and Computer Graphics, 9(4), pp.538-550.
[93] Bianchi, G., Solenthaler, B., Székely, G. and Harders, M., 2004, September. Simultaneous topology and stiffness identification for mass-spring models based on fem reference deformations. In International Conference on Medical Image Computing and Computer-Assisted Intervention, pp. 293-301.
[94] Mosegaard, J., 2003. Parameter optimisation for the behaviour of elastic models over time. Studies in health technology and informatics, 98, pp.253-255.
[95] Ishikawa, T., Sera, H., Morishima, S. and Terzopoulos, D., 1998. Facial image reconstruction by estimated muscle parameter. In Proceedings. Third IEEE International Conference on Automatic Face and Gesture Recognition, 1998. pp. 342-347.
[96] Nürnberger, A., Radetzky, A. and Kruse, R., 2001. Using recurrent neuro-fuzzy techniques for the identification and simulation of dynamic systems. Neurocomputing, 36(1), pp.123-147.
[97] Qiao, B., Chen, G. and Ye, X., 2009, August. The research of soft tissue deformation based on mass-spring model. In International Conference on Mechatronics and Automation, ICMA 2009, pp.4655-4660.
[98] Zhu, L., Ye, X., Ji'er, X., Gu, Y. and Guo, S., 2010, June. A real-time deformation modeling scheme of soft tissue for virtual surgical. In IEEE International Conference on Information and Automation, ICIA 2010, pp. 771-775.
[99] Georgii, J. and Westermann, R., 2005. Mass-spring systems on the GPU. Simulation modelling practice and theory, 13(8), pp.693-702.
[100] Rasmusson, A., Mosegaard, J. and Sangild, T., 2008, July. Exploring parallel algorithms for volumetric mass-spring-damper models in CUDA. In International Symposium on Biomedical Simulation, pp. 49-58.
[101] Vassilev, T. and Rousev, R., 2008. Algorithm and data structures for implementing a mass-spring deformable model on GPU. Research and Laboratory University Ruse, pp.102-109.
[102] Leon, C.A.D., Eliuk, S. and Gomez, H.T., 2010, March. Simulating soft tissues using a GPU approach of the mass-spring model. In Virtual Reality Conference (VR), IEEE, pp.261-262.
[103] Etheredge, C.E., 2011. A parallel mass-spring model for soft tissue simulation with haptic rendering in CUDA. In 15th Twente Student Conference on IT.
[104] Wahl, A.M., 1944. Mechanical springs. Penton Publishing Company.
[105] Paredes, M., and Rodriguez, E., 2009. Optimal design of conical springs. Engineering with computers, 25(2), p.147-154.
[106] Sparks, J. L., Vavalle, N. A., Kasting, K. E., Long, B., Tanaka, M. L., Sanger, P. A., Schnell, K., and Conner-Kerr, T. A., 2015. Use of Silicone Materials to Simulate Tissue Biomechanics as Related to Deep Tissue Injury. Advances in Skin & Wound Care, 28(2), pp. 59-68.
[107] Boonvisut, P. and Cavusoglu, M. 2013. Estimation of Soft Tissue Mechanical Parameters from Robotic Manipulation Data. IEEE/ASME Transactions on Mechatronics, 18(5), pp. 1602-1611.
[108] Allard, J., Cotin, S., Faure, F., Bensoussan, P.J., Poyer, F., Duriez, C., Delingette, H. and Grisoni, L., 2007, February. Sofa-an open source framework for medical simulation. In MMVR 15-Medicine Meets Virtual Reality, 125(1), pp. 13-18.
[109] Shi, H., 2007. Finite Element Modeling of Soft Tissue Deformation. Doctor of Philosophy. Department of Electrical and Computer Engineering University of Louisville Louisville, Kentucky.
[110] Saada, A.S., 2009. Elasticity: Theory and Applications, Revised & Updated. J. Ross Publishing.
[111] Boresi, A.P., Chong, K. and Lee, J.D., 2010. Elasticity in engineering mechanics. John Wiley & Sons.
[112] Barden, L., 1963. Stresses and displacements in a cross-anisotropic soil. Geotechnique, 13(3), pp.198-210.
[113] Michell J. H., 1900. The stress distribution in an allotropic solid with an infinite plane boundary. Proc. London Math. Society, 32, pp.247-258.
[114] Olson, R. and Lai, J., 2003. Advanced Soil Mechanics, Unit 8 - Stress Distribution', [Online]. Available: http://www.cyut.edu.tw/~jrlai/CE7332/Chap8.pdf. [Accessed: 09- Oct- 2015].
[115] Lu, G. and Yu, T.X., 2003. Energy absorption of structures and materials. Elsevier.
[116] Helwany, S., 2007. Applied soil mechanics with ABAQUS applications. John Wiley & Sons.
[117] Huangfu, Z., 2013. An Improved Mass-Spring Model for Simulation of Soft Tissue Deformation. Journal of Information and Computational Science, 10(17), pp. 5551–5558.

APPENDICES

APPENDIX 1

The four functions, however, are not completely independent. It can be proved that for an arbitrary three dimensional convex domain, the number of the independent functions can be reduced to three. The functions $\overline{\boldsymbol{A}}$ and B can be deduced from Galerkin's vector $\overline{\boldsymbol{V}}$ if

$$\overline{\boldsymbol{A}} = 2(1-v)\nabla^2\overline{\boldsymbol{V}} \tag{A1.1}$$

$$B = \overline{\nabla}\cdot\overline{\boldsymbol{V}} - \frac{\overline{\boldsymbol{A}}\cdot\overline{\boldsymbol{X}}}{4(1-v)} \tag{A1.2}$$

A special form of $\overline{\boldsymbol{A}}$ and B for problems with axial symmetry is

$$A_r = A_\theta = 0 \tag{A1.3}$$

$$A_z = A_z(r.z) \tag{A1.4}$$

$$B = B(r,z) \tag{A1.5}$$

Looking at the Boussinesq problem in the axisymmetric condition, a load P is acting on the elastic body in a normal direction at the origin of coordinates. According to Saada [110], the four harmonic functions have the solutions in the form of

$$A_r = A_\theta = 0 \tag{A1.6}$$

$$A_z = 4(1-v)\frac{K}{\rho} \tag{A1.7}$$

$$B = C\ln(\rho + l_z) \tag{A1.8}$$

where $\rho = \sqrt{{l_r}^2 + {l_\theta}^2 + {l_z}^2}$.

By adding the harmonic functions into Eq. (4.6), the displacement vector is given as

$$\overline{\boldsymbol{u}} = \frac{4(1-v)}{2G}\frac{K}{\rho}\bar{e}_z - \frac{\overline{\nabla}}{2G}\left[C\ln(\rho + l_z) + \frac{K\,l_z}{\rho}\right] \tag{A1.9}$$

where $\bar{e}_z$is the unit vector in the normal direction. In expanded form, using the cylindrical coordinates, the expression can be written as follows

$$u_r = -\frac{C\ l_r}{2G\rho(\rho + l_z)} + \frac{K\ l_r\ l_z}{2G\rho^3} \tag{A1.10}$$

$$u_\theta = 0 \tag{A1.11}$$

$$u_z = -\frac{(3-4v)K - C}{2G\rho} + \frac{K\ {l_z}^2}{2G\rho^3} \tag{A1.12}$$

The constants can be found by referring to the boundary conditions. The boundary conditions of the problems are

1. On the surface of the semi-infinite solid, $\sigma_{rz} = 0$ everywhere.
2. On the surface of the semi-infinite solid,$\sigma_{zz} = 0$ everywhere.
3. Sum of all vertical stress on a horizontal plane at a depth z is equal to the input load.
4. When r or z approach infinity, all stresses approach zero.

Using the strain-displacement relations in cylindrical coordinate given as [110]

$$e_{rr} = \frac{\partial u_r}{\partial r} \tag{A1.13}$$

$$e_{\theta\theta} = \frac{1}{l_r}\frac{\partial u_\theta}{\partial \theta} + \frac{u_r}{l_r} \tag{A1.14}$$

$$e_{zz} = \frac{\partial u_z}{\partial z} \tag{A1.15}$$

$$e_{r\theta} = \frac{1}{2}\left(\frac{1}{l_r}\frac{\partial u_r}{\partial \theta} + \frac{\partial u_\theta}{\partial r} - \frac{u_\theta}{l_r}\right) \tag{A1.16}$$

$$e_{rz} = \frac{1}{2}\left(\frac{\partial u_r}{\partial z} + \frac{\partial u_z}{\partial r}\right) \tag{A1.17}$$

$$e_{\theta z} = \frac{1}{2}\left(\frac{\partial u_\theta}{\partial z} + \frac{1}{l_r}\frac{\partial u_z}{\partial \theta}\right) \tag{A1.18}$$

and the stress-strain relations given as [110]

$$\sigma_{rr} = \frac{E}{(1+v)(1-2v)}[(1-v)e_{rr} + ve_{\theta\theta} + ve_{zz}] \tag{A1.19}$$

$$\sigma_{\theta\theta} = \frac{E}{(1+v)(1-2v)}[ve_{rr} + (1-v)e_{\theta\theta} + ve_{zz}] \quad \text{(A1.20)}$$

$$\sigma_{zz} = \frac{E}{(1+v)(1-2v)}[ve_{rr} + ve_{\theta\theta} + (1-v)e_{zz}] \quad \text{(A1.21)}$$

$$\sigma_{r\theta} = \frac{E}{(1+v)}e_{r\theta} \quad \text{(A1.22)}$$

$$\sigma_{rz} = \frac{E}{(1+v)}e_{rz} \quad \text{(A1.23)}$$

$$\sigma_{\theta z} = \frac{E}{(1+v)}e_{\theta z} \quad \text{(A1.24)}$$

the following expression is obtained for σ_{rz}

$$\sigma_{rz} = \frac{l_r}{\rho^3}\left[C - K(1-2v) - \frac{3K\,{l_z}^2}{\rho^2}\right] \quad \text{(A1.25)}$$

and the expression for $\sigma_{zz}$is given as

$$\sigma_{zz} = -\frac{3K\,{l_z}^3}{\rho^5}. \quad \text{(A1.26)}$$

The first boundary condition that is $\sigma_{rz} = 0$, when substituted in Eq. (A1.25), it yields the following relation between C and K

$$C = K(1-2v). \quad \text{(A1.27)}$$

To determine the unknown K, in terms of equilibrium force, at any horizontal plane with a distance z from the origin, the resultant of all the vertical forces on this plane must be equal to P. It can be presented in the following integration form

$$P = \int_{r=0}^{r=\infty} \frac{3K\,{l_z}^3}{\rho^5} 2\pi\, l_r\, dr. \quad \text{(A1.28)}$$

Solving the integration gives

$$K = \frac{P}{2\pi}. \quad \text{(A1.29)}$$

Thus, adding Eq. (A1.29) into Eq. (A1.27), we have

$$C = \frac{P}{2\pi}(1-2v). \tag{A1.30}$$

Summing up the results, the solution for the Boussinesq problem in cylindrical coordinate is given as

$$\sigma_{rr} = \frac{P}{2\pi\rho^2}\left[\frac{(1-2v)\rho}{\rho + l_z} - \frac{3\, l_z\, {l_r}^2}{\rho^3}\right] \tag{A1.31}$$

$$\sigma_{\theta\theta} = \frac{(1-2v)P}{2\pi\rho^2}\left[\frac{l_z}{\rho} - \frac{\rho}{\rho + l_z}\right] \tag{A1.32}$$

$$\sigma_{zz} = -\frac{3P{l_z}^3}{2\pi\rho^5} \tag{A1.33}$$

$$\sigma_{rz} = -\frac{3Pl_r{l_z}^2}{2\pi\rho^5} \tag{A1.34}$$

$$u_r = \frac{P}{4\pi G\rho}\left[\frac{l_r l_z}{\rho^2} - \frac{(1-2v\,)l_r}{(\rho+z)}\right] \tag{A1.35}$$

$$u_\theta = 0 \tag{A1.36}$$

$$u_z = \frac{P}{4\pi G\rho}\left[2(1-v\,) + \frac{{l_z}^2}{\rho^2}\right] \tag{A1.37}$$

In Cartesian coordinates, the solution is given as

$$\sigma_{xx} = -\frac{P}{2\pi\rho^2}\left\{\frac{3l_z{l_x}^2}{\rho^3} - (1-2\mu\,)\left[\frac{l_z}{\rho} - \frac{\rho}{\rho + l_z} + \frac{{l_x}^2(2\rho + l_z)}{\rho(\rho + l_z)^2}\right]\right\} \tag{A1.38}$$

$$\sigma_{yy} = -\frac{P}{2\pi\rho^2}\left\{\frac{3l_z{l_y}^2}{\rho^3} - (1-2\mu\,)\left[\frac{l_z}{\rho} - \frac{\rho}{\rho + l_z} + \frac{{l_y}^2(2\rho + l_z)}{\rho(\rho + l_z)^2}\right]\right\} \tag{A1.39}$$

$$\sigma_{zz} = -\frac{3P{l_z}^3}{2\pi\rho^5} \tag{A1.40}$$

$$\sigma_{xy} = -\frac{P}{2\pi\rho^2}\left[\frac{3l_x l_y l_z}{\rho^3} - \frac{(1-2\mu\,)(2\rho + l_z)l_x l_y xy}{\rho(\rho + l_z)^2}\right] \tag{A1.41}$$

$$\sigma_{xz} = -\frac{3Pl_x{l_z}^2}{2\pi\rho^5} \tag{A1.42}$$

$$\sigma_{zy} = -\frac{3Pl_y{l_z}^2}{2\pi\rho^5} \tag{A1.43}$$

$$u_{xx} = \frac{P}{4\pi G}\left[-\frac{(1-2v\,)l_x}{\rho(\rho+l_z)} + \frac{l_x l_z}{\rho^3}\right] \quad \text{(A1.44)}$$

$$u_{yy} = \frac{P}{4\pi G}\left[-\frac{(1-2v\,)l_y}{\rho(\rho+l_z)} + \frac{l_y l_z}{\rho^3}\right] \quad \text{(A1.45)}$$

$$u_{zz} = \frac{P}{4\pi G\rho}\left[2(1-v\,) + \frac{{l_z}^2}{\rho^2}\right] \quad \text{(A1.46)}$$

APPENDIX 2

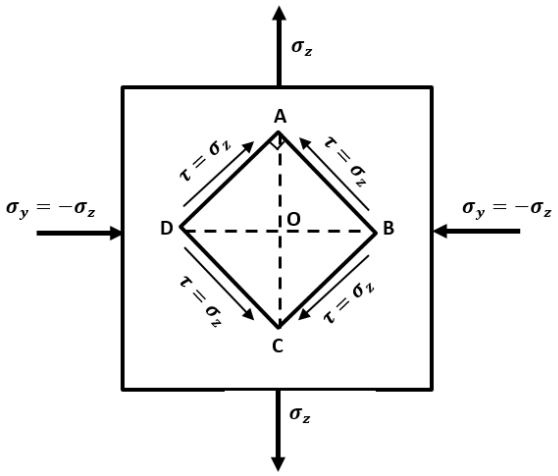

Figure A2.0.1. Plane stress element.

Consider the state of plane stress $\sigma_x = 0$ as shown in Fig. A2.1. The shear stress τ is equal to the direct stress σ_z and will strain the element $ABCD$ so that the right angle DAB alters by an amount γ. In the triangle OAB, after deformation,

$$\frac{OB}{OA} = \frac{1+\varepsilon_y}{1+\varepsilon_z} = \tan\left(\frac{\pi}{2} - \frac{\gamma}{2}\right) \tag{A2.1}$$

For a very small value of ε_y, ε_z and γ, the relation between them is given as

$$\varepsilon_y - \varepsilon_z = -\gamma \tag{A2.2}$$

From Eq. (5.6) and Eq. (5.7), and putting $\sigma_x = 0$ and $\sigma_y = -\sigma_z$, we have

$$\varepsilon_y = -\frac{\sigma_z}{E}\left(\frac{1}{n} + v_3\right) \tag{A2.3}$$

$$\varepsilon_z = \frac{\sigma_z}{E}\left(1 + \frac{v_2}{n}\right) \tag{A2.4}$$

Thus

$$\gamma = \varepsilon_z - \varepsilon_y = \frac{\sigma_z}{E}\left(1 + \frac{v_2}{n} + \frac{1}{n} + v_3\right) \tag{A2.5}$$

Substituting $\sigma_z = \tau$ and $n = \frac{v_2}{v_3}$, gives

$$\tau = \frac{Ev_2}{(v_2 + v_3 + 2v_2v_3)} \cdot \gamma \quad \text{(A2.6)}$$

From Hooke's law, shear stress in term of shear strain is given as

$$\tau_{zx} = G_1\gamma_{zx} \quad \text{(A2.7)}$$

$$\tau_{zy} = G_2\gamma_{zy} \quad \text{(A2.8)}$$

$$\tau_{xy} = G_3\gamma_{xy} \quad \text{(A2.9)}$$

Then, comparison of Eq. (A2.7) and Eq. (A2.8) with Eq. (A2.6), the stiffness constant is given as

$$C_{44} = \frac{Ev_2}{(v_2 + v_3 + 2v_2v_3)} \quad \text{(A2.10)}$$

APPENDIX 3

The Hooke's law equation for the cross-anisotropic material is given in the form of

$$\begin{bmatrix}\sigma_1\\ \sigma_2\\ \sigma_3\\ \sigma_4\\ \sigma_5\\ \sigma_6\end{bmatrix} = \begin{bmatrix} C_{11} & C_{12} & C_{13} & 0 & 0 & 0 \\ & C_{11} & C_{13} & 0 & 0 & 0 \\ & & C_{33} & 0 & 0 & 0 \\ & & & C_{44} & 0 & 0 \\ & & & & C_{44} & 0 \\ & & & & & C_{11}-C_{12} \end{bmatrix} \begin{bmatrix}\varepsilon_1\\ \varepsilon_2\\ \varepsilon_3\\ \varepsilon_4\\ \varepsilon_5\\ \varepsilon_6\end{bmatrix} \tag{A3.1}$$

Then, by using the symmetrical relations, the Hooke's law equation can be inverted in terms of elastic constants E, *v* and G as

$$\begin{bmatrix}\varepsilon_1\\ \varepsilon_2\\ \varepsilon_3\\ \varepsilon_4\\ \varepsilon_5\\ \varepsilon_6\end{bmatrix} = \begin{bmatrix} \frac{1}{E_1} & \frac{-v_{12}}{E_1} & \frac{-v_{31}}{E_3} & 0 & 0 & 0 \\ \frac{-v_{12}}{E_1} & \frac{1}{E_1} & \frac{-v_{31}}{E_3} & 0 & 0 & 0 \\ \frac{-v_{13}}{E_1} & \frac{-v_{13}}{E_1} & \frac{1}{E_3} & 0 & 0 & 0 \\ 0 & 0 & 0 & \frac{1}{2G_{13}} & 0 & 0 \\ 0 & 0 & 0 & 0 & \frac{1}{2G_{13}} & 0 \\ 0 & 0 & 0 & 0 & 0 & \frac{1}{2G_{12}} \end{bmatrix} \begin{bmatrix}\sigma_1\\ \sigma_2\\ \sigma_3\\ \sigma_4\\ \sigma_5\\ \sigma_6\end{bmatrix} \tag{A3.2}$$

where the symmetrical property give the following relations

$$\begin{aligned} E_1 &= E_2 \\ v_{12} &= v_{21} \\ v_{13} &= v_{23} \\ v_{31} &= v_{32} \\ G_{13} &= G_{23} \end{aligned} \tag{A3.3}$$

$$\frac{v_{13}}{E_1} = \frac{v_{31}}{E_3} \tag{A3.4}$$

The relation of the shear modulus to the elastic modulus and the Poisson ratio in the respective orientation is given as

$$G_{ij} = \frac{E_{ij}}{2(1 + v_{ij})} \quad \text{(A3.5)}$$